



ÉCOLE POLYTECHNIQUE
FÉDÉRALE DE LAUSANNE

EDMX

PHD THESIS

**Construction and Operation of a
milli-Kelvin Spectroscopic Imaging STM
for the study of correlated electron
materials**

Author:

Mostafa ENAYAT

Supervisors:

Prof. Klaus KERN

Prof. Peter WAHL

Tunneling Spectroscopy of Strongly Correlated Electron Materials

MPI- FKF

May 2014

Abstract

Understanding the mechanism of unconventional superconductivity in correlated electron materials is a step towards developing superconductors with higher transition temperatures. Scanning tunneling microscopy/spectroscopy is a perfect tool to study the quantum mechanical states of correlated electron materials both in real space and momentum space.

In this thesis I discuss about construction, development and operation of an spectroscopic imaging scanning tunneling microscopy (SI-STM) which operates at milli-Kelvin temperatures, and magnetic fields up to 14 Tesla. Measuring at ultra low temperatures has the advantage of approaching exciting electronic phases (e.g. superconductivity), and additionally enhances the spectroscopic energy resolution to microelectron volt range, which is crucial for the study of strongly correlated electron materials. SI-STM can be used to image the electronic excitations and structure close to the Fermi energy, and to detect the quasi-particle interference (QPI) in Fourier space.

This thesis deals mainly with different families of correlated electron materials, in particular about their superconducting and magnetic phases. The studied superconductors belong to the family of heavy fermion compounds (CeCu_2Si_2), and noncentrosymmetric superconductors (BiPd); whereas the magnetic compounds are linked with parent compounds of iron-based superconductors (Fe_{1+y}Te), and heavy fermions (CeB_6).

I show the possibility to image the atomic-scale magnetic structure of a parent compound of an iron-based superconductor in real space, which has been carried out for the first time. This brings the possibility to carry out spin-polarized measurements on high temperature superconductors (cuprates). Furthermore, the vortex lattice of the heavy fermion superconductor CeCu_2Si_2 has been visualized by STM. This has not been accomplished by other techniques such as neutron scattering previously, and highlights the suitability of STM for research in condensed matter physics. Eventually the first tunneling measurements with atomic resolution on a family of non-centrosymmetric superconductor has been carried out. The results on BiPd indicate a BCS gap, and mark this compound as a conventional type two superconductor.

The results can help to further understand the relation and interplay between magnetism and superconductivity, and also the mechanism of superconductivity in these materials.

Keywords: Scanning tunneling microscopy, dilution refrigeration, correlated electron materials, Iron based superconductors, Heavy fermions

Kurzfassung

Ein wichtiger Schritt für die Entwicklung von Supraleitern mit höheren sprungtemperaturen ist das Verständnis des Mechanismus der unkonventionellen Supraleitung in korrelierten Elektronenmaterialien. Rastertunnelmikroskopie /-Spektroskopie eignet sich dabei sehr gut, um die elektronischen Zustände korrelierter Elektronenmaterialien sowohl im Realraum also auch im Impulsraum zu studieren.

In dieser Arbeit diskutiere ich die Konstruktion, Entwicklung und Inbetriebnahme eines spektroskopischen Rastertunnelmikroskops (SI-STM), das bei Temperaturen von einigen MilliKelvin und bei Magnetfeldern bis zu 14 Tesla arbeitet. Messungen bei extrem niedrigen Temperaturen bieten die Möglichkeit der Annäherung spannende elektronische Phasen (z.B. Supraleitung) und verbessert zusätzlich die spektroskopische Energieauflösung, welche entscheidend ist für stark korrelierte Materialien. SI-STM wird dabei zur Abbildung der elektronischen Anregungen und Struktur in der Nähe der Fermi-Energie verwendet, ebenso wie zur Erfassung von Quasi-Partikel-Interferenz (QPI) im Fourierraum.

Der Großteil der Arbeit enthält Messungen an verschiedenen Familien von korrelierten Elektronenmaterialien, mit hauptsächlich supraleitenden und magnetischen Phasen. Die untersuchten Supraleiter gehören zur Familie der Schweren-Fermionen-Verbindungen (CeCu_2Si_2) und nichtzentrosymmetrischen Supraleitern (BiPd), während die magnetischen Phasen Verbindungen mit übergeordneten Verbindungen von Eisen-basierten Supraleitern (Fe_{1+y}Te) und schwere Fermionen (CeB_6) sind.

Ich zeige die Möglichkeit, die atomaren magnetischen Struktur der nicht supraleitender Basisverbindung eines Eisen-basierten Supraleiter im realen Raum abzubilden, was zum ersten Mal durchgeführt werden konnte. Dies eröffnet die Möglichkeit zur Durchführung von spin-polarisierten Messungen an Hochtemperatur-Supraleitern (Cupraten). Außerdem wurden die Vortex-Gitter der Schweren-Fermionen-Supraleiter CeCu_2Si_2 durch STM-Messungen abgebildet. Dies ist bis jetzt nicht durch Techniken wie Neutronenstreuung erreicht worden, und hebt die Bedeutung von STM in der Physik kondensierter Materie hervor. Schließlich wurde die erste Tunnel Messungen mit atomarer Auflösung zu einer Familie von nicht-zentrosymmetrischen Supraleiter durchgeführt.

Die Ergebnisse können dazu beitragen, die Beziehung und das Zusammenspiel zwischen Magnetismus und Supraleitung, und auch den Mechanismus der Supraleitung in diesen Materialien weiter zu verstehen.

Stichworte: Rastertunnelmikroskopie, Mischungskühlung, korrelierte Elektronen Materialien, Eisen basierten Supraleitern, Schwere-Fermionen

Contents

Abstract	i
Kurzfassung	ii
1 Introduction	1
1.1 Correlated electron materials	1
1.2 Objective	3
1.3 Outline	4
2 Introduction to Scanning Tunneling Microscope	5
2.1 Working principle of STM	5
2.2 Tunneling Theory	6
2.3 Imaging the topography	8
2.4 Density of states	9
2.4.1 DOS of superconductors	10
2.4.1.1 BCS gap	10
2.4.1.2 Dynes gap	12
2.5 Spectroscopic maps	12
2.5.1 Quasi particle interference (QPI)	13
3 Setup and construction of a milli-Kelvin STM	14
3.1 Dilution refrigeration	14
3.1.1 Operation mechanism and components of a dilution refrigerator . .	16
3.2 Setup and challenges	17
3.3 First results	20
3.3.1 Measurements on NbSe ₂ single crystal	20
3.3.2 Measurements of Aluminum tip on gold sample	21
4 Al-Al Josephson junction	24
4.1 Introduction on Josephson coupling	24
4.2 Data on Al-Al junction	26
4.3 Characterizing the STM circuit	28
4.3.1 The RCSJ Model	29
4.3.1.1 Phase diffusive model	31
4.3.2 Quantum fluctuations model (Ingold model)	34
4.4 Conclusion and summary	36

5	Visualizing the magnetic structure in Fe_{1+y}Te	38
5.1	Iron-chalcogenides	38
5.2	Results	40
5.2.1	Unidirectional modulation from topography of $\text{Fe}_{1.07}\text{Te}$	41
5.2.2	Twin boundaries	43
5.2.3	Bias dependence	43
5.2.4	Temperature dependence	45
5.2.5	Spatial dependence on spectra	45
5.2.6	Topography of $\text{Fe}_{1.15}\text{Te}$	47
5.2.7	Quasi particle interference (QPI)	48
5.2.8	Spectroscopy on excess Fe defects	48
5.2.9	Magnetic field dependence	49
5.2.10	Conclusion and summary	51
6	Observation of vortices on CeCu_2Si_2	54
6.1	Introduction to Heavy-Fermion compounds	54
6.1.1	Introduction to CeCu_2Si_2	56
6.1.1.1	Sample preparation and heat-capacity measurements	57
6.2	Results	58
6.2.1	Topography and periodic rows	58
6.2.2	Spectroscopy in large energy range and superconducting gap as a function of temperature	59
6.2.3	Field dependence spectra	61
6.2.3.1	Observation of vortices as a function of field	62
6.2.3.2	Average distance between vortices as function of field	62
6.2.3.3	Extraction of coherence length from data and from autocorrelation of data	63
6.3	Conclusion and summary	66
7	Tunneling measurements on magnetic phases of CeB_6	67
7.1	Introduction	67
7.2	STM measurements	68
7.2.1	Topography	68
7.2.2	Temperature dependence of spectra	68
7.2.3	Field dependence spectra	71
7.3	Summary and conclusion	72
8	Superconducting gap and vortex core on BiPd	73
8.1	Introduction	73
8.2	Results	75
8.2.1	Physical characterization of the crystal	75
8.2.2	STM measurements	76
8.2.2.1	Topography	76
8.2.2.2	Tunneling spectra	77
8.2.2.3	Temperature dependence	78
8.2.2.4	Magnetic field dependence	79
8.2.2.5	Vortex core	81
8.2.2.6	Measurements with superconducting tips	82

8.3 Summary and Discussion	84
9 Conclusion and summary	85
Bibliography	88
Acknowledgements	102
Publications	103
Curriculum Vitae	104

Chapter 1

Introduction

Strongly correlated materials are a broad family of electronic materials which were discovered in the last few decades, exhibiting extraordinary (usually technologically practical) electronic and magnetic properties. Many of these materials are composed of transition metal oxides, which may be classified according to their properties, e.g. high temperature superconductors, spintronic materials, quasi-low-dimensional materials, etc. Due to the similarities of the phase diagrams of these compounds, understanding the mechanism of superconductivity for correlated electron materials might be very helpful to design superconductors with a higher transition temperature, and maybe even one day obtaining a material which has a transition temperature above room temperature.

1.1 Correlated electron materials

Electrons in metals are known to be itinerant and delocalized, where they move independently in extended Bloch states. In metals electrons are well defined in momentum-space (k-space). On the other hand, for insulators electrons are known to be localized and can not move. Electrons in this case are defined in real-space. By introducing magnetic ions to metals (e.g. rare earth compounds) or by doping insulators (e.g. doped Mott insulators like copper-oxide superconductors) a system known as correlated electron material is formed which shows new properties.

Correlated electron materials have incompletely filled d- or f-electron shells with narrow energy bands, which require a high energy resolution to detect the electronic excitations. The duality between localized and delocalized character of electrons makes the difference to conventional materials complicated, including their theoretical description and experimental detection. For studying electronic behavior of these compounds, it

is essential to obtain data from both real space and k-space. STM is an ideal tool to retrieve information on the electronic excitations in both spaces. STM offers the possibility to detect the local density of states (LDOS) with atomic resolution in real space. By transforming spectroscopic maps to Fourier space, it is possible to gain information about the dispersion of quasiparticles in momentum-space, by analyzing the interference pattern of electrons and holes (quasiparticles).

Unconventional superconductors, or compounds with complex magnetic phase diagrams are examples of correlated electron materials, which are suitable to be studied with STM. These materials are divided in many families of compounds: Cuprates, iron-based superconductors, heavy fermions, Manganites, Ruthenates, etc.

Cuprates, which are copper-oxide superconductors, were discovered in 1986 by IBM researchers Müller and Bednorz [1], who were awarded the 1987 Nobel prize in physics “for their important break-through in the discovery of superconductivity in ceramic materials”. These compounds have the highest transition temperature of the known superconductors, up to 150K at high pressures, making them extremely interesting for applications. BSCCO ($\text{Bi}_2\text{Sr}_2\text{CaCu}_2\text{O}_{8+\delta}$) has been extensively studied with STM and angle resolved photoemission spectroscopy (ARPES) because it cleaves easily, exposing an atomically flat surface. For Cuprates, superconductivity originates from the strongly interacting electrons in the Cu-O planes. The undoped compound has an antiferromagnetic Mott insulating ground state in which Coulomb repulsion prevents electrons from hopping from Cu to Cu. Doping these insulating CuO_2 layers with holes (removing electrons) causes the appearance of new electronic states including high temperature superconductivity and the still poorly understood pseudogap phase.

Iron-based superconductors were discovered in 2006 by Japanese researchers [2]. Soon these materials gained focus by the scientific community since these materials were the first to show high T_c superconductivity in a non copper based material. The superconducting transition temperatures in iron-based superconducting materials are lower than those of cuprates [3]. In iron-based superconductors, unlike the cuprates, it appears that multiple 3d orbitals of the iron are involved in the electronic structure near the Fermi energy [4]. Although the undoped material is also antiferromagnetic, unlike in the cuprates, it is metallic. With doping, the magnetic state is suppressed and a superconducting phase appears.

Heavy Fermion compounds were first discovered in 1975 by researchers in Bell Laboratories [5]. These materials are typically intermetallic compounds containing actinides or rare earth ions (such as Ce, U, Yb). Heavy fermions have a high electronic specific heat coefficient ($\gamma > 400 \text{ mJ/mol.K}^2$), implying that the effective mass of the electrons are high ($\gamma \propto m^*$). The first heavy fermion superconductor was discovered in 1979 by

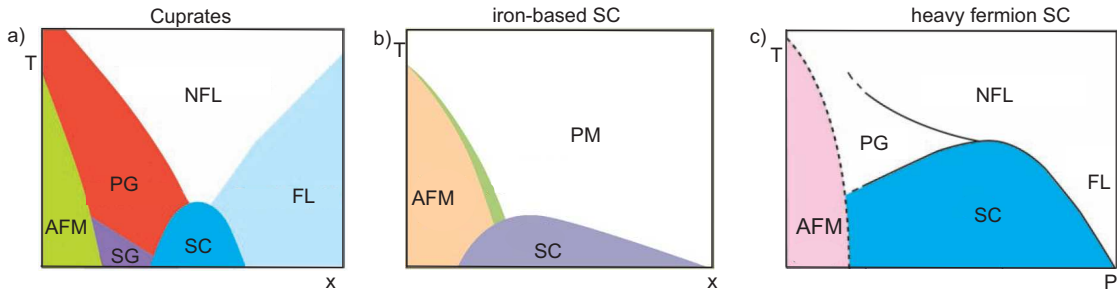


FIGURE 1.1: Generic phase diagrams of (a) HTSC-cuprates as a function of doping (x), reproduced from [7] (b) Iron-based superconductors as a function of doping (x), reproduced from [8] (c) Heavy fermion compound as a function of pressure (p), reproduced from [7]. AFM, antiferromagnetic; SC, superconducting; PM, paramagnetic phase; (N)FL, (non) Fermi liquid; PG, pseudogap; SG, spin glass phase.

F. Steglich [6] (chapter 6). This was unexpected due to the assumption that magnetic ions suppress superconductivity. As it can be seen in Fig. 1.1, the phase diagrams of cuprates, iron-based superconductors and heavy fermions show some similarities.

The properties of heavy fermion materials exhibit drastic changes under comparatively small variations in temperature, magnetic field, composition or pressure [9], indicating a rich electronic structure in the vicinity of the Fermi level (E_F). This is reflected in the heavy effective mass of the conduction electrons but also in the delicate balance between localized and delocalized electronic states often found in these compounds. The relevant temperature scales for heavy fermion materials are frequently well below 1K, therefore the experimental investigation of the changes in the electronic structure as a function of temperature and magnetic field requires very low temperatures [10, 11].

Because of the similarities of the phase diagram (Fig. 1.1), and the similar interaction of the localized spins with the conduction electrons (heavy fermions and iron-based superconductors), there might be a relation for the mechanism of superconductivity.

1.2 Objective

In recent years, spectroscopic-imaging STM has proven to be able to give insight into details of the band structure, electronic excitations near the Fermi level, and information on local inhomogeneities and the influence of defects from spatial maps of the differential conductance (dI/dV), which for energies close to the Fermi energy is proportional to the local density of states (LDOS) [12]. Transforming the data into reciprocal space yields information on the dominant scattering vectors due to quasiparticle interference, revealing information about the electronic structure [13]. It has been shown that in superconducting materials, from analyzing quasiparticle interference, even the symmetry of the superconducting order parameter can be determined [14]. Similar studies of the

superconducting order parameter in heavy fermion materials and also organic [15] or topological [16] superconductors are highly attractive, however they require operation of the STM at temperatures well below 1K. The resolution of tunneling spectroscopy is limited by the thermal broadening of the Fermi distribution of the charge carriers in the tip and is improved by going to lower temperatures.

1.3 Outline

In chapter 2 I will briefly discuss and explain the basis of how an STM works and what information we can retrieve from the data. In chapter 3 the working principle of a dilution refrigerator will be explained, and then I discuss the setup and construction of our home-built spectroscopic-imaging STM (SI-STM) which operates at milli-kelvin temperatures [17]. This enables us to probe the electronic excitations of correlated electron materials with excellent energy resolution. In order to test and characterize the energy resolution, electronic temperature and stability of the STM scan head we performed measurements on NbSe₂ and Aluminium. In chapter 4 I discuss Al-Al Josephson junctions, from which I derive the values of the elements of the STM circuit. Various methods have been used to model the supercurrent flow between the coupled superconductors (Cooper pair tunneling). In chapter 5 I show results on the parent compound of the '11' family of iron chalcogenides, Fe_{1+y}Te, which has a spin density wave (SDW) phase. An interesting and enigmatic unidirectional modulation has been observed for this material. In chapter 6, measurements on the first discovered heavy fermion superconductor, CeCu₂Si₂, are shown. For the first time, the vortex lattice of this material has been imaged. In chapter 7, I show results on another heavy fermion compound with a complex magnetic phase diagram at low temperatures, CeB₆. Measurements as a function of temperature and magnetic field showed a change in the conductance spectra, possibly due to the variation of the magnetic phase. In chapter 8, I show the superconducting gap as a function of temperature and magnetic field, vortex with atomic resolution on the non-centrosymmetric superconductor BiPd. Results indicate an s-wave superconducting gap order parameter. Finally, in chapter 9, I draw a summary and conclusion of the thesis.

Chapter 2

Introduction to Scanning Tunneling Microscope

Since the invention of scanning tunneling microscope (STM) about three decades ago, this technique has been widely used, applied and adapted in different fields of science and research. It is a nano-scope made up of a sharp tip, which provides a unique opportunity to investigate the topography and electronic excitations of conductive samples on atomic level. This technique can be used either in studying the surface or physics of the bulk of specimen. Spectroscopic Imaging- STM (SI-STM) enables us to spatially image the electronic excitations and offers insight to the momentum (reciprocal) space of electrons, hinting about the electronic band structure of the crystal. In this chapter I will briefly discuss how an STM works and how we can interpret the data obtained from an STM. This chapter is based on these references [18–22].

2.1 Working principle of STM

An STM is an instrument which exploits the strong distance dependence of quantum tunneling of electrons in order to probe the surface of a conducting or semi-conducting material. The components of an STM are shown schematically in Fig. 2.1. As it can be seen, a bias is applied to the junction across the tip and surface in order to tunnel the electrons between the tip and the sample. Consequently, the tip scans over the sample and by applying a feedback loop the topography can be recorded. The STM tip is mounted on a piezoelectric scan tube, which by applying a voltage it can scan in the subnanometer range.

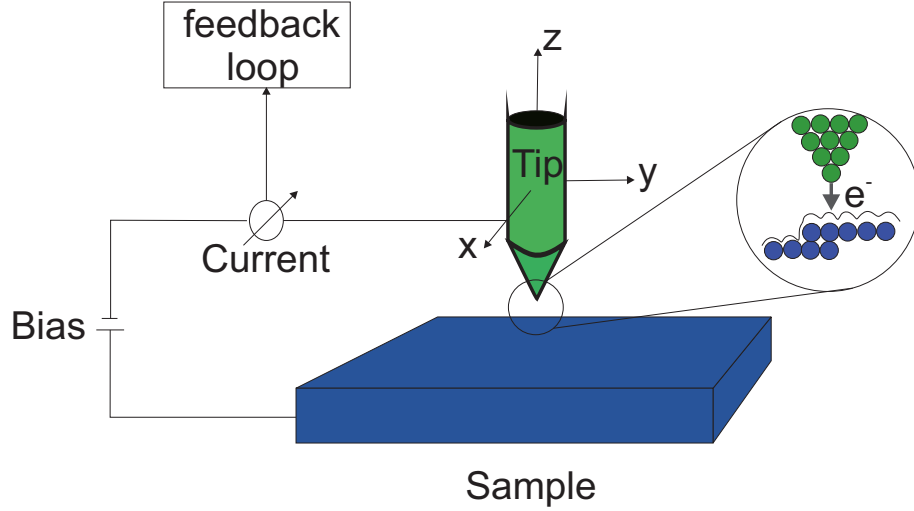


FIGURE 2.1: Schematic illustration of an STM. A bias is applied across the junction between tip and sample which tunnel the electrons. The feedback loop sustains the tunneling current at a desired value. After fixing the sample bias voltage to V_{set} , a feedback loop controls the voltage on the z piezo to keep the tunneling current constant at I_{set} .

2.2 Tunneling Theory

One of the fundamental features of quantum mechanics which distinguishes it from classical mechanics, is the tunneling phenomenon. In classical mechanics particles can not pass through a wall, whereas in quantum mechanics, particles (e.g. electrons) from separate electrodes can tunnel through a thin insulating barrier (e.g. vacuum). If a positive bias V is applied to the sample with respect to the tip, the Fermi level of the sample reduces amount of eV respectively. The electrons will tend to flow from the occupied state of the tip to the empty states of the sample. This situation is illustrated in Fig. 2.2. From Schrödinger's equation it is possible to determine the tunneling current ratio on the two side of the insulating barrier,

$$I(d) = I(0) \exp(-2\kappa d), \quad (2.1)$$

$$\kappa = \frac{\sqrt{m (\Phi_t + \Phi_s - eV)}}{\hbar}. \quad (2.2)$$

κ is the decay constant of the barrier region, being dependent on the electron mass m , Planck constant \hbar , and the work functions of the tip and sample Φ_t , Φ_s . The work functions are on the order of 5 eV , which makes κ on the order of 10 nm^{-1} . This indicates that by increasing the barrier (tip-sample distance) width d only 1 \AA , the tunneling current will reduce 1 order of magnitude, making STM a very powerful tool to detect

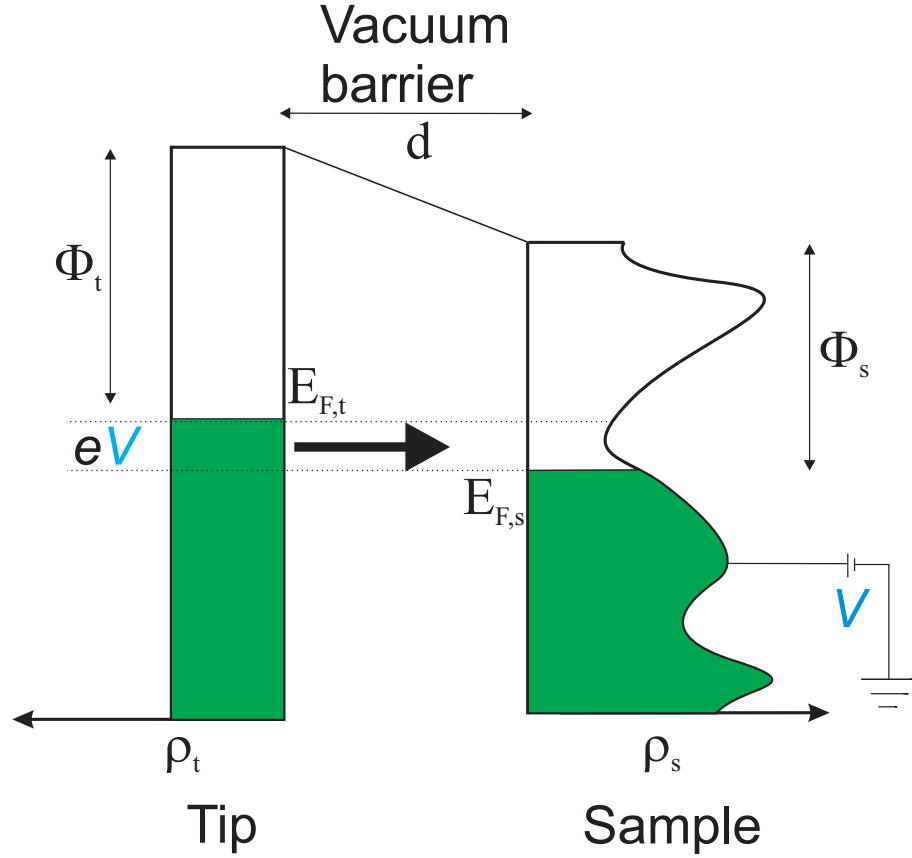


FIGURE 2.2: schematic of a tunnel junction with a positive bias voltage V applied to the sample. Φ_t and Φ_s are the work functions of the tip and sample respectively. The vertical axis shows the energy and the horizontal axes show the density of states for the tip and sample. Filled states are shown in green.

atomic corrugations in the range of tens of picometers. Bardeen formulated the theory of a current through a planar tunneling junction using time dependent perturbation theory and Fermi's golden rule [23], which can also be used for describing tunneling in STM with slight modifications proposed by Tersoff and Hamann [24]. By assuming energy conservation during tunneling process (elastic tunneling), then the net tunneling current can be written as:

$$\begin{aligned} I &= I_{t \rightarrow s} - I_{s \rightarrow t} \\ &= \frac{4\pi e}{\hbar} \int_{-\infty}^{\infty} |M|^2 \rho_s(E_s) \rho_t(E_t) \{f(E_t, T)[1 - f(E_s, T)] - f(E_s, T)[1 - f(E_t, T)]\} d\varepsilon. \end{aligned} \quad (2.3)$$

where e is the electron charge, $|M|$ is the matrix element for tunneling and $\rho_s(E)$ and $\rho_t(E)$ are the density of states of the sample and the tip respectively, and $f(E, T)$ is the Fermi distribution:

$$f(E, T) = \frac{1}{1 + \exp(E/k_B T)} \quad , \quad (2.4)$$

The tip and the sample energies can be written as ($E_t = \varepsilon + eV$ and $E_s = \varepsilon$), since the bias voltage V , alters the relative elastic tunneling. Therefore the tunneling current can

be written as:

$$I = \frac{4\pi e}{\hbar} \int_{-\infty}^{\infty} |M|^2 \rho_s(\varepsilon) \rho_t(\varepsilon + eV) [f(\varepsilon, T) - f(\varepsilon + eV, T)] d\varepsilon, \quad (2.5)$$

This current is referred as the integrated density of states (IDOS). In practice, the tip is usually selected from a material which has a flat density of states (no energy dependence), so that $\rho_t(\varepsilon + eV)$ can be treated as a constant and be taken outside the integral. The most common tips are W, Pt, and Pt-Ir, which all are metals with flat DOS near the fermi level. Another approximation is to treat the matrix element $|M|$ energy independent, such that it can be taken outside of integral. The tunneling current can be simplified to the equation:

$$I = \frac{4\pi e}{\hbar} |M|^2 \rho_t(0) \int_{-\infty}^{\infty} \rho_s(\varepsilon) [f(\varepsilon, T) - f(\varepsilon + eV, T)] d\varepsilon, \quad (2.6)$$

When $T \rightarrow 0$, $\{f(\varepsilon, T) - f(\varepsilon + eV, T)\}$ is a step function and equals 1 in the range of $0 < \varepsilon < eV$, and can be neglected from Eq. 2.6. This assumption is realistic for an STM operating at milliKelvin temperature.

Finally, the matrix element $|M|^2$ can be approximated using Eq. 2.1, 2.2, showing the exponential decay of the current by increasing the tip-sample distance,

$$|M|^2 = \exp(-10.2 d \sqrt{\varphi}), \quad (2.7)$$

where φ is the average work function of the tip and the sample (with unit of eV) and d is the tip sample distance (with unit \AA). Consequently the tunneling current can be expressed in the form:

$$I = \frac{4\pi e}{\hbar} \exp(-10.2 d \sqrt{\varphi}) \rho_t(0) \int_0^{eV} \rho_s(\varepsilon) d\varepsilon. \quad (2.8)$$

2.3 Imaging the topography

One of the biggest advantages of using an STM is that it enables us to image atoms and local defects, such as vacancies, adatoms or step edges with high resolution depending on the sharpness of the tip. The most common way to image the topography is by using a constant (tunneling) current mode. In this mode, after fixing the sample bias voltage to V_{set} , a feedback loop controls the voltage on the z piezo to keep the tunneling current constant at I_{set} . By recording the voltage of the z piezo, it is possible to map the height of the surface [20]. However, it should be noted that the height of the surface depends

on the IDOS of the sample, meaning that at some voltage biases the topography might look different due to the electronic configuration of the surface.

2.4 Density of states

A feature which makes STM unique and an exciting probe for physicists is its ability to locally detect the electronic density of states (DOS) as a function of energy. This feature can be extracted from the tunneling current seen in Eq. 2.8, where the IDOS can be converted to DOS by deriving the differential conductance spectra with the assumptions of a constant tip-sample separation and constant tip DOS in the energy range of interest.

$$\begin{aligned} I &= I_0 \int_0^{eV} \rho_s(\epsilon) d\epsilon, \\ G(V) &= \frac{dI}{dV} \propto \rho_s(eV) \end{aligned} \quad (2.9)$$

accounting for thermal broadening due to the Fermi distribution, the tunneling conductance can be expressed as:

$$\frac{dI}{dV}(V) \propto \int_{-\infty}^{\infty} \rho_s(E) \times \left[\frac{-\partial f(E + eV, T)}{\partial V} \right] dE. \quad (2.10)$$

In practice, the differential tunneling conductance is measured by setting the tip-sample distance, specified by the junction resistance at bias and current setpoints (V_t and I_t). By sweeping the bias, there will be a tunneling current which can be detected, therefore the $I - V$ curve can be plotted. A common technique to measure the differential conductance spectra is to use a lock-in amplifier. In this technique, a small sinusoidal voltage modulation V_{mod} is added to the bias voltage. The resulting current modulation, which is read by the lock-in amplifier connected to the output of the current amplifier, is proportional to the differential conductance. By applying the Taylor expansion, the current can be written as:

$$I(V + V_{mod} \sin \omega t) = I(V) + \frac{dI}{dV} \Big|_V \cdot V_{mod} \sin \omega t, \quad (2.11)$$

where ω is the frequency of the modulation voltage. Therefore, at any given point on the surface, the LDOS can be measured as a function of the bias, by recording the amplitude of the lock-in output, which is proportional to dI/dV (differential conductance). The broadening due to the lock-in modulation V_{RMS} is accounted for from the convolution

of Eq. 2.10 with a half-circle [25],

$$G_{fit}(V) \propto \int_{-\sqrt{2}V_{ac}}^{\sqrt{2}V_{ac}} \frac{dI}{dV}(V + E) \sqrt{2V_{ac}^2 - E^2} dE. \quad (2.12)$$

The energy resolution in the spectra, is the minimum separation in energy of two neighboring spectroscopic features which can be resolved. The total energy resolution is made up of a thermal ($\Delta E_{thermal}$) and lock-in ($\Delta E_{Lock-in}$) contributions, shown below [26]:

$$\begin{aligned} \Delta E &= \sqrt{(\Delta E_{thermal})^2 + (\Delta E_{Lock-in})^2}, \\ &\simeq \sqrt{(3.5k_B T)^2 + (2.5eV_{mod})^2} \end{aligned} \quad (2.13)$$

Equation 2.13 shows that by reducing the temperature T and amplitude of the voltage modulation V_{mod} , the energy resolution will improve. However, reduction of V_{mod} beyond a certain threshold results in less signal to noise ratio. Therefore an optimum V_{mod} has to be selected for the measurements.

2.4.1 DOS of superconductors

2.4.1.1 BCS gap

In order to visualize the tunneling process, a simple energy (E)- momentum (k) diagram can be represented as shown in Fig. 2.3. In Fig. 2.3a, the dashed line represents the portion of the parabola below the fermi energy E_F (hole states) which has been reflected across the Fermi level. For the case of the superconductor, all the Cooper pairs are at the Fermi level and a minimum threshold energy Δ (energy gap) is required by an excitation as shown in Fig. 2.3b. In this case, a particle which is partly in the electron state and partly in the hole state exists, which are known as quasiparticles which have energy $E = (\varepsilon^2 + \Delta^2)^{1/2}$ [22]. From this relation between E and ε , and also $N(E)dE = \rho(\varepsilon)d\varepsilon$ where $N(E)$ and $\rho(\varepsilon)$ are the density of states in the superconductor and in the normal metal respectively. Thus we have

$$N(E) = N(0) \left[\frac{E}{\sqrt{E^2 - \Delta^2(E)}} - \frac{\Delta(E)[d\Delta(E)/dE]}{\sqrt{E^2 - \Delta^2(E)}} \right]. \quad (2.14)$$

In the case of BCS approximation (where $d\Delta(E)/dE = 0$), we have the following equation for the density of states:

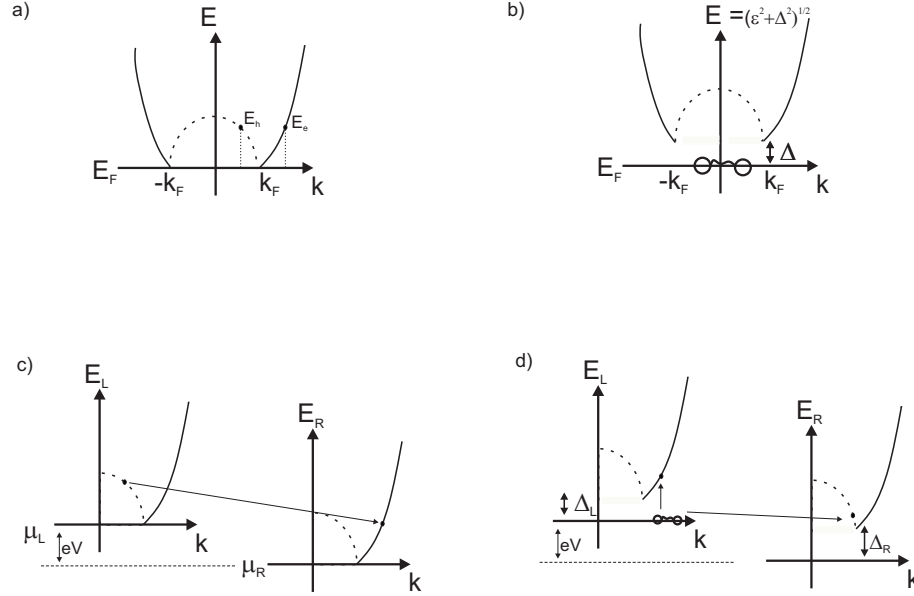


FIGURE 2.3: Energy momentum diagrams of a) Normal metal. b) Superconducting metal. c) electron tunneling process between two normal metal electrodes. d) quasi-particle tunneling process between superconductors. The process involves the breaking of a Cooper pair. Reproduced from [22]

$$N(E) \propto \begin{cases} \frac{|E|}{\sqrt{E^2 - \Delta^2}} & |E| \geq \Delta \\ 0 & |E| \leq \Delta \end{cases} \quad (2.15)$$

The tunneling process between normal metals is shown in Fig. 2.3c. The transfer of an electron from the left to the right metal creates a hole excitation on the left and an electron state on the right. When the two metals are in the superconducting state the tunneling current can be written as:

$$I_{SS} = \text{constant} \times \int_{-\infty}^{+\infty} \frac{|\varepsilon|}{|\varepsilon^2 - \Delta_L^2|^{1/2}} \frac{|\varepsilon + eV|}{|(\varepsilon + eV)^2 - \Delta_R^2|^{1/2}} [f(\varepsilon, T) - f(\varepsilon + eV, T)] d\varepsilon, \quad (2.16)$$

By solving this integral with numerical calculations, we will obtain for the current I_{SS} a finite discontinuity at $V = \pm|\Delta_R + \Delta_L|/e$ and a logarithmic singularity at a voltage $V = \pm|\Delta_R - \Delta_L|/e$ for $T \neq 0$. The single electron tunneling between two superconductors is combined with the destruction of a pair on the left and creation of an excitation on the right as seen in Fig. 2.3d.

2.4.1.2 Dynes gap

Quasiparticles at the Fermi energy will have a limited coherence length (e.g. due to scattering at impurities), which will introduce a lifetime broadening Γ . The following equation has been proposed by Dynes [27]:

$$\frac{dI}{dV}(V) \propto \left| \operatorname{Re} \left[\frac{eV - i\Gamma}{\sqrt{(eV - i\Gamma)^2 - \Delta^2}} \right] \right|, \quad (2.17)$$

where V is the bias voltage and $\frac{dI}{dV}(V)$ the differential conductance (neglecting thermal broadening and assuming a constant tip density of states). Γ and Δ denote the quasiparticle-lifetime broadening and size of the gap.

Some superconductors (e.g. NbSe₂) have two gaps, and their DOS can be written as:

$$\frac{dI}{dV}(V) = \sum_{n=1,2} C_n \left| \operatorname{Re} \left[\frac{eV - i\Gamma_n}{\sqrt{(eV - i\Gamma_n)^2 - \Delta_n^2}} \right] \right| + D, \quad (2.18)$$

Where C_n are constant prefactors and D is an overall constant background.

2.5 Spectroscopic maps

In STM, we can retrieve information from real space. Besides the surface topography, spectroscopic data probes the local density of states. A supportive technique to extract information on the sample is spectroscopic imaging-STM (SI-STM). In this technique, the tip is scanned over the sample surface with a fixed tunneling resistance $R_t = V_t/I$, recording the topographic information. At each pixel of a topographic image, the scan and feedback are switched off to freeze the tip position (x,y and z). This allows the voltage to be swept to measure $I(V)$ and dI/dV over an extended voltage range, the latter being proportional to the local density of states. The bias is then set back to V_t , the feedback turned on, and the scanning resumed. The result is a topographic image measured at V_t and simultaneous spectroscopic images which can be reconstructed from the $I(V)$ and dI/dV data. Acquisition of such a spectroscopic map requires extreme stability of the tunnel junction over the time of the measurement. A map is typically composed of $\sim 10^4$ spectra, requiring acquisition times on the order of a week. This technique provides a very rich set of information.

2.5.1 Quasi particle interference (QPI)

By taking spectroscopic imaging maps, it will be possible to image the dispersion of quasiparticle states from the QPI patterns induced by impurity scattering. When quasiparticles disperse off the impurities, standing waves are formed. The dominant sets of quasiparticle momenta can be observed by taking the fourier transform of the real-space interference pattern (FFT-STIS) [20].

Chapter 3

Setup and construction of a milli-Kelvin STM

In this chapter the set-up and performance of a dilution-refrigerator based spectroscopic imaging scanning tunneling microscope is discussed. It operates at temperatures below 10mK and in magnetic fields up to 14T. The system allows for sample transfer and in situ cleavage. I present first results demonstrating atomic resolution and the multi-gap structure of the superconducting gap of NbSe₂ at base temperature. To determine the energy resolution of our system I have measured a normal metal/vacuum/superconductor tunneling junction consisting of an aluminum tip on a gold sample. Our system allows for continuous measurements at base temperature on time scales of up to 170 h [17].

3.1 Dilution refrigeration

One of the methods to cool down below 100mK is dilution refrigeration, which was first proposed by H. London in 1951 [28]. In this method the latent heat of mixing of the two Helium isotopes ³He and ⁴He are used for cooling. This section is based on these references [21, 29, 30].

The phase diagram of the mixture as a function of ³He content can be seen in Fig 3.1. During cooling down the ³He/⁴He mixture, two phases with different ³He concentration form (in the unstable region). At a temperature of 867 mK and a ³He concentration of 67.5% the lambda line meets the phase separation line. At this point the super fluidity of ⁴He disappears and further cooling down results in a formation of two fluid phases with different concentration of ³He: one phase which is rich in ⁴He (diluted phase) and one

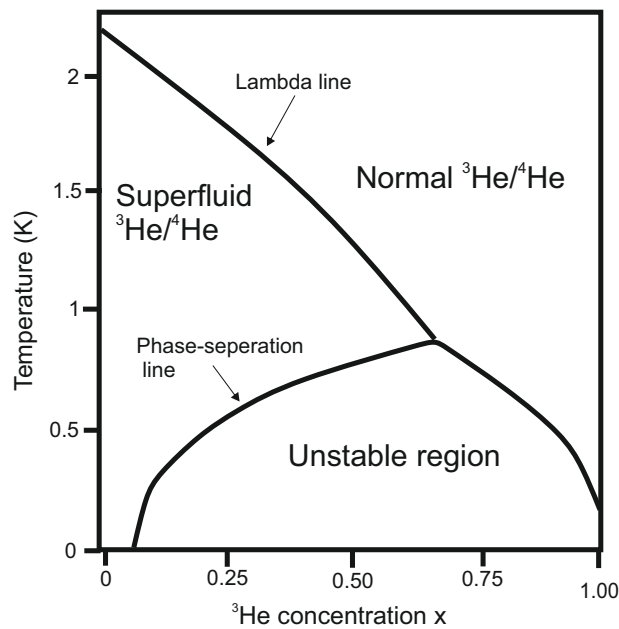


FIGURE 3.1: Phase diagram of a liquid ${}^3\text{He}/{}^4\text{He}$ mixture. The graph is reproduced from [30].

which is rich in ${}^3\text{He}$ (concentrated phase). The two fluid phases have different densities and thus there is a phase separation with diluted phase sinking to bottom due to its higher density. As can be seen in Fig 3.1, at 0 K the concentrated phase contains only ${}^3\text{He}$, whereas the diluted phase contains about 6.6% ${}^3\text{He}$ in ${}^4\text{He}$. This finite amount of ${}^3\text{He}$ in the diluted phase is necessary for the dilution refrigerator to operate.

The reason for this solubility can be explained by comparing the chemical potential of a single ${}^3\text{He}$ atom in the concentrated and diluted phase at $T = 0$ K. The driving force for solubility is because of the larger mass of ${}^4\text{He}$, which makes the zero point motion smaller than for ${}^3\text{He}$. As a consequence, the ${}^3\text{He}$ atoms are further apart from each other than the ${}^4\text{He}$ atoms. As the atoms in the ${}^4\text{He}$ concentrated phase can pack together more closely, the forces between the atoms are greater. Therefore, a single ${}^3\text{He}$ atom has a higher binding energy in a ${}^4\text{He}$ host than a ${}^3\text{He}$ host. However, since ${}^3\text{He}$ is a Fermion (due to its $1/2$ nuclear isospin), there will be an attractive interaction ($k_{\text{B}}T_{\text{F}}(x)$) as a function of concentration between two ${}^3\text{He}$ atoms. Eventually, the chemical potential of a ${}^3\text{He}$ atom in a dilute solution with a ${}^3\text{He}$ concentration x can be written as:

$$\frac{\mu(x)}{N_0} = -\epsilon(x) + k_{\text{B}}T_{\text{F}}(x),$$

$$k_{\text{B}}T_{\text{F}}(x) = (\hbar^2/2m^*)(3\pi^2xN_0/V_m)^{2/3} \sim x^{2/3}, \quad (3.1)$$

where N_0 is the Avogadro number, $\epsilon(x)$ is the binding energy of a single ${}^3\text{He}$ atom to

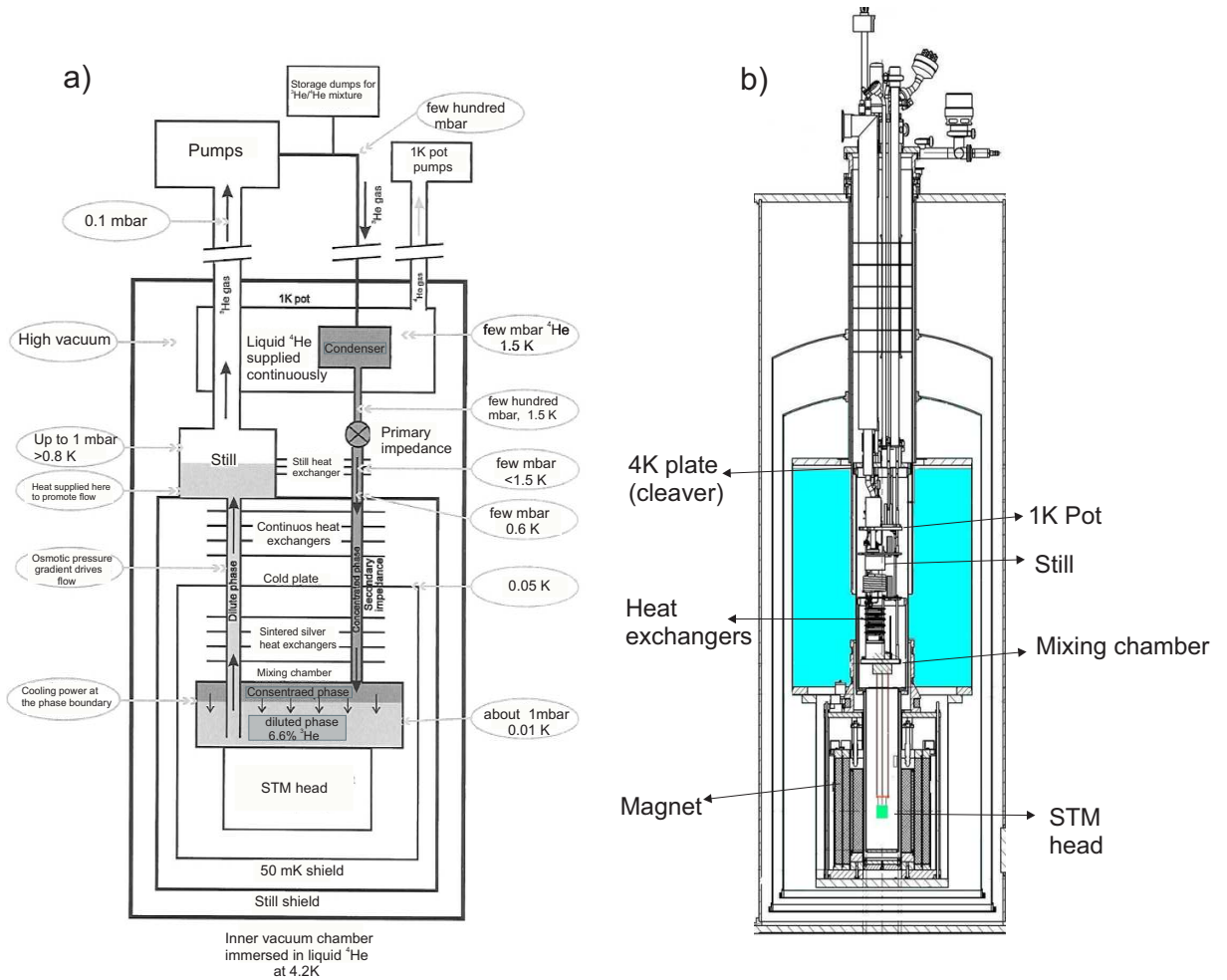


FIGURE 3.2: (a) Schematic of a dilution refrigerator taken from Oxford instruments. (b) Illustration of the dewar, insert and the different plates in the dilution refrigerator.

^4He host. In Eq. 3.1, at a concentration $x = 6.6\%$, the binding energy of the ^3He in the concentrated phase equals the binding energy of ^3He in the diluted phase.

3.1.1 Operation mechanism and components of a dilution refrigerator

A schematic illustration of our dilution refrigerator is shown in Fig. 3.2. The $^3\text{He}/^4\text{He}$ mixture circulates in a closed cycle. As it can be seen in Fig. 3.2a, the ^3He pressure reduces as it goes down through the different cooling stages. All the pressures inside the tubes inside and outside the insert are less than ambient pressure so that the mixture is less prone to diffuse out over time. At the beginning the mixture passes through liquid nitrogen and helium cool traps to eliminate the dirt which might leak from air. Afterwards the mixture enters the insert by first passing through the 1k pot in order to condense. 1K pot is connected to the main ^4He bath through a flow impedance. The pot is pumped by a rotary pump, so that the vapor pressure of ^4He is about 2-3 mbar and

therefore the temperature of the pot is about 1.8 K. Consequently, the mixture passes through impedances and heat exchangers, till eventually it reaches the mixing chamber.

The Mixing chamber (MC) is the coldest part of in the cryostat. In this part of the insert phase separation between the concentrated and diluted phases occurs. Inside the MC ^3He diffuses through the phase boundary from the concentrated phase to the dilute phase, whereas the ^4He acts as a suprafluid background and flows up to the Still plate due to the pressure difference between MC and the Still. The temperature in the Still is a bit higher than 800mK, such that ^3He is evaporated but ^4He stays as liquid.

^3He is pumped by a roots pump out of the Still to pipes installed outside of the cryostat at room temperature. At this stage ^3He passes through an intelligent gas handling (IGH) system, which controls the flow of the mixture. As it has been mentioned the Helium and Nitrogen cool traps are installed near the IGH where every time the mixture is cleaned before it enters the cryostat. In dilution refrigeration the experimental equipments are installed at the MC (since it has the lowest temperature), and the cooling power (\dot{Q}) is defined as the product between the flow of ^3He atoms crossing the phase boundary \dot{n} and the enthalpy difference between the diluted and concentrated phase. The enthalpy of the two phases can be known from specific heat measurements. After simplifying the enthalpies, the ideal cooling power inside the MC can be written in the equation:

$$\dot{Q} = \dot{n}(H_d(T) - H_c(T)) = 84\dot{n}T^2 [W]. \quad (3.2)$$

3.2 Setup and challenges

Over the past few years, a few ^3He -based STMs which can potentially reach temperatures down to 300mK have been developed [31–33]. Dilution refrigerator based designs, however, which can reach temperatures well below 100mK, are still rather rare [34–39]. Especially the set-up of UHV-compatible systems is a serious challenge, which was only recently achieved [38–40]. The technical difficulties in these systems are the vibrational decoupling of the pumping system, filtering of radio frequency (RF) interferences and electronic noise, and a limited choice of materials. RF filtering and shielding are very important [37], as external RF noise can severely limit the energy resolution to an effective "electronic temperature" significantly higher than the nominal temperature of the experiment.

Our millikelvin SI-STM has been developed based on a dilution refrigerator with a high field magnet (0 – 14T) supplied by Oxford Instruments [41]. The dilution refrigerator provides a cooling power of $\dot{Q}=400\mu\text{W}$ at 100mK. The design of the insert has been

modified to allow for a line-of-sight port for the sample transfer. It reaches a base temperature (without the microscope head and support structure) of 7mK at the mixing chamber as measured by a nuclear orientation thermometer. The design of our home-built STM head is based on the design by S.H. Pan [31, 42, 43]. Our head is optimized for high mechanical stiffness and good thermal conductivity by making the main body out of sapphire [44]. The microscope head is mounted on a copper base plate which is suspended by gold-coated copper rods from the mixing chamber plate as shown in Fig. 3.3a and b to place the STM head at the center of the magnet. The triangular walker prism is clamped between six piezo stacks [45] and hosts the scanner tube with the STM tip. The sample holder is clamped by an aluminum oxide plate to the main body. To allow for the sample transfer, the STM head is located 2cm off-center from the main axis of the magnet (leading to a magnetic field deviating by less than 1% from the specified field [46]). The STM base plate has a number of slits to avoid eddy current heating of the base plate while ramping the magnetic field. In order to check the motion of the walker, the position can be detected by a capacitive distance sensor consisting of concentric brass cylinders [20].

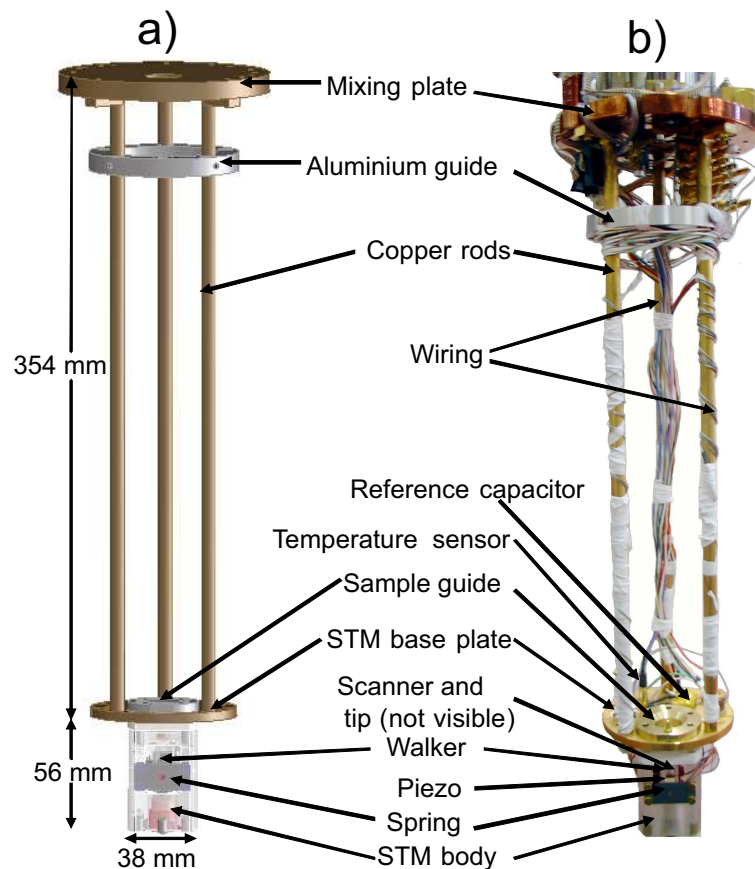


FIGURE 3.3: Schematic view of STM assembly below the mixing chamber plate. (a) and (b) are the computer aided design model and real images, respectively.

Samples can be exchanged by a vertical sample manipulator. For in-situ cleavage of

samples we have constructed a cleaving stage which simultaneously acts as a radiation shield when the manipulator is removed. The cleaving stage is mounted on the 4K plate of the dilution refrigerator, the design is depicted in Fig. 3.4a. The cleaver is operated by translating a rotation of the manipulator into a movement of the shutter of the cleaver, which knocks off a rod glued to the sample surface. The construction of the cleaver prevents uncleaved samples from being inserted into the STM as well as removal of the manipulator without closing the cleaver shutter.

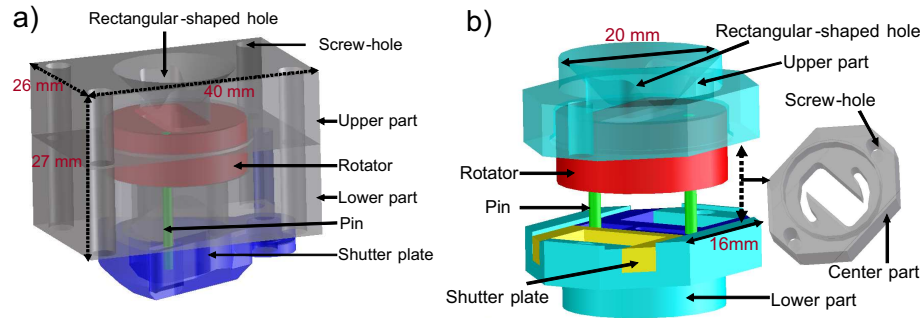


FIGURE 3.4: (a) Sample cleaver. The sample cleaver is mounted at the 4K-plate of the cryostat. It acts at the same time as a radiation shield to block thermal radiation from room temperature. The cleaving mechanism is operated by the sample transfer mechanism, allowing for transfer of the sample into the inner vacuum only after cleavage, (b) Shutter for thermal radiation shielding. The shutter is mounted on the still plate to block thermal radiation from the 4K-plate from reaching the sample. The shutter is opened and closed by rotation of the manipulator similar to the cleaver.

To prevent thermal radiation along the line of sight (which, apart from the cleaver, goes from room temperature to the mixing chamber plate) from heating up the mixing chamber plate and thus the STM, an additional mechanical shutter is mounted on the still plate (Fig. 3.4b), setting its temperature to $\approx 600\text{mK}$. Its functional principle is similar to that of the sample cleaver, with the difference that by turning a rotational insert, two shutter plates are moved apart or towards each other. The STM head is further shielded from thermal radiation by a cylinder attached to an intermediate cold plate (at $\sim 50\text{mK}$) to block thermal radiation from the IVC which is at 4K.

Due to the extreme sensitivity of the tunneling current to the tip-sample distance, the cryostat is mounted on a vibration-isolation table suspended on air springs [47]. All pumping lines run through vibration isolation consisting of wooden boxes filled with sand, the still line is additionally decoupled by two bellows. All gas lines and pumping tubes are clamped to the vibration table prior to their connection to the insert. Environmental RF noise can perturb the tunnel current thus increasing the effective temperature of the STM. All electric lines entering the insert except for the tunnel current go through RF filters at room temperature, which are effective in a frequency range from 10MHz to 10GHz [48]. The temperature of the mixing chamber is below 10mK

and the temperature of the STM head below 30mK (T_{STM}) as measured by calibrated RuO₂ sensors [49]. The STM head is controlled by a commercial DSP controller built by Soft DB [50] with the open source SPM control software GXSM [51, 52] and both home-built high-voltage amplifier and piezo motor controller. As a current amplifier, we use a commercial variable gain amplifier [53].

3.3 First results

I have carried out SI-STM measurements on a NbSe₂ single crystal at the base temperature $T_{\text{MXC}} \approx 10\text{mK}$. Afterwards I performed measurements with an aluminum tip and a Au crystal as a sample, in order to determine the electronic temperature of the STM.

3.3.1 Measurements on NbSe₂ single crystal

A mechanically cut Pt-Ir wire was used for the tip, and then cleaned in-situ by field emission on a gold single crystal at voltages up to 180V applied between the tip and sample. Figure 3.5a shows a topographic image of an NbSe₂ surface, revealing atomic resolution as well as the known charge density wave order [55]. From the line cut profile in Fig. 3.5b, the vertical stability of the instrument can be estimated to be better than 5pm.

For the spectroscopy, the tunneling spectra were measured under open feedback loop conditions. The dI/dV signal were measured using a lock-in amplifier. In Fig. 3.5c I present the spatially averaged spectra of ~ 6000 differential conductance spectra taken over a large area spectroscopic map showing two different gap values. The gaps were determined by fitting them with the sum of two Dynes gap equations Eq. 2.18. The size of the large gap $\Delta_1 \approx 1.2\text{meV}$ and of the small gap $\Delta_2 \approx 0.4\text{meV}$ have been found, comparable to previous reports [56].

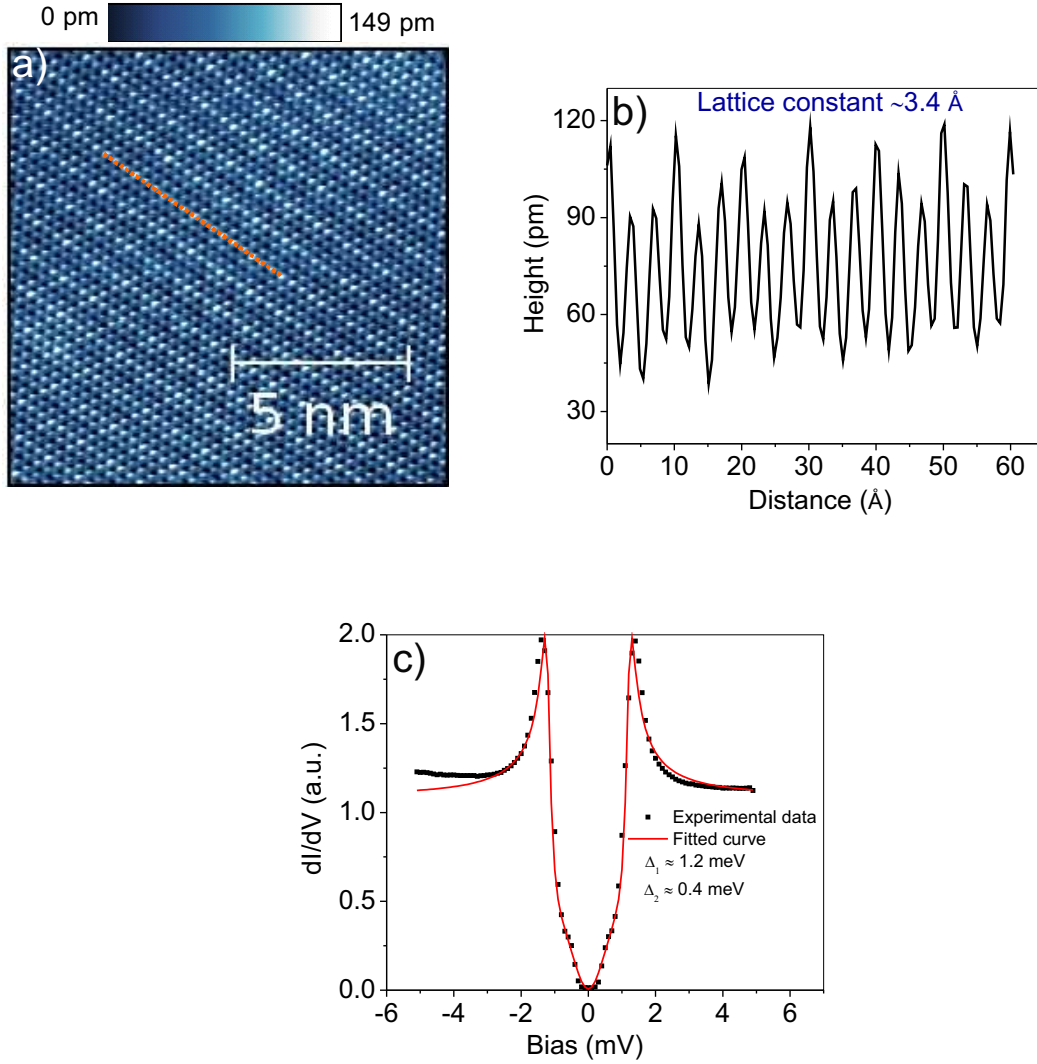


FIGURE 3.5: (a) Atomically resolved topography of a cleaved NbSe₂ surface ($12 \times 12 \text{ nm}^2$, $V = 90 \text{ mV}$ and $I = 0.5 \text{ nA}$) measured at $T_{\text{MXC}} \approx 10 \text{ mK}$. Besides the surface atomic structure, a modulation due to formation of a charge density wave can be seen. (b) Line cut along an atomic row, it can be seen that the residual noise is below 5 pm [54]. (c) Spatially averaged spectra taken on NbSe₂ (spectroscopy set-point: $V = 90 \text{ mV}$, $I = 1 \text{ nA}$, lock-in modulation of $100 \mu\text{V}$, and frequency of 511 Hz) at base temperature, the solid line shows a fit of eq. 2.18 to the data.

3.3.2 Measurements of Aluminum tip on gold sample

To determine the energy resolution of our dilution-refrigerator based SI-STM, I have performed measurements on a superconductor-vacuum-metal junction, using a piece of aluminum wire as material for the STM tip and a Au(111) crystal as a sample [57]. Aluminum is a conventional superconductor described well by BCS theory and has a critical temperature $T_c \simeq 1.2 \text{ K}$ [34]. The aluminum tip has been cleaned in-situ by field emission as described above. Measurements have been carried out at $T_{\text{MXC}} \approx 10 \text{ mK}$. A modulation in the range of $5 - 50 \mu\text{V}$ has been applied to the sample.

The spectra have been modeled following Bardeen's theory of tunneling [23], accounting for thermal broadening due to the Fermi distribution and lock-in broadening [58]. The tunneling conductance can be expressed as Eq. 2.10. The BCS gap equation for $\rho_{Al}(E)$ is obtained using Eq. 2.15. The broadening due to the lock-in modulation V_{RMS} is accounted for from the convolution of Eq. 2.10 with a half-circle, applying Eq. 2.12.

The calculated spectrum from the above equations has been fitted to the measured data using a non-linear least squares algorithm, the free parameters were a proportionality constant, a constant offset, the gap width Δ , an energy offset (due to a small instrumental offset in the bias voltage) and the temperature. In Fig. 3.6a, the fitted spectrum is plotted together with the measured one and the residuum. A gap size of $188\mu\text{eV}$ has been found close to previously measured values ($\approx 175 - 190\mu\text{eV}$) [33, 34] and a temperature of $\approx 140\text{mK}$. This value constitutes an upper limit for the real electronic temperature. The preparation of the tip on a gold crystal likely leads to a thin gold layer on the tip apex. Though this gold layer will become superconducting due to the proximity effect [59], this will introduce a finite density of states in the gap and reduce the height of the coherence peaks – potentially leading to a higher apparent electronic temperature. It should also be noted that spectra vary considerably for different tips; depending on the tip condition, sometimes no superconducting gap is observed at all. The difference between the temperature of the STM head ($T_{STM} \approx 30\text{mK}$) and the electronic temperature indicates that RF noise still leads to a non-negligible broadening of the tunneling spectrum - despite careful filtering of all signal lines at room temperature. Additional filtering at low temperature should allow us to improve our spectroscopic resolution significantly [37].

In Fig. 3.6b, I display the dI/dV spectra measured as a function of magnetic field with a lock-in modulation of $20\mu\text{V}$. The superconducting gap with coherence peaks at energies $\pm 170\mu\text{V}$ survives up to a magnetic field between 27.5mT and 30mT , which is almost three times higher than the critical field of bulk Al ($\approx 10\text{mT}$). This increase in magnetic field has been observed in previous STM experiments with aluminum and lead tips [34]. This may occur due to the tip apex having a smaller size than the coherence length, where the superconductivity can survive up to magnetic fields higher than the critical field of the bulk material [60].

I have also measured the superconducting gap with lock-in modulation applied in the range of $5 - 50\mu\text{V}$, as presented in Fig. 3.6c. It is clearly visible that higher lock-in modulation broadens the coherence peaks and affects the shape of the superconducting gap. Calculated spectra according to Eq. 2.10-2.12 are shown in Fig. 3.6d and compare well to the measured ones.

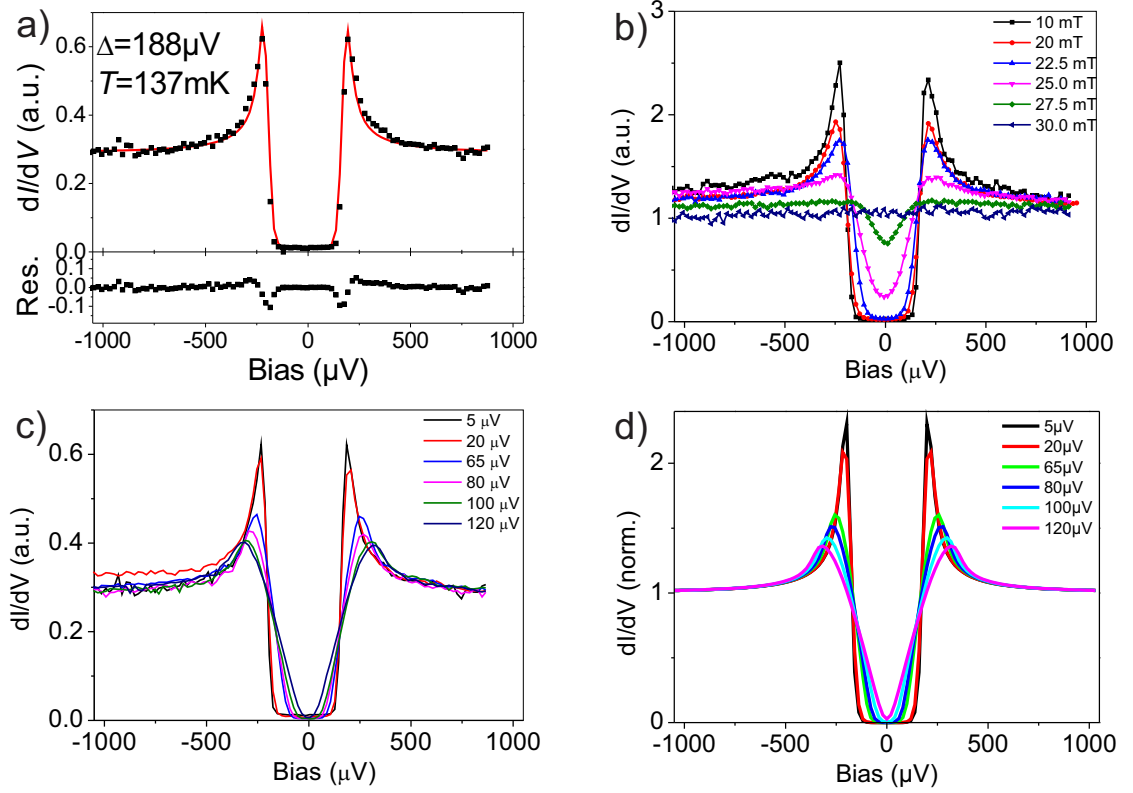


FIGURE 3.6: Tunneling Spectroscopy of a Gold-Vacuum-Aluminum-Junction at $T_{\text{MXC}} \approx 10\text{mK}$ with $V = 2\text{mV}$ and $I = 3\text{nA}$ (a) Fit of Eq. 2.12 to a spectrum of the Au-Vacuum-Al junction for a lock-in modulation of $5\mu\text{V}$, yielding an electronic temperature of $\approx 140\text{mK}$. (b) Tunneling spectroscopy as a function of applied magnetic field. The superconducting gap disappears at magnetic fields on the order of 30mT . (c) and (d) tunneling and calculated spectra as a function of lock-in modulation (frequency: 511Hz).

In conclusion, we have demonstrated successful operation of a dilution-refrigerator based SI-STM with *in situ* sample exchange and a base temperature below 10mK .

Chapter 4

Al-Al Josephson junction

When two superconductors are coupled to each other through a weak link (e.g. vacuum or insulator), a device known as Josephson junction is formed. This device proposed by Brian Josephson [61], can transfer current (electrons) without any voltage applied. Josephson tunneling is Cooper pair tunneling between two superconductors separated by a thin barrier. It is potentially possible to spatially resolve the superconducting order parameter (SOP) of the sample surface if the SOP of the tip is known, since Cooper pairs tunnel from similar SOP [62]. In this chapter I discuss about the supercurrent, i.e the superconducting current flowing without dissipation, which I measured by tunneling cooper pairs between a superconducting tip and a superconducting sample (S-S). With this supercurrent, I want to characterize the STM electronics and circuitry, as well as the temperature. Good reviews on Josephson junctions can be found in e.g.[22, 63].

4.1 Introduction on Josephson coupling

Cooper pair tunneling does not involve excitations and can occur even without bias across the junction, contrary to quasiparticle tunneling. The wavefunction of an isolated superconductor is:

$$\psi = |\psi| \exp(i\varphi), \quad (4.1)$$

with phase φ . In Josephson junctions, the distance between superconducting electrodes which is separated by an insulating barrier (e.g. vacuum) will be in the order of few Ångstroms. Because of this short distance, the wavefunctions of the two superconducting electrodes can overlap, which allows the Cooper pairs to tunnel. The Josephson supercurrent which flows at zero bias between the two superconducting electrodes is:

$$I_S = I_{Max} \sin(\varphi), \quad (4.2)$$

where I_{Max} is the critical current, that is the maximum supercurrent that the junction can possess before switching to the dissipative state, and $\varphi = (\varphi_2 - \varphi_1)$ is the phase difference of the wave functions of the two superconducting electrodes. This equation describes the DC-Josephson junction, as shown in Fig. 4.1. I_{Max} can be calculated by the Ambegaokar-Baratoff relation [64]:

$$I_{Max} = \frac{\pi\Delta(T)}{2eR_N} \tanh \frac{\Delta(T)}{2k_B T}, \quad (4.3)$$

where R_N is the normal state resistance of the junction, e is electron charge, $\Delta(T)$ is the superconducting gap and $k_B T$ is the thermal energy, with $k_B = 86.17 \mu\text{eV/K}$, being the Boltzmann constant and T the temperature of the system. In the low temperature limit, Eq. 4.3 reduces to

$$I_{Max} = \frac{\pi\Delta(0)}{2eR_N}. \quad (4.4)$$

When a voltage V is applied to the Josephson junction, the phase difference $\varphi = (\varphi_2 - \varphi_1)$ will follow equation:

$$\frac{d\varphi}{dt} = \frac{2e}{\hbar} V \quad (4.5)$$

resulting in a linear increase of the phase φ with time. As a consequence, an oscillating supercurrent develops across the junction $I_S = I_{Max} \sin[2\pi\nu t + \varphi(0)]$, characterized by the frequency $\nu = (2e/h)V$. This phenomenon, is known as the AC Josephson effect, which associates voltage and frequency only through fundamental constants (e and h) and the value $2e/h$ has been adopted as frequency-to-voltage conversion. The energy stored in the junction is given by the integral $E = \int I_S V dt$. After substituting the Josephson relations, the integral results in the equation:

$$E = \frac{\hbar I_{Max}}{2e} (1 - \cos \varphi) = E_J (1 - \cos \varphi), \quad (4.6)$$

where $E_J = \frac{\hbar}{2e} I_{Max}$ denotes the Josephson coupling energy. In the low temperature limit, it can be simply calculated using the relation:

$$E_J = \frac{R_Q \Delta(0)}{2R_N}, \quad (4.7)$$

where $R_Q = h/(2e)^2 \simeq 6.45 \text{ k}\Omega$ is the quantum resistance.

In the next section, I will show the Josephson coupling results which we obtained with an Aluminum coated tip by field emission on a polycrystalline high purity (99.9%) Aluminum sample.

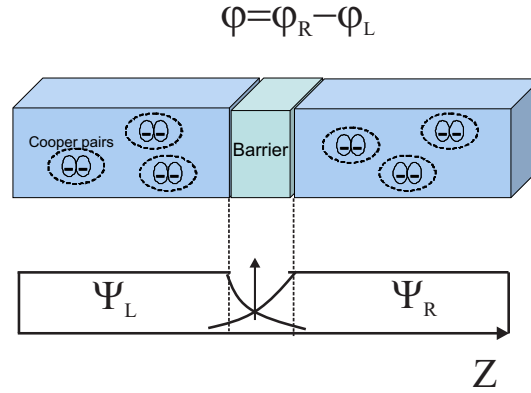


FIGURE 4.1: Josephson tunneling from two superconducting electrodes. Ψ_L and Ψ_R are the left and right pair wavefunctions.

4.2 Data on Al-Al junction

In this section, I will show our Josephson-STM results. The tip and the sample are both considered the superconducting electrodes, whereas the vacuum is regarded as the thin insulating barrier. In Fig. 4.2, the schematic of the measurements in this chapter are shown, where the data are obtained by Pt-Ir tip coated with aluminium after field emission, on an aluminium sample ($T_{c,Al} = 1.2\text{K}$).

After having superconducting tip and sample, the conductance spectra show a different behavior. If the superconductors are the same material, the quasi-particle excitation peaks in the tunneling conductance will be at voltage $V = \pm 2\Delta/e$. In the case where the tip and sample do not have the same gap size, the coherence peaks will be found at $V = \pm(\Delta_1 + \Delta_2)/e$. As it can be seen in Fig. 4.2b, by having double the gap size of aluminum conductance spectra, the superconducting nature of the tip will also be confirmed.

An important feature which can be studied in S-S Josephson junctions is the supercurrent. Measuring the supercurrent is dependent on the Josephson coupling energy E_J (Eq. 4.7) and thermal energy $k_B T$. Since all our measurements were taken at base temperature, the thermal energy is constant. The only parameter that can change E_J is R_N (the resistance of the junction). If the junction resistance value has a comparatively high value (here $R_N > 2\text{M}\Omega$), then there is no supercurrent peak in the conductance spectra (Fig. 4.2b). On the other hand, if the junction resistance value has a low value (here $R_N < 2\text{M}\Omega$), then supercurrent peak in the conductance spectra is observed (Fig. 4.2c). In our measurements above contact resistance of $R_N = 2\text{M}\Omega$, the signal to noise ratio for observing the supercurrent was not sufficient. For Aluminium which has a superconducting (SC) gap size $\Delta \simeq 0.2\text{ meV}$, E_J can be estimated to be $E_J = \frac{645}{R_N}\text{ meV}$ (Eq. 4.7), which means that when $R_N \simeq 1\text{ M}\Omega$, $E_J \simeq 0.645\text{ }\mu\text{eV}$, less than $k_B T \simeq 2\text{ }\mu\text{eV}$. Below

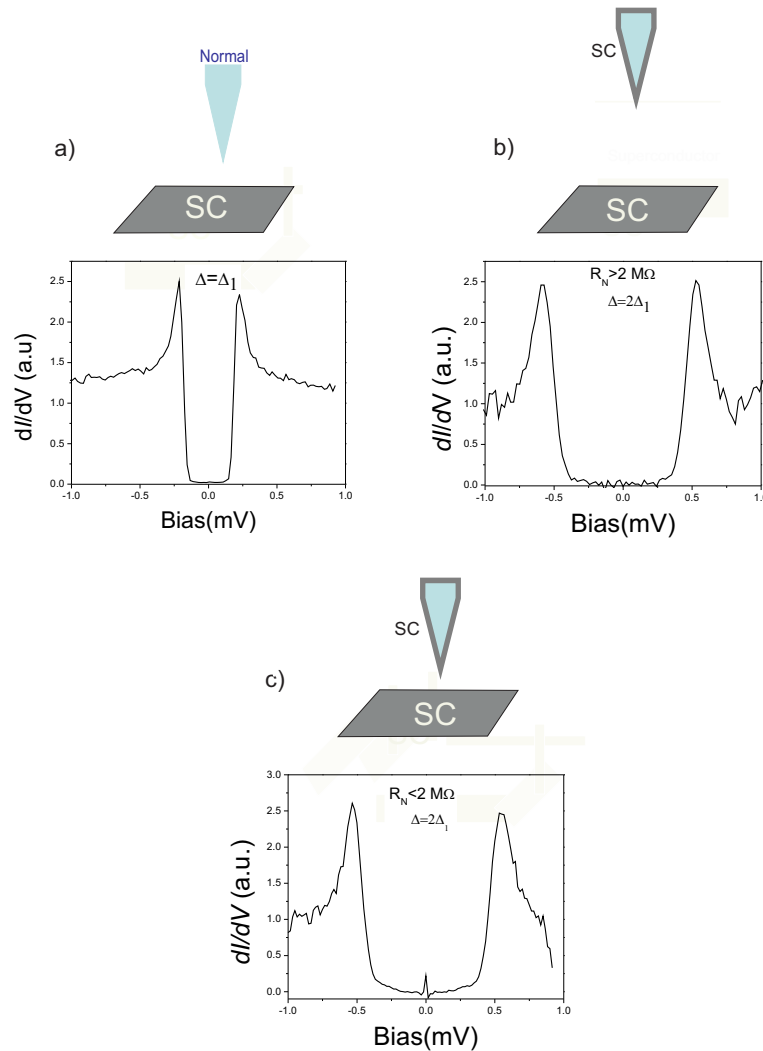


FIGURE 4.2: (a) Normal tip on superconducting sample, coherence peaks appearing at $V = \pm\Delta/e$. (b) Superconducting tip on superconducting sample, coherence peaks appearing at $V = \pm 2\Delta/e$. (c) When the tip gets closer to the surface, E_J increases thus the conductance spectra shows the Josephson supercurrent peak at zero bias.

the contact resistance of $2 \text{ M}\Omega$, we expect considerable Josephson coupling, which would be observed in the conductance spectra as zero bias peak. The height of the zero bias Josephson peak depends on the contact resistance, which is proportional to the spectroscopic set points ($R_N = V_t/I_t$). The lower R_N , results in a higher Josephson coupling E_J and thus, the zero bias Josephson conductance peak will be higher. As it can be seen in Fig. 4.3a, the set of data obtained as a function of conductance ($G_N = 1/R_N$) from $0.5 \mu\text{S}$ to $2.3 \mu\text{S}$ ($\sim 1.9 \text{ M}\Omega$ to $\sim 435 \text{ K}\Omega$) in the range of $\pm 75 \mu\text{V}$, shows that the Josephson peak (supercurrent) increases by increasing the setpoint conductance. The junction resistance cannot be arbitrarily small, and there are two factors restricting the range of this parameter. First, because of the small junction area, the current flux are high and the junction resistances below few tens of $\text{K}\Omega$ will result in the destruction of the superconductivity in the tip due to high current densities. A second limit on

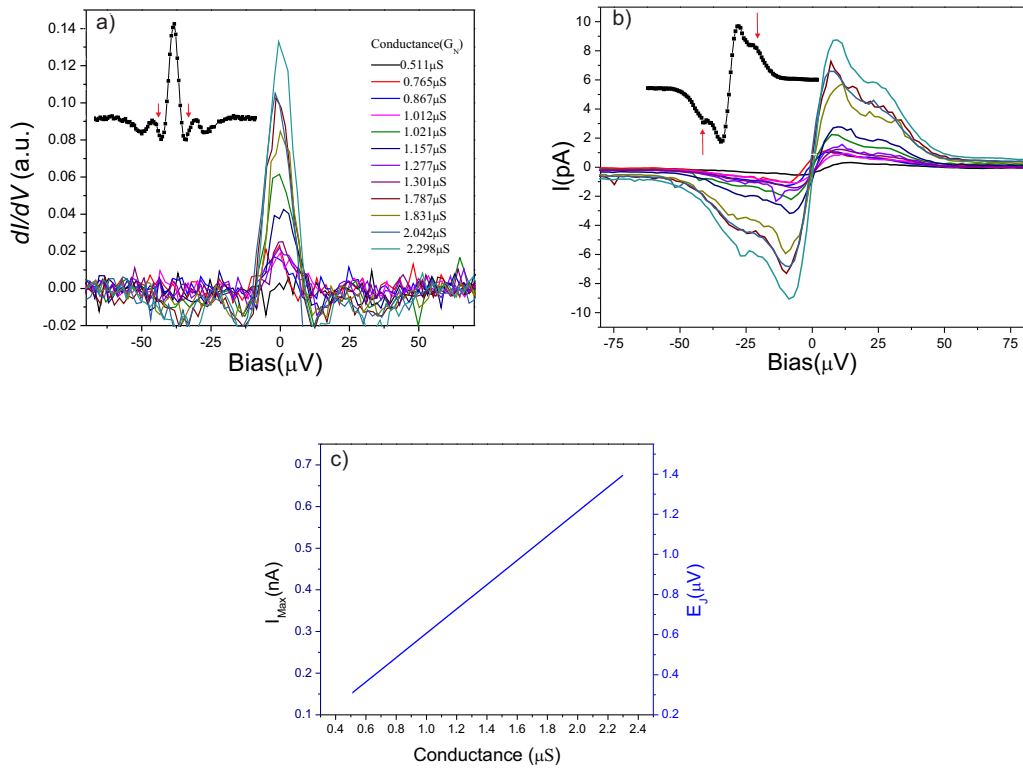


FIGURE 4.3: Data obtained as a function of conductance: (a) dI/dV spectra showing the Josephson peak as function of Resistance (conductance) in the range of $\pm 75 \mu V$. In the inset a typical spectra shows the Josephson peak and two additional bumps (marked with red). (b) $I - V$ curves as function of Resistance (conductance) in the range of $\pm 75 \mu V$, at zero bias the peak denotes the super current. In the inset a typical curves is shown, the shoulders are marked. (c) The Josephson coupling energy (E_J) and critical current (I_{Max}) as a function of conductance.

the resistance is the transition from vacuum tunneling to a point contact regime [65]. Experimentally, we measured at resistances down to $\sim 435 K\Omega$.

In the next section, I will quantitatively analyze the data with different models, in order to characterize the STM- circuitry and learn more about Josephson coupling.

4.3 Characterizing the STM circuit

In order to quantitatively analyze the data, we focus on the $I - V$ spectra. In a very small energy range ($\pm 75 \mu V$), supercurrent peak and two smaller shoulders (peaks) in the vicinity of the Fermi level appear (Fig. 4.3).

Normal-metal STM studies reveal only the quasi-particle excitation spectrum. However, an STM with a SC tip is a local Josephson probe and can access the SC pair wave function directly on a length scale smaller than or comparable to the SC coherence

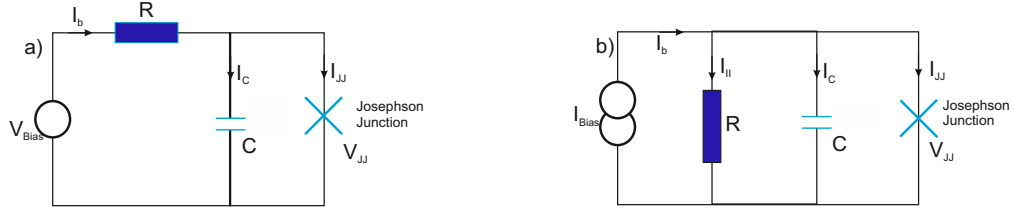


FIGURE 4.4: Schematic of the circuits discussed in RCSJ model. (a) Voltage-bias configuration. (b) Current-bias configuration. The two biasing schemes are equivalent if $V_b = RI_b$, reproduced from [63]

length ξ . There have been some Josephson STM articles [65–69]. For instance, in the work done by Naaman et. al in 2001 [65], they used SC Pb-Ag tip on Pb sample and later on NbSe₂ and BSSCO samples [67]. In this thesis I used three different models to analyze the data. With these three models, I extract the Josephson temperature as well as components of the Josephson circuit such as environmental impedance and the capacitance. At the end of the chapter, there is a comparison between the various models. All the fits in this chapter are obtained with least square fit except the last model which was fitted with educated guess.

4.3.1 The RCSJ Model

In order to analytically model a Josephson junction in nanometer scale, it is necessary to consider the circuit and the electromagnetic environment of it. For Josephson-STM, where the junction is on the order of few nanometers, the capacitance is very small (on the order of femto Farad), and the charging energy is significant ($E_C = 2e^2/C$ for Cooper pairs). In Fig. 4.4, a general scheme of a resistively and capacitively shunted junction (RCSJ) is shown. In this simple model, the dissipation due to the environment from the resistance R is assumed to be linear and frequency independent. The two configurations are equivalent if the relation $V_b = RI_b$ is satisfied. The time dependence of the phase φ across the junction can be calculated by equating the bias current I_b to the total current, and can be written as:

$$\begin{aligned}
 I_b &= I_{Max} \sin \varphi + \frac{V}{R} + C \frac{dV}{dt} \quad (\text{Current - bias}), \\
 V_b &= RI_{Max} \sin \varphi + V + RC \frac{dV}{dt} \quad (\text{Voltage - bias}).
 \end{aligned}
 \tag{4.8}$$

By using the second Josephson equation (Eq. 4.5), the second order differential equation emerges:

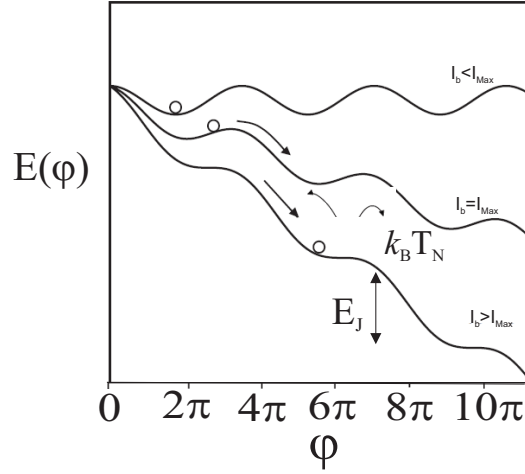


FIGURE 4.5: Josephson phase dynamics of the washboard potential in the classical thermal fluctuation regime. Reproduced from [67]

$$\frac{2e}{\hbar}I_b = \frac{2e}{\hbar}I_{Max} \sin \varphi + \frac{\dot{\varphi}}{R} + C\ddot{\varphi}, \quad (4.9)$$

where C indicates the capacitance inside the circuit. As long as $I_b \ll I_{Max}$, Eq. 4.9 has a constant solution, with $\varphi = \arcsin(I_b/I_{Max})$, for any arbitrary values of C and R . When $I_b > I_{Max}$, the junction switches to voltage-bias state, and the $I_b - V$ curve, is dependent on C and R parameters, having time-dependent solution.

The thermal noise on a Josephson junction, gives rise to Nyquist noise (I_n) and can be described in the equation:

$$\langle I_n(t)I_n(t + \tau) \rangle = \frac{2k_B T}{R} \delta(\tau), \quad (4.10)$$

where $\delta(\tau)$ is the δ -function, and I_n is the fluctuating current originating from the noise in the resistor. In this model, as it can be seen in Fig. 4.5, one can show the dynamics of the phase φ in a Josephson junction by a point particle with mass proportional to C and position φ , moving in a periodic washboardlike potential landscape $E(\varphi) = (1 - \cos \varphi)E_J$ (Eq. 4.6). In this case if the junction resistances are very high (very shallow potential), then the motion of the phase is completely stochastic by thermal fluctuations ($E_J < k_B T$). By reducing the resistance, the phase spends on average more time near the minima of $E(\varphi)$. This problem was first encountered by Ivanchenko and Zil'berman [70] in 1969.

In the case when $E_C \gg E_J$, the capacitance C can be neglected and thus the second derivative in the phase in differential Eq. 4.9 can be eliminated, and it can be written as:

$$\frac{2e}{\hbar}(I_b + I_n) = \frac{2e}{\hbar}I_{Max} \sin \varphi + \frac{d\varphi}{dt} \frac{1}{R}. \quad (4.11)$$

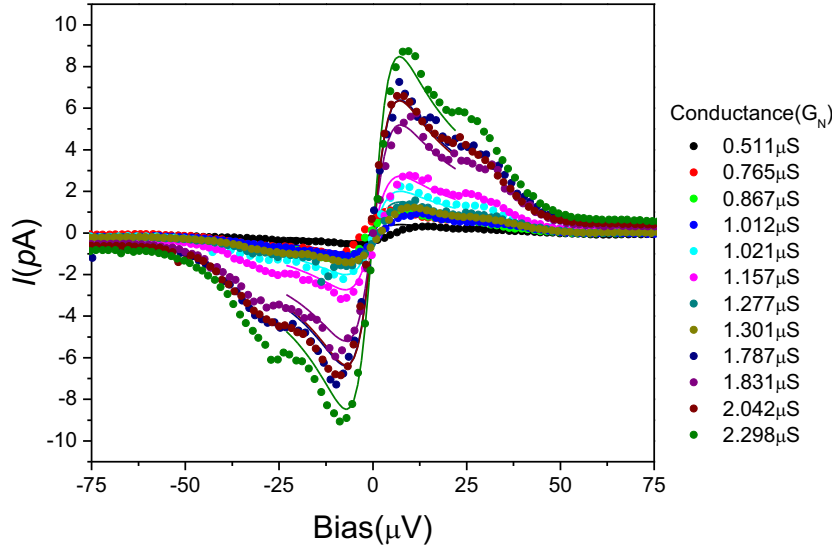


FIGURE 4.6: Fitting the data with RCSJ model, as in Eq. 6.1.

From equation 4.11, the Cooper pair current in the Josephson junction as a function of thermal fluctuations can be analytically expressed in the form

$$I = I_{Max} \langle \sin \varphi \rangle = I_{Max} \times \text{Im} \left[\frac{\mathbb{I}_{1-i\eta}(\alpha)}{\mathbb{I}_{-i\eta}(\alpha)} \right], \quad (4.12)$$

where

$$\alpha = \frac{E_J}{k_B T}, \quad (4.13)$$

$$\eta = \frac{I_b}{I_{Max}} \alpha = \frac{V_b/R}{I_{Max}} \alpha, \quad (4.14)$$

where \mathbb{I}_m are the modified Bessel functions of the first kind and complex order m . The larger the ratio α , the steeper would the Josephson supercurrent be, as it approaches to I_{Max} . With Eq. 4.12, It is possible to fit the data as shown in Fig. 4.6 and derive the temperature ($T_{mean} = 383 \pm 40$ mK) and the resistance ($R_{mean} = 487 \pm 40 \Omega$).

4.3.1.1 Phase diffusive model

In the limiting case for $\alpha \ll 1$ (in Eq. 4.13), a simple analytic form for the $I - V$ characteristics of the thermally fluctuated Josephson currents can be used [70],

$$I(V) = A \frac{V}{V^2 + V_P^2}, \quad (4.15)$$

$$A \equiv \frac{I_{Max}^2 Z_{Env}}{2}, \quad (4.16)$$

$$V_P = (2e/\hbar)Z_{Env}k_B T_n, \quad (4.17)$$

where V_P is the voltage at which the peak in the Josephson current appears. These equations are valid when the capacitances in the circuit drop out and charging effects are no longer present [71]. The thermal fluctuations are generated by a resistor Z_{Env} at a noise temperature T_n ; both of these parameters depend on the experimental setup. The measured $I - V$ characteristics for Al/I/Al STM Josephson junctions near zero bias with various $R_N(G_N)$ have been fitted to Eq. 4.15 depicted in Fig. 4.7a. There are only two parameters, A (illustrated in Fig. 4.7b) and V_P (shown in Fig. 4.7c). A shows a parabolic relation by increasing the conductance $A = 0.5(\pi\Delta/2e)^2 Z_{Env} G_N^2$, and from the fit we can derive the $Z_{Env} = 598\Omega$. V_P shows a constant behavior since it is just proportional to the environmental impedance and the noise temperature. It is also the bias of the position of the peak in the $I - V$ curve, which is on average $8.54 \mu V$. By having Z_{Env} and V_P , it is possible to derive T_n from Eq. 4.17 which has the mean value of 374 mK. From Eq. 4.15 and Eq. 4.7, we can plot all the fitted data as a function of conductance (G_N) in the equation:

$$\begin{aligned} y &= \sqrt{(4e/\hbar)A/V_P}, \\ x &= G_N = 1/R_N. \end{aligned} \quad (4.18)$$

This line is expected to have zero intercept and slope of $m = \pi\Delta/(2e\sqrt{k_B T_J})$ (or $I_{Max}R_N/\sqrt{k_B T_J/e}$). By fitting the set of data with the line from Eq. 4.18 and deriving the slope, we can calculate the Josephson temperature (T_J) as shown in Fig. 4.7d. The Josephson temperature can be regarded as the Cooper pair tunneling temperature, which is affected by the circuit, similar to the electronic temperature. T_J and T_n are physically the same but have different mathematical approaches to be obtained. Since the slope is $0.0548 \times 10^{-7} V^{0.5}$ the Josephson temperature can be calculated with equation: $T_J = \frac{1}{4k_B}(\frac{\pi\Delta}{m})^2$, which is equal to 336mK. This value is a bit higher than the electronic temperature (mentioned in the previous chapter). In this model, the fit is limited to $\pm 25\mu V$, which is close to the place where there is a shoulder.

The fitted values are very close to the values of the previous model (Fig. 4.8). The average temperature and resistance in both models are very close to each other. From these comparisons, we can conclude that in fact the limiting case for $\alpha \ll 1$ is valid for this case.

In order to include the shoulder to the model, we added Lorentzian peak to Eq. 4.15, which is composed of height (H), width (w), and center of the peak (x_0), as shown

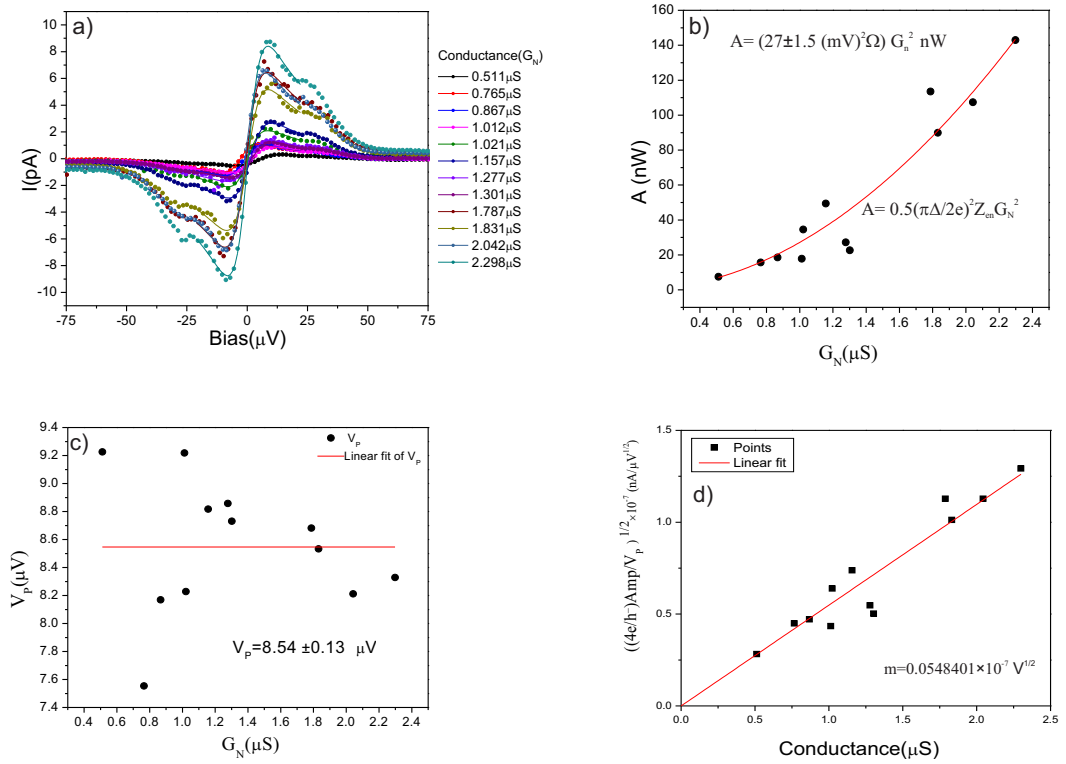


FIGURE 4.7: (a) Data and fits from different conductances. The fitting range covers till the shoulder. (b) Fits of A as a function of conductance. It shows a parabolic behavior, derived from Eq. 4.16 and Eq. 4.4, the red line shows the parabolic fitting, the coefficient is proportional to the impedance. (c) Fits of V_P , which shows a nearly constant behavior. (d) Linear fit to retrieve the Josephson temperature, which is proportional to the slope of the fit: 336mK.

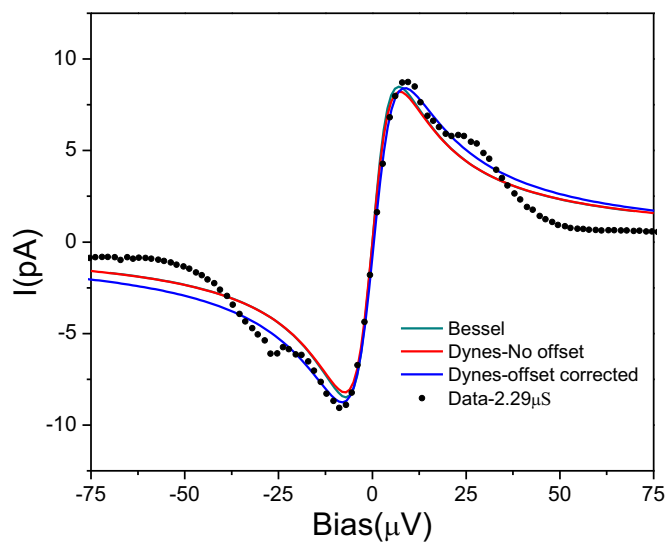


FIGURE 4.8: Comparison between the fitted models in the two models. As it is shown, the two models are very close to each other.

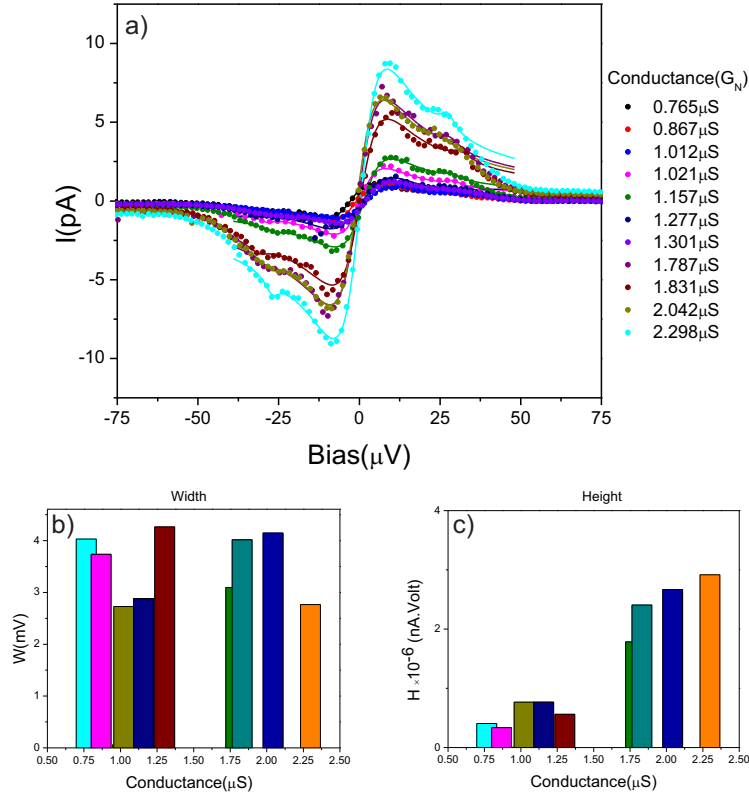


FIGURE 4.9: (a) Lorentzian fit with Eq. 4.19. (b) The width and (c) The height of the shoulder obtained from the fit.

in Eq. 4.19. After fitting the data (Fig. 4.9a), we see that for almost all the data, $x_0 \simeq 28 \mu V$, which can indicate that this value (center of the peak, i.e where the shoulder is located) is a property of the circuit. In fact this bias corresponds to frequency $\omega = 2eV/\hbar \sim 85$ GHz. This frequency can represent the resonance frequency of the circuit. The resonance frequency is itself dependent on the electronic circuit, the length of the tip and the environmental noises. The height of the shoulder increases with increasing the conductance, whereas the width tends to stay constant (Fig. 4.9b,c).

$$I = \frac{Amp \times V}{V^2 + V_p^2} + \frac{|W \times H|}{(V - |x_0|)^2 + W^2} - \frac{|W \times H|}{(V + |x_0|)^2 + W^2} \quad (4.19)$$

4.3.2 Quantum fluctuations model (Ingold model)

When the size of the junction is reduced, the quantum effects should be taken into consideration. Ingold et al. [71, 72] developed a model which expresses the formation of

the Josephson peak, being independent of the high-frequency behavior of the environment. In this approach a Hamiltonian describing the influence of the electromagnetic environment on an ultrasmall Josephson junction has been introduced, and the Cooper-pair tunneling rate has been derived. By neglecting the quasi-particle excitation, the Hamiltonian can be written as:

$$H = \frac{Q^2}{2C} - E_J \cos(\varphi) + \sum_{n=1}^N \left[\frac{q_n^2}{2C_n} + \left(\frac{\hbar}{e} \right)^2 \frac{1}{2L_n} \left(\frac{\varphi}{2} - \frac{e}{\hbar} Vt - \varphi_n \right)^2 \right]. \quad (4.20)$$

H describes a Josephson junction coupled to environmental modes. The junction is characterized by a capacitance C , carrying the charge Q , and a coupling term, which depends on the phase difference φ across the junction. C_n and L_n are capacitances and inductances respectively. The total Cooper pair current can be calculated using the relation [72]:

$$I(V) = 2e[\vec{\Gamma}(V) - \overleftarrow{\Gamma}(V)] = \frac{\pi e E_J^2}{\hbar} [P(2eV) - P(-2eV)], \quad (4.21)$$

where $\vec{\Gamma}(V)$ and $\overleftarrow{\Gamma}(V)$ are the forward and backward tunneling rate and $P(E)$ is the probability that a Cooper pair emits the energy E to the environment.

In order to derive the probability function $P(E)$, another paper from Ingold et al.[73] can be taken into consideration,

$$P(E) = Inh(E) + \int_{-\infty}^{+\infty} \mathbf{K}(E, \omega) P(E - \hbar\omega) d\omega, \quad (4.22)$$

$$Inh(E) = \frac{1}{\pi \hbar} \frac{D}{D^2 + E^2/\hbar^2}, \quad (4.23)$$

$$D = (\pi k_B T / \hbar) \times (R/R_Q), \quad (4.24)$$

$$\mathbf{K}(E, \omega) = \frac{E/\hbar}{D^2 + E^2/\hbar^2} k(\omega) + \frac{D}{D^2 + E^2/\hbar^2} K(\omega). \quad (4.25)$$

where the inhomogeneity ($Inh(E)$) corresponds to the $P(E)$ for a purely ohmic environment in the limit of near zero junction capacitance and high temperatures. $\mathbf{K}(E, \omega)$ is the integral kernel and is a complex function, where $K(\omega)$ is the Hilbert transform of $k(\omega)$ (See reference [73] for the complete set of equations). For the case where the external circuit can be described by a resistance R in series with an inductance L , \mathbf{K} will be a function of $\omega_C = 1/RC$ (inverse relaxation time), $\omega_S = 1/\sqrt{LC}$ (resonance frequency of the undamped circuit) and $Q = \frac{\omega_C}{\omega_S} = \frac{\sqrt{L/C}}{R}$ (quality factor). Therefore by fitting the $P(E)$ -theory model with the data we can derive the components in the STM circuit (R, C, L). Additionally it is possible to derive the temperature (T), since it is related to D (Eq. 4.24).

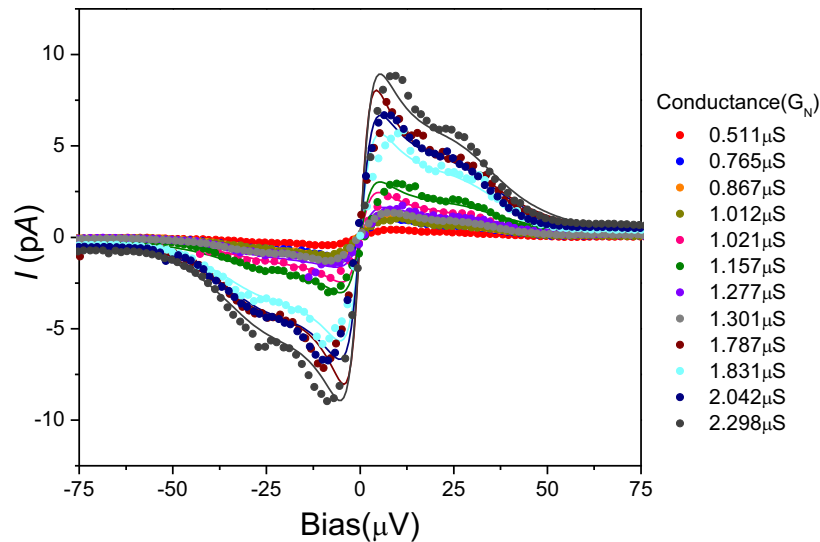


FIGURE 4.10: Fitting with P(E) theory model, as it can be seen the fits cover the whole data set.

It is now possible to calculate the function $P(E)$ numerically from the integral in Eq. 4.22, and then $I(V)$ from Eq. 4.21. The integral equation can be solved by iteration starting with the inhomogeneity $Inh(E)$ as first trial function. In Fig. 4.10 the fits using P(E)-theory can be seen. The fits cover the whole data set, including the peak, the shoulder and the tails.

By fitting, the mean values are $T_{mean} = 305 \pm 140$ mk, $R_{mean} = 871 \pm 280 \Omega$. The capacitances and inductances have the average values of $C_{mean} = 10.55 \pm 4$ fF and $L_{mean} = 10.56 \pm 3$ mH respectively. Additionally, the average charge energy ($E_C = 2e^2/C = 10.29 \pm 3 \mu eV$), which is higher than the thermal energy and Josephson coupling, making it necessary to be considered in the circuit. The mean values of ω_c and ω_s are: $\omega_{c,mean} = 121 \pm 6$ GHz and $\omega_{s,mean} = 99 \pm 4$ GHz.

4.4 Conclusion and summary

In this chapter the Josephson supercurrent and the resonances in the $I - V$ curve on Al/I/Al junction have been analyzed. The elements of the circuit (capacitance, resistance and inductance), and the Josephson temperature which is related to the circuit and electronic noises have been derived. In Table. 4.1 a summary of the values derived from various models can be seen. The noise (Josephson) temperature for all the various models are consistent and in the same range of ~ 350 mK. This temperature is related to the electronic temperature when electron pairs (Cooper pairs) tunnel through

the barrier, and it can be reduced by adding more filters to the circuit to get closer to the base temperature. The resistance (Z_{env}) for the first three models are in the same range $\sim 550 \Omega$. From these comparisons we can conclude that the assumption for phase diffusion model is valid, since it is a special case of RCSJ model in the limiting case where $E_J < k_B T$ which holds true for our conditions. In the quantum fluctuations model, the resistance is higher than the previous cases. This can be explained because this model considers the environmental impedances with all the frequencies, unlike the previous models where just the impedance at zero frequency was considered. The resonance frequency which produces the shoulder in the $I - V$ curve, has been derived from two models (3,4). The values are close to each other ~ 90 GHz. This value depends on the electronic circuit, length and the material of the tip. By changing the tip the resonance frequency can be affected. The capacitance and the inductance of the circuit can be derived only from the final model. The capacitance is on the order of 10 fF which makes the capacitance energy significant. In summary all the models are to high extent consistent with each other. In chapter 8 Josephson STM on BiPd will be discussed.

TABLE 4.1: Comparison between the fitted values from different models. (PD: phase diffusion)

Models	$T_n(mK)$	$T_J(mK)$	$Z_{env}(\Omega)$	$\omega(GHz)$	$C(fF)$	$L(mH)$
1- RCSJ	383 ± 41	n.A	487 ± 40	n.A	n.A	n.A
2- PD	374 ± 40	336 ± 150	598 ± 48	n.A	n.A	n.A
3- PD+Lorentzian	391 ± 165	341 ± 150	596 ± 167	85 ± 1.5	n.A	n.A
4- P(E) theory	305 ± 142	n.A	872 ± 281	99 ± 4.8	10.55 ± 4	10.56 ± 3

Chapter 5

Visualizing the magnetic structure in Fe_{1+y}Te

In order to understand the competition between superconductivity and magnetic order in iron based superconductors, the non-superconducting parent compound of the iron chalcogenides, Fe_{1+y}Te , has been studied with spectroscopic imaging STM. Fe_{1+y}Te has a magnetostructural phase transition at $\sim 60\text{-}70$ K, below which it shows a bicollinear antiferromagnetic order. In this study, I show the low temperature atomic scale imaging of the magnetic structure of $\text{Fe}_{1.07}\text{Te}$ and $\text{Fe}_{1.15}\text{Te}$ in real space obtained by STM. The magnetic structure images reveal that magnetic order in the monoclinic phase ($\text{Fe}_{1.07}\text{Te}$) has a unidirectional stripe order, whereas in the orthorhombic phase at higher excess iron concentration ($\text{Fe}_{1.15}\text{Te}$), a transition to a phase with coexistence of magnetic order in both directions, locally similar to a plaquette order, is observed.

5.1 Iron-chalcogenides

Fe_{1+y}Te is the non-superconducting parent compound of the iron chalcogenide superconductors [74], where the phase diagram is shown in Fig. 5.1a. By doping the compound with about 25% selenium, superconductivity emerges. A peculiarity of the case of Fe_{1+y}Te compared to the non-superconducting parent compounds of the iron-pnictide superconductors is that the magnetic order does not occur at the dominant nesting vector of the Fermi surface sheets of the superconducting compound, in the Fe-Fe bond direction, but rather at 45° , as is shown in Fig. 5.1 c and d. The complex magnetic structure of Fe_{1+y}Te was determined by neutron scattering already long before the discovery of superconductivity in iron-based materials [76]. At temperature of around 60K, it shows a magneto-structural phase transition, with the structure changing from

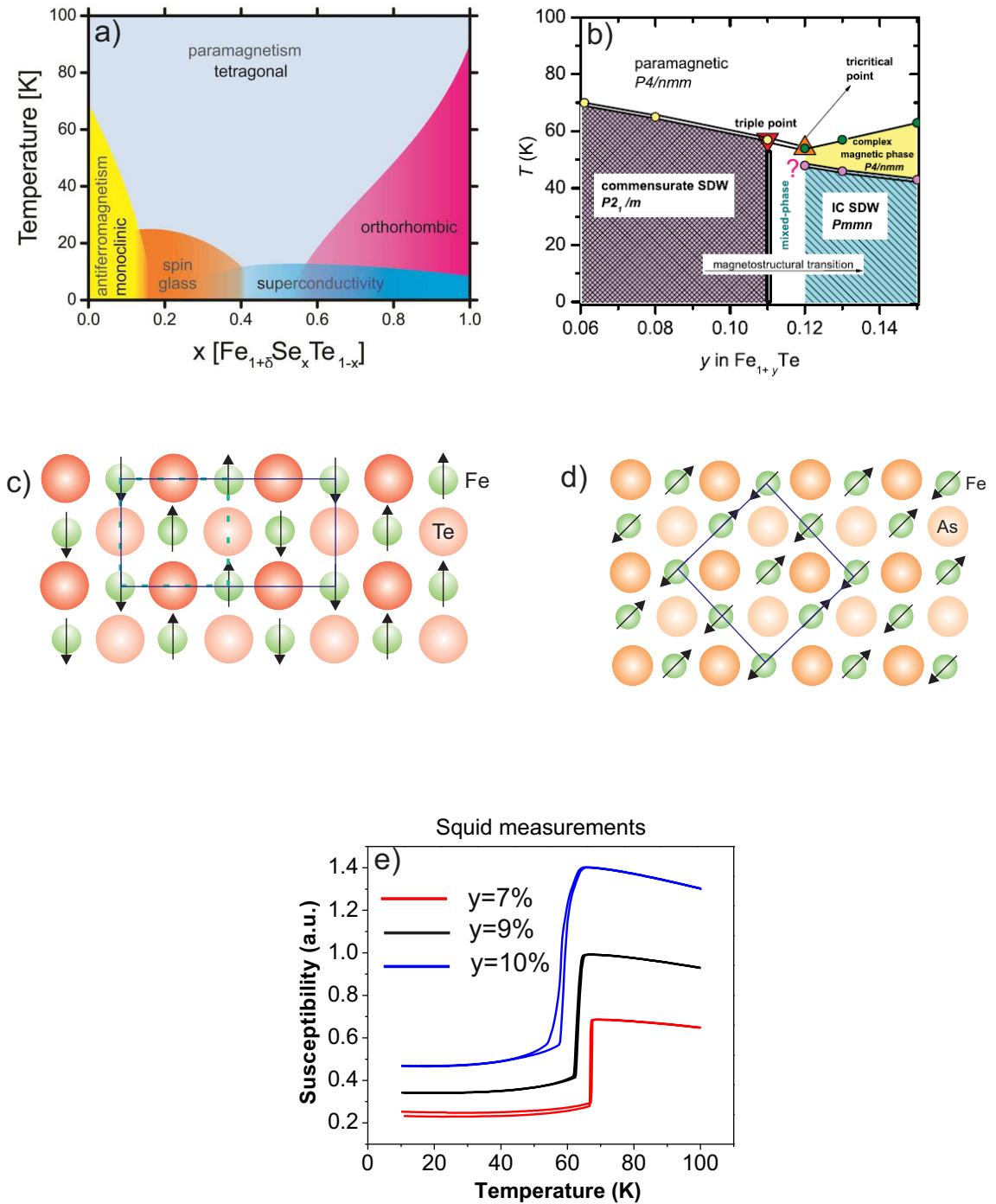


FIGURE 5.1: (a) Phase diagram of $FeSe_xTe_{1-x}$ as a function of selenium content x . At the extremes of the phase diagram $x=0$ and $x=1$, the material exhibits a monoclinic and orthorhombic distortion of the crystal lattice, respectively, while at $x=0.5$ it is tetragonal. Only for pure FeTe magnetic ordering is observed. Reproduced from [74]. (b) The phase diagram of $Fe_{1+y}Te$ as a function of temperature and excess iron composition [75]. (c) Schematic illustration of the atomic unit cell (in dashed lines) and magnetic unit cell (in solid lines) of FeTe. (d) Magnetic unit cell of the parent compound of other families of iron-based superconductors (such as 122 or 1111 families). There is a 45° shift in the spin of iron atoms. Red, green and orange spheres represent Te, Fe and As atoms respectively. (e) SQUID measurement on our samples (excess iron ranging between 7 to 10%).

tetragonal to monoclinic. With increasing concentration of excess iron, the transition temperature is suppressed (Fig. 5.1b) [77, 78]. The magnetic order and phase transition of Fe_{1+y}Te have been studied by neutron scattering experiments [79, 80] which shows that at small excess iron concentrations $y < 0.11$ and at low temperatures the magnetic moments order with a commensurate wave vector. The magnetic order can be described by different models: bicollinear spin order at $Q_{\text{SDW}} = (1/2, 0, 1/2)$ [79, 81, 82] and spin plaquettes of four nearest neighbor iron atoms [83, 84] (in the following, wave vectors are refer to the reciprocal lattice of iron atoms). At higher excess iron concentration, the magnetic order becomes incommensurate and an additional magnetic phase emerges at the transition from tetragonal to orthorhombic structure [78].

According to density functional theory (DFT) calculations [85], the Fermi surface in Fe_{1+y}Te does not exhibit electron or hole pockets at $(\pm 1, \pm 1)$ (reciprocal lattice of iron atom). Therefore, it is unlikely that the driving force towards magnetic order is nesting like in many of the iron-pnictide compounds. A number of scenarios based on local moment approaches have been proposed for the origin of magnetism in Fe_{1+y}Te , dominated by interactions between Fe $3d$ electrons up to the third nearest neighbor [82, 84, 86, 87]. Curie-Weiss like behavior of the susceptibility [86] and the large magnetic moment per iron atom ($2.7\mu_{\text{B}}$) favor this picture [88]. There are however also approaches which describe the magnetic order from an itinerant picture [89] or where both, itinerant and localized states are important [83].

5.2 Results

In this chapter I present an investigation of the electronic properties of Fe_{1+y}Te by our home-made STM/STS, in order to obtain a microscopic picture. Our data reveal a unidirectional modulation both in STM images and in spectroscopy, which has the same wave vector as the spin density wave (SDW) order. I discuss the relation of this unidirectional modulation with the magneto-structural phase transition in Fe_{1+y}Te . Experiments were performed in two home-built low temperature STMs, one already discussed in this thesis operating at temperatures down to 10mK [17] and another STM with a base temperature of 1.8K also in cryogenic vacuum, operated with the assistance of Dr. Singh and MSc. Aluru. Samples are prepared by *in-situ* cleaving, and PtIr wire used as STM tip. Bias voltages are applied to the sample, with the tip at virtual ground. Differential conductance spectra have been recorded through a lock-in amplifier. Single crystals of Fe_{1+y}Te were grown by the Bridgman from high purity (4N) materials [90]. We have studied four samples with different excess iron concentrations of $y = 7.6 - 15\%$ as determined by Energy-dispersive X-ray spectroscopy analysis. Superconducting quantum interference

device (SQUID) characterization of the magnetization of the samples shows that for our samples the magnetostructural phase transition is between 60 and 67K (Fig. 5.1e). The behavior of the magnetic phase transition as function of excess iron is consistent with the previously published phase diagram [78].

5.2.1 Unidirectional modulation from topography of $Fe_{1.07}Te$

$Fe_{1+y}Te$ has a layered crystal structure (Fig. 5.2a) where the iron chalcogenide layers are only weakly bound by van-der-Waals interactions. The most likely cleavage plane in $Fe_{1+y}Te$ is in the (001) plane between the tellurium layers.

The superposition of a sketch of the magnetic structure with a topographic image is shown in Fig. 5.3b. According to DFT calculations done by Dr. Yaresko, the electronic states at the Te sites are strongly spin-polarized in the vicinity of the Fermi level, with the direction of the magnetization being in plane and in opposite direction to the spin of the three equal-spin iron neighbors.

A topographic image of the sample surface with atomic resolution is shown in Fig. 5.2c, in which the square lattice represents the top layer tellurium atoms. Excess iron atoms at the surface show up as bright protrusions [91, 92]. The excess iron atoms reside in hollow sites between tellurium atoms, where recently isosceles triangular electronic structure around the excess iron atoms have been observed [93]. The Fourier transform of the topography (Fig. 5.2d) clearly shows the peaks associated with the tellurium lattice at the surface. The two non-equivalent spots associated with the tellurium lattice at $\mathbf{q}_{Te}^a = (\pm 1, 0)$ and $\mathbf{q}_{Te}^b = (0, \pm 1)$ have noticeably different intensities. A topographic image in the same position as Fig. 5.2c obtained with a different tip after picking up excess iron, is shown in Fig. 5.2e. It shows clear stripe-like patterns superimposed to the tellurium lattice. The Fourier transform of the topography reveals an additional pair of peaks with half the wave vector compared to the atomic peaks (Fig. 5.2f). The unidirectional modulation has two major components in the Fourier transform: the first is a pair of distinct peaks at wave vectors $\mathbf{q}_{AFM} = (\pm 1/2, 0)$, the second, which is also seen with a normal tip, at $\mathbf{q}_{CDW} = (\pm 1, 0)$ coincides with the atomic peak of the tellurium lattice – and is still clearly noticeable by the intensity difference compared to the other peak related to the Te lattice ($\mathbf{q}_{Te}^b = (0, \pm 1)$).

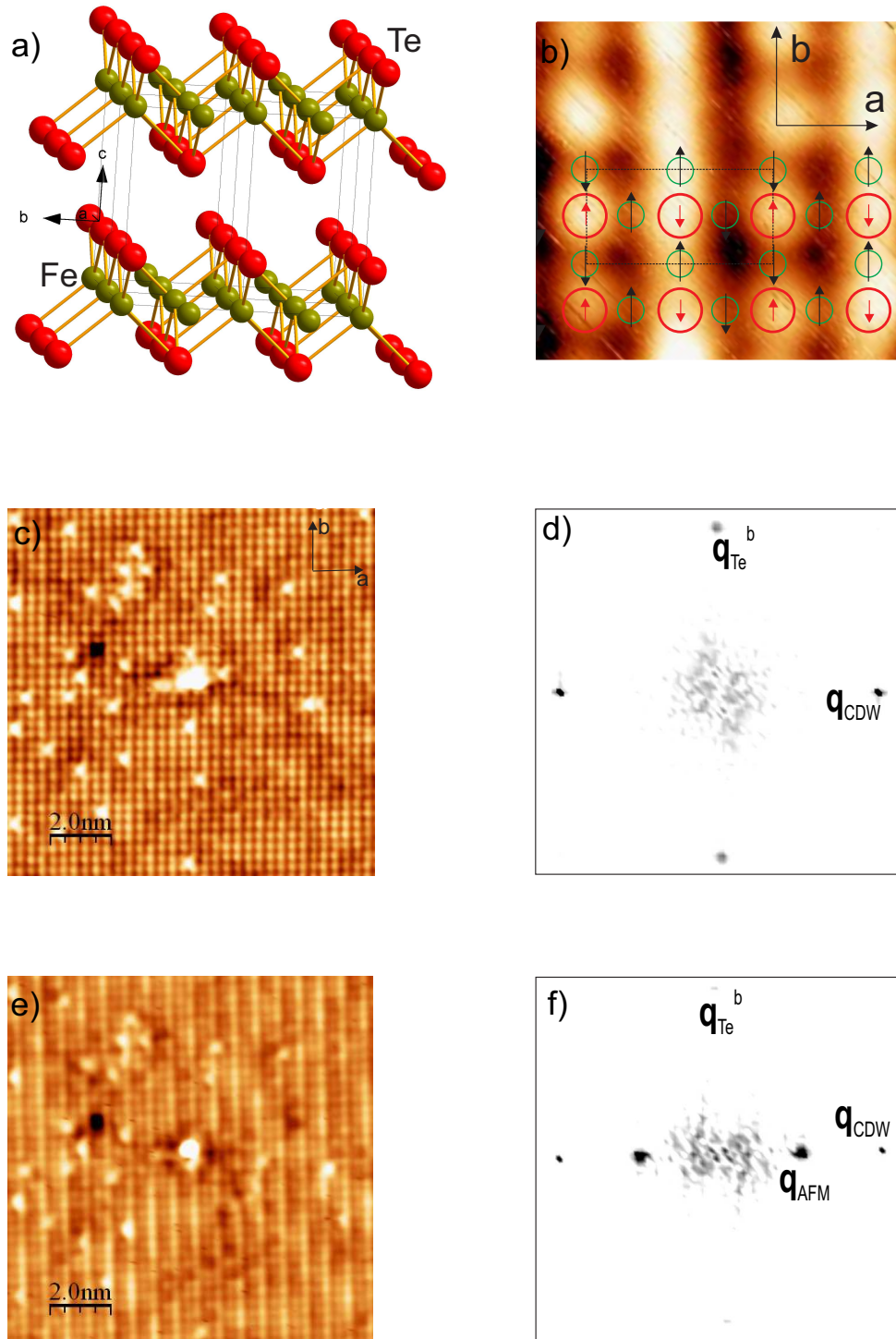


FIGURE 5.2: (a) Illustration of the crystal structure of Fe_{1+y}Te . (b) Ball model of the top-most tellurium and iron atoms with the spin structure determined from neutron scattering overlaid on a topographic image. Arrows on Te atoms indicate polarization as obtained from calculations, on iron atoms the local magnetic moment (because the direction of the magnetization of the tip is unknown, a magnetic structure with all spins reversed could yield the same contrast). Image taken at $T = 30$ mK, $V_b = 50$ mV, $I_t = 500$ pA). (c) Topography of a Fe_{1+y}Te sample, acquired with a tip which shows no magnetic contrast, excess iron atoms show up as protrusions ($V_b = 60$ mV, $I_t = 200$ pA, $T = 3.8$ K). (d) Fourier transform of (c) is displayed, showing the peaks associated with the Te lattice at $\mathbf{q}_{\text{Te}}^a = (\pm 1, 0)$ and $\mathbf{q}_{\text{Te}}^b = (0, \pm 1)$. One pair of peaks, marked \mathbf{q}_{CDW} ($= \mathbf{q}_{\text{Te}}^a$) shows up with stronger intensity than the other. (e) Topography acquired in the same place as (c) with a tip which shows magnetic contrast ($V_b = 60$ mV, $I_t = 200$ pA, $T = 3.8$ K). (f) The Fourier transform of (e), showing beside the peaks due to the Te lattice, additional ones associated with magnetic order at $\mathbf{q}_{\text{AFM}} = (\pm 1/2, 0)$.

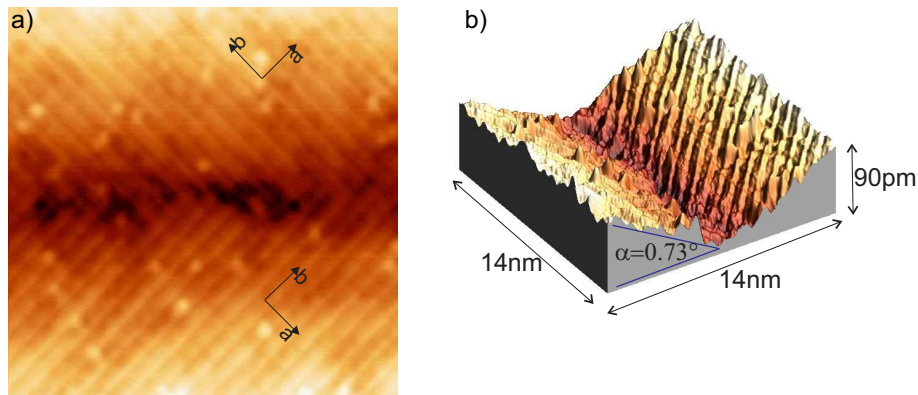


FIGURE 5.3: Symmetry breaking in Fe_{1+y}Te in topographic images. (a) Topographic image of a twin boundary ($14 \times 14 \text{nm}^2$, $V_b = 150 \text{mV}$, $I_t = 0.03 \text{nA}$). Stripes on the two planes are perpendicular with respect to each other. (b) 3D rendering of the topography in (a) to better visualize the angle between the two domains.

5.2.2 Twin boundaries

Twin boundaries are highly symmetrical interface, often one of the crystals being the mirror image of the other; also, atoms are shared by the two crystals at regular intervals. This has a much lower-energy interface than the grain boundaries that form when crystals of arbitrary orientation grow together.

When cooling the sample from room temperature down to 4K at the cleaver stage and due to the defects existing in the sample, the monoclinic distortion will not be uniform across the crystal, and as a consequence multiple domains occur. A boundary between two different domains of the monoclinic distortion is shown in Fig. 5.3a. The tilt angle between the two surfaces is 1.46° (Fig. 5.3b). If the crystallographic c-axis is the same on both sides of the twin boundary, this would yield $\beta = 89.27^\circ$, fairly close to the value obtained by X-ray diffraction ($\beta = 89.21^\circ$ [79]). The direction of the stripes changes at the domain boundary. The modulation is found consistently over large surface areas and is never found to switch direction or phase within a domain of the monoclinic distortion in samples with low excess iron ($y < 0.12$) — but at a domain boundary the stripes always switch direction as shown in Fig. 5.3a. The locking between the modulation at q_{AFM} and the structural distortion suggests that it is related to the magnetostructural phase transition.

5.2.3 Bias dependence

The appearance of the modulation in topographic images of FeTe has a bias dependence. The contrast of the modulation which we observe reverses around 0mV (compare

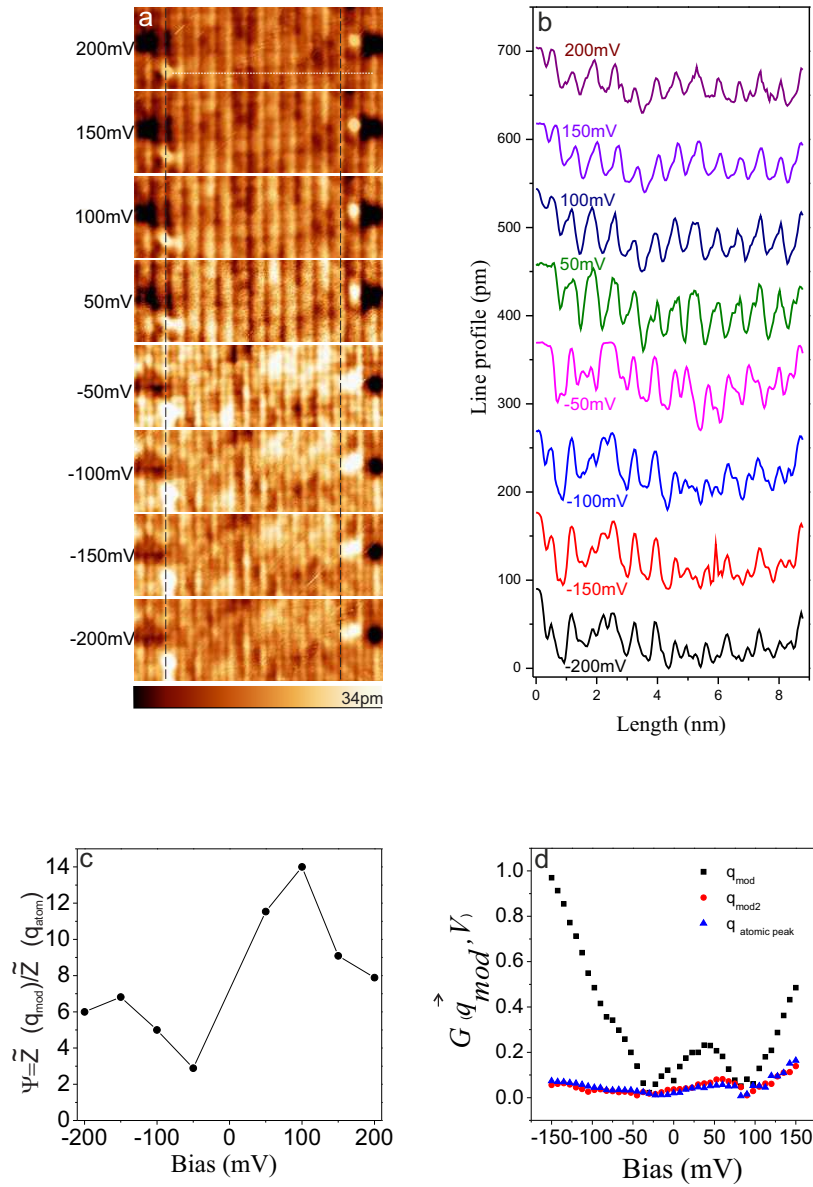


FIGURE 5.4: (a) Topographic images as a function of bias voltage $V_b = -200$ — $+200$ mV, taken in the same place (as can be seen from the defects). A contrast reversal can be seen across 0V. The length is 10 nm. (b) Height profile of white dashed line in (a) for different biases. (c) Intensity of the modulation as a function of bias taken from the FFT of topography. (d) Intensity of the Fourier components of the modulation q_{AFM} , q_{CDW} and q_{Te^b} taken from spectroscopic map. The data are tip dependent.

Fig. 5.4a). The amplitude of the modulation is strongest at bias voltages in the range between 0mV and 100mV (compare Fig. 5.4c). The contrast reversal can also be traced in spatial maps of the differential conductance (Fig. 5.4b and d). However, the values derived from spectroscopic maps as well as the intensity of the modulation were strongly tip dependent. This rules out the idea that the stripe (modulation) originates from a charge density wave, otherwise the energy dependence in the spectroscopic maps were consistent and would have all shown similar energy values.

5.2.4 Temperature dependence

While the data at low temperature shows the same periodicity of the magnetic order as found in neutron scattering, in order to establish its relation to the magneto-structural phase transition observed in the bulk, we studied its temperature dependence. On increasing the temperature, the stripe modulation disappeared around a temperature T of 45 K and was not observed at $T > 50$ K. A topographic image taken at $T = 54$ K is displayed in Fig. 5.5a. The Fourier transform (inset in Fig. 5.5a) shows only the peaks associated with the Te lattice. To quantify the intensity of the modulation, I used the ratio $\Psi_{\text{AFM}} = \tilde{z}(\mathbf{q}_{\text{AFM}})/\tilde{z}(\mathbf{q}_{\text{Te}}^b)$ of the amplitude of the Fourier component at the wave vector of the magnetic order $\tilde{z}(\mathbf{q}_{\text{AFM}})$ with the amplitude of the (weaker) atomic peak $\tilde{z}(\mathbf{q}_{\text{Te}}^b)$. Fig. 5.5b shows the temperature dependence of Ψ_{AFM} . The trend is consistent with a mean-field behavior (Eq. 5.1 [94]) with a critical temperature $T_c = 45$ K (solid line in Fig. 5.5b).

$$\Psi(T) = \Psi_0 \tanh\left(\frac{\pi}{2} \sqrt{\frac{T_c}{T} - 1}\right) \quad (5.1)$$

In Fig. 5.5c, I plot Ψ_{CDW} as a measure for the intensity of the peak at $\mathbf{q}_{\text{CDW}} = \mathbf{q}_{\text{Te}}^a$ as a function of temperature. The asymmetry of the intensity of the atomic peaks shows the same temperature dependence as the intensity of the peak at \mathbf{q}_{AFM} , therefore it is really the magnetic order of the sample which is suppressed. The transition temperature in the bulk (60 – 70 K) is somewhat larger. A possible reason for this is that the surface iron-tellurium layer has only one neighboring layer as opposed to two in the bulk.

5.2.5 Spatial dependence on spectra

Previous angle resolved photoemission spectroscopy (ARPES) [95] studies and DFT calculations with bicollinear antiferromagnetic (AFM) spin order [96] have not identified a true SDW gap. Spectra taken along a line normal to the stripes reveal small position dependant changes (Fig. 5.6b). Tunneling spectroscopy shows a gap like feature close to the Fermi energy (compare Fig. 5.6a). However no fully developed gap is observed.

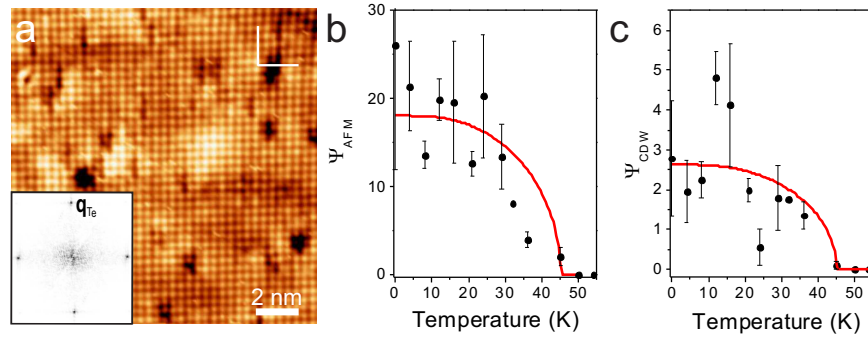


FIGURE 5.5: (a) topography recorded at 50 K. Inset shows the Fourier transform of the topography. The unidirectional modulation is not detected at this temperature ($V_b = 100$ mV, $I_t = 800$ pA). (b) Intensity of the modulation Ψ_{AFM} as a function of temperature, solid red line is what would be expected in a mean field theory. (c) $\Psi_{\text{CDW}} = (\tilde{z}(\mathbf{q}_{\text{CDW}}) - \tilde{z}(\mathbf{q}_{\text{Te}}^b)) / \tilde{z}(\mathbf{q}_{\text{Te}}^b)$ at the wave vector of the charge density wave \mathbf{q}_{CDW} as a function of temperature. The fit in c has been done by fixing T_c to the same value as in b.

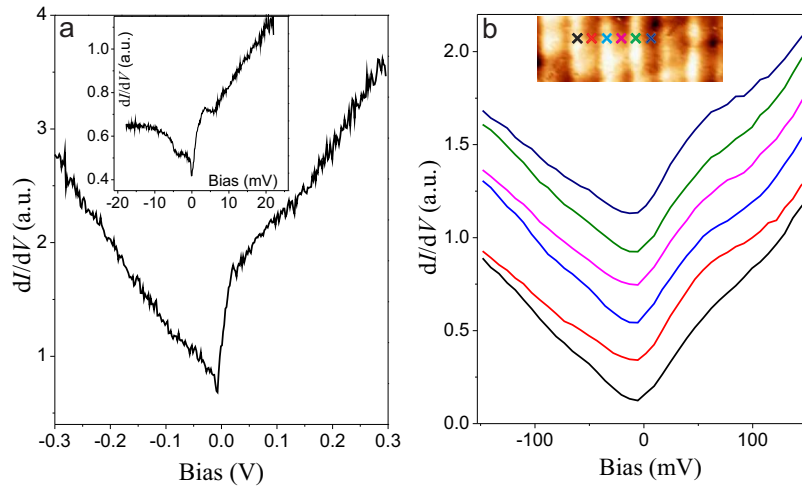


FIGURE 5.6: Spectroscopy of the stripe structure. (a) Conductance tunneling spectrum, with large energy range. In the inset the small energy range spectrum a gap-like feature can be seen. (b) Evolution of the spectra as a function of spatial position. Crosses in the Inset show the positions where the spectra were taken. For clarity, spectra are offset vertically ($V_b = 150$ mV, $I_t = 100$ pA).

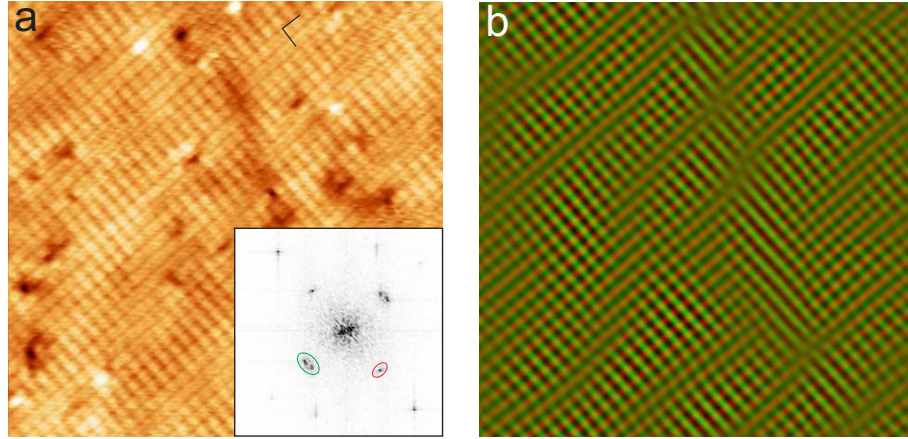


FIGURE 5.7: **Topography at higher excess iron concentration** ($y > 0.12$). **(A)** topography obtained from a sample with high excess iron concentration ($y = 0.15$), showing stripe modulation in two directions superimposed ($V_b = 100$ mV, $I_t = 100$ pA, $T = 1.8$ K). A large part of excess iron has been picked up by the tip, leaving an almost clean Te-terminated surface. Inset: Fourier transform of the topography showing peaks associated with magnetic contrast around $(\pm 1/2, 0)$ and $(0, \pm 1/2)$. **(B)** Filtered image showing the components associated with magnetic contrast in different colours to visualize the bidirectional stripe order.

5.2.6 Topography of $\text{Fe}_{1.15}\text{Te}$

The magnetic order in Fe_{1+y}Te becomes more complex with increased excess iron content y [80, 97]. Figure 5.7a shows a topographic image obtained on a sample with higher excess iron concentration (at $y = 0.15$). In contrast to measurements taken on samples with lower excess Fe concentration, the topography reveals stripe-like patterns in both directions, i.e. at $(\pm 1/2, 0)$ and $(0, \pm 1/2)$ in Fourier space (insert of Fig. 5.7a), coexisting in the same domain of the orthorhombic distortion. The image reveals nanoscale domains of predominantly unidirectional stripes coexisting with regions of bidirectional patterns. These two-dimensional patterns could be due to a superposition between the two unidirectional modulations or due to a transition towards a plaquette order, which has been theoretically predicted to become more important due to quantum fluctuations as the sample becomes orthorhombic [84]. As can be seen from the real space picture, the structure is still locally commensurate with the lattice, however, there are phase slips between different nanoscale domains. This can be more clearly seen from a Fourier-filtered image where only the Fourier components associated with the modulation contrast are shown (Figure 5.7b).

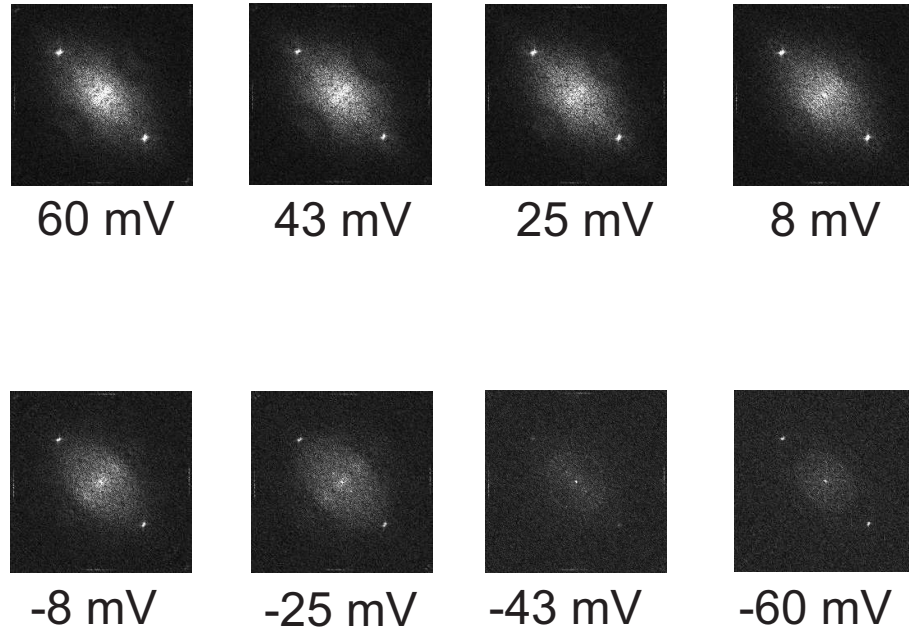


FIGURE 5.8: FFT of map from -60mV to 60 mV.

5.2.7 Quasi particle interference (QPI)

In Fig. 5.8, the symmetrized fourier transform of the conductance map from -60 mV to 60 mV can be seen. The bright points indicate q_{AFM} . The intensity of q_{AFM} has already been shown in Fig. 5.4d. As it can be seen there is a dispersion in the direction perpendicular to q_{AFM} .

5.2.8 Spectroscopy on excess Fe defects

By comparing the average spectra between the clean areas and places with excess iron or defect, a clear difference can be seen as shown in Fig. 5.9a. The excess irons have a higher DOS at the occupied states (negative energies), and thus in the map will look as bright points. On the other hand, the defects have a lower DOS than the clean area at the unoccupied states (positive energies), and therefore in the map will look as darker regions. This is consistent with the STM results published previously in this compound [92].

In STM topographies the distribution of excess iron atoms appears inhomogeneous on length scales on the order of ten nanometers (see Fig. 5.9b and c), which in the monoclinic phase has only negligible influence on the reported modulation. These areas are the regions where the excess irons deposit on the tip.

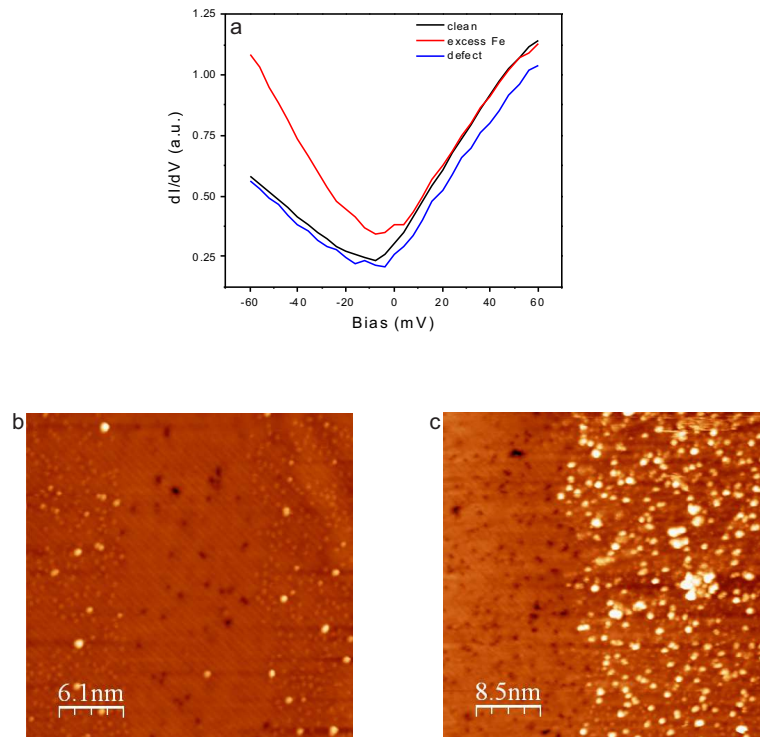


FIGURE 5.9: **Topography showing excess iron inhomogeneities, accompanied with the stripes.** (a) Comparison of the conductance spectra on different positions: excess iron, clean area and defects from -60mV to 60 mV. (b) Topography of Fe_{1+y}Te with less excess iron ($y = 7\%$) at 10mK ($V_b = 200\text{mV}$, $I_t = 100\text{pA}$). (c) Topography of Fe_{1+y}Te with high excess iron ($y = 15\%$) taken at 1.8K. ($V_b = 90\text{mV}$, $I_t = 300\text{pA}$)

5.2.9 Magnetic field dependence

In order to verify that the stripe modulation originates from spin-polarized tunneling, we demonstrated the performed measurements in magnetic field. Fig. 5.10a and b show topographic images taken at the same location on the surface in magnetic fields of $B = +5\text{T}$ and -5T , respectively. The stripes shift by half the wave length of the antiferromagnetic order on reversing the direction of the magnetic field. This can be clearly seen in the line profiles in Fig. 5.10c which have been obtained from Fig. 5.10a and b along the stripes of the modulation, resulting in a profile of the modulation along a. The magnetic field dependence of the imaging contrast demonstrates that the stripe modulation is due to spin-polarized tunneling. Because the sample has only a small net magnetization, the magnetic field switches the magnetization of the tip only. The strongest spin polarization is observed in between the tellurium atoms.

The appearance of excess iron atoms shows a strong dependence on the spin-polarization of the tip, as can be seen from the dashed square in Fig. 5.10a and b. The topographic height of the excess iron atoms is directly correlated with the apparent height of the

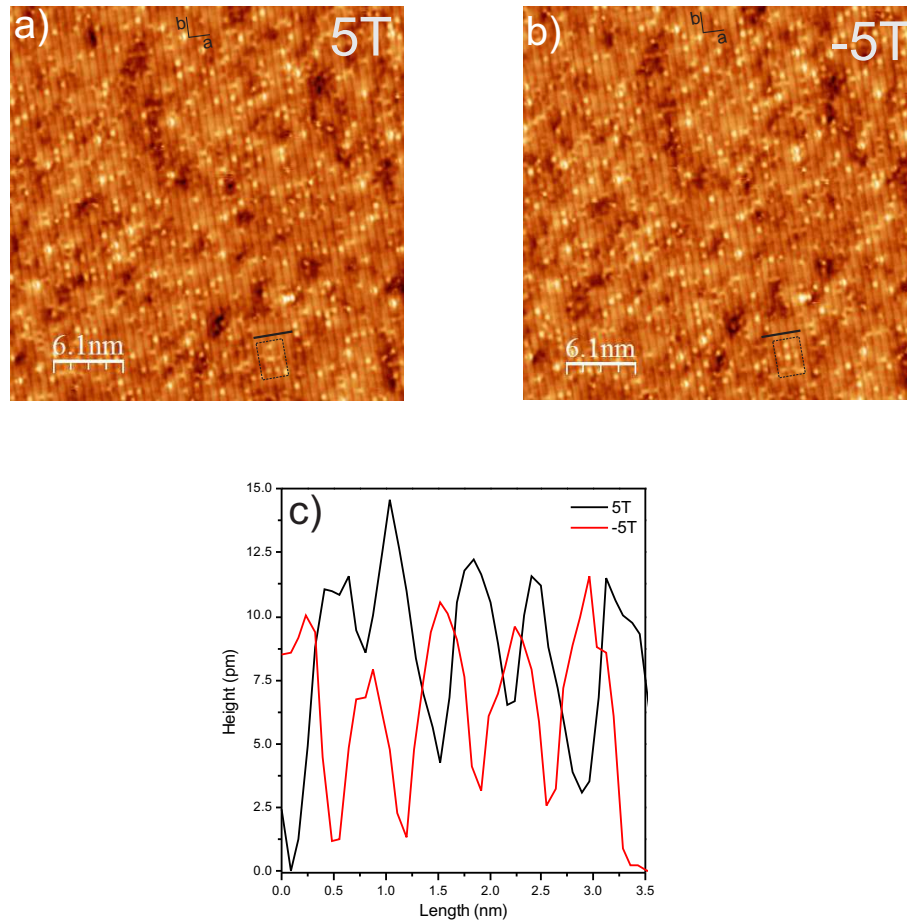


FIGURE 5.10: (a) Topography measured at 3.8K at a magnetic field of 5T normal to the surface, (b) Topography taken in the same place in a magnetic field of $-5T$ ($V_b = 80mV$, $I_t = 100pA$). Images obtained at zero field before the topography in a was measured showing the same contrast as the one shown in panel a. The dashed squares in (a) and (b) show the change in the contrast of the excess iron by reversing the applied field. (c) Line profile normal to the modulation (in the solid line in a and b) showing the change in the modulation with magnetic field.

trough (or crest) between two rows of Tellurium atoms, both switching their apparent height with field.

5.2.10 Conclusion and summary

The topographies indicate that the stripes appear at the wave vector of the spin density wave, and were quite stable and were visible for the majority of the topographies, and seldom were we able to retrieve the atomic resolution topographies without the modulation. Since X-ray diffraction experiments at 20K [98] did not show the same modulation, it can be concluded that it is more likely an electronic (charge) or magnetic (spin) effect than a real structural distortion of the lattice. The possible explanations which can describe the modulation are either surface reconstruction, charge modulation or spin polarized measurements. Here I discuss the most favorable explanation.

At the surfaces of some of the iron pnictides ($\text{Ca}(\text{Fe}_{1-x}\text{Co}_x)_2\text{As}_2$, $\text{Sr}_{1-x}\text{K}_x\text{Fe}_2\text{As}_2$), strong unidirectional modulations have been observed in STM which have been attributed to a surface reconstruction with the same periodicity as the one we observe in Fe_{1+y}Te . There are a number of major differences to the case of Fe_{1+y}Te , which make an interpretation of the unidirectional modulation in terms of a surface reconstruction rather unlikely: (1) The surface reconstruction observed on $\text{Sr}_{1-x}\text{K}_x\text{Fe}_2\text{As}_2$ (or Co-doped BaFe_2As_2) is usually connected to a Strontium (Barium) layer at the surface which reconstructs [99, 100]; in $\text{Fe}_{1+y}\text{Se}_x\text{Te}_{1-x}$ there is no such overlayer and no reconstruction has been reported [101]. (2) The direction of the modulation observed on the 122-materials due to the surface reconstruction is not constrained by the underlying crystal structure. Changes in the direction of the modulation are found within a single domain - unlike our case [102, 103]. (3) the surface reconstruction on $\text{Sr}_{1-x}\text{K}_x\text{Fe}_2\text{As}_2$ can be observed at temperatures up to 200K, above the temperature of the structural phase transition [102].

The next possibility is the charge modulation or a charge density wave. However, according to theoretical predictions, a charge density wave (CDW) is induced by antiferromagnetic or spin density wave (SDW) order in iron-based superconductors [104], such that the wave vector of the CDW is twice the wave vector of the magnetic order (i.e. $\mathbf{q}_{\text{CDW}} = 2\mathbf{q}_{\text{AFM}}$), which rules out this conjecture. Furthermore, supplementary techniques such as X-ray or neutron scattering are able to determine the CDW with different modulations, which however has never been reported. Additionally, if the assumption of CDW would be correct, then we would expect to see a CDW gap opening on the conductance spectra. Our data show no evident gap emerging on the spectra and by further analysis of the spectra I found that the spectra are strongly tip dependent and not a property of the sample, since from various spectroscopic maps different values were obtained, which suggests that the origin of the modulation emerges from the tip. Temperature dependence measurements of the intensity of the modulation further related

the origin of the stripes to the magnetostructural phase transition as the modulation vanishes at a temperature close to the SDW phase transition.

The most convincing possibility for explaining the origin of the stripe is that we have a magnetic tip. We have various evidences which strongly supports this claim : (1) Initially after putting the sample in the STM at low temperatures, the stripes were never visible and only after crashing the tip on the surface or by applying high currents between the tip and the sample were we able to observe the modulation. This is a very important fact which supports the hypothesis that a cluster of excess iron atoms on the surface deposit on the tip and result a spin polarized tip, due to the ferromagnetic behavior of iron. Spin polarized scanning tunneling microscopy measurements have been previously carried out with magnetic tips on thin films, nanostructures and magnetic clusters [105]. The Fe cluster on the tip is really stable and does not tend to detach, since the metallic bond in the tip between Pt – Ir and Fe is stronger than van-der-Waals bond between $Fe_{1+y}Te$ and Fe. (2) The strongest proof for the claim of spin polarized measurement are the field dependent topographies. The contrast reversal of the topographies by reversing the direction of the applied field indicates that we are detecting spin. Applying a magnetic field should in principle have no effect on the charge and thus this rules out the assumption of a charge modulation. Applying a magnetic field in inverse directions would change the spin polarity of the tip, resulting in contrast reversal due to magnetic structure of the sample.

The picture which emerges from our measurements is that at low excess iron concentrations, the magnetic order is commensurate and locked with the monoclinic distortion of the lattice. In Heisenberg models incorporating up to the third nearest neighbour, this has been rationalized by anisotropic coupling between nearest and next-nearest neighbour iron spins [87] or by the influence of orbital ordering on the magnetic couplings [82]. Our observation of a unidirectional stripe-like magnetic order in the monoclinic phase shows that the monoclinic distortion suppresses bidirectional or plaquette magnetic order at low excess iron concentrations, strongly favouring unidirectional stripe order. As the lattice constants in the a - and b -direction approach each other with increasing excess Fe concentration [75, 80], we observe both directions of the magnetic order near $(1/2, 0)$ and $(0, 1/2)$ coexisting in the same domain of the sample with patches reminiscent of plaquette order. Further, the magnetic order becomes incommensurate. Incommensurate magnetic order has also been detected in neutron scattering at high excess iron concentrations, showing a shortening of the wave vector associated with the magnetic order [80, 97]. In our case the peak associated with the magnetic order spreads away from the high symmetry direction. As the material still has an orthorhombic distortion, the two directions will not have the same energetics. This raises interesting questions as to how the magnetic order sets in as a function of temperature. Neutron scattering has

shown that there is an additional magnetically ordered phase at higher temperatures in samples with high excess iron concentration [78, 97].

In summary, we have carried out spin-polarized low temperature STM experiments on $Fe_{1+y}Te$ crystals with iron concentrations from 7% to 15% to characterize the atomic scale spin structure by spin-polarized tunneling. We found a commensurate unidirectional stripe modulation at low excess iron concentration, with a transition to coexistence of the two almost equivalent directions of the stripe order and patches reminiscent of plaquette order at larger excess iron concentrations.

Chapter 6

Observation of vortices on CeCu_2Si_2

“Understanding the origin of superconductivity in highly correlated electron systems continues to be at the forefront of the unsolved problems of physics” [106]. CeCu_2Si_2 is the first heavy Fermion superconductor that has been discovered, therefore many researches and measurements have been carried out on CeCu_2Si_2 . However, the mechanism and the symmetry of the order parameter are still under debate. In this chapter I present the first scanning tunneling microscopy study on this material with our home-built dilution refrigerator STM. By in-situ cleaving, a flat crystal surface and stripe like structure was observed. By measuring conductance spectroscopy, the evolution of the gap as a function of temperature and magnetic field was probed. Furthermore, the magnetic vortices were mapped and their dependence on the magnetic field was investigated. Our findings could provide insight on the symmetry of the order parameter and elucidate the interaction between magnetic excitation and superconductivity in heavy-fermion superconductors.

6.1 Introduction to Heavy-Fermion compounds

When a magnetic impurity is embedded in a metal, at low temperatures the spin of conduction electrons tend to screen the local magnetic moment, causing the spins to align antiparallel with respect to each other. These electron clouds surrounding the impurity ion act as scattering centers, which results in the increase of resistance of metals below a certain temperature (known as Kondo temperature T_K , e.g. Cu doped with Fe [107]). This phenomenon referred as Kondo effect is illustrated in Fig. 6.1a. The impurities give rise to a narrow, localized state electron band in the DOS as a consequence of the

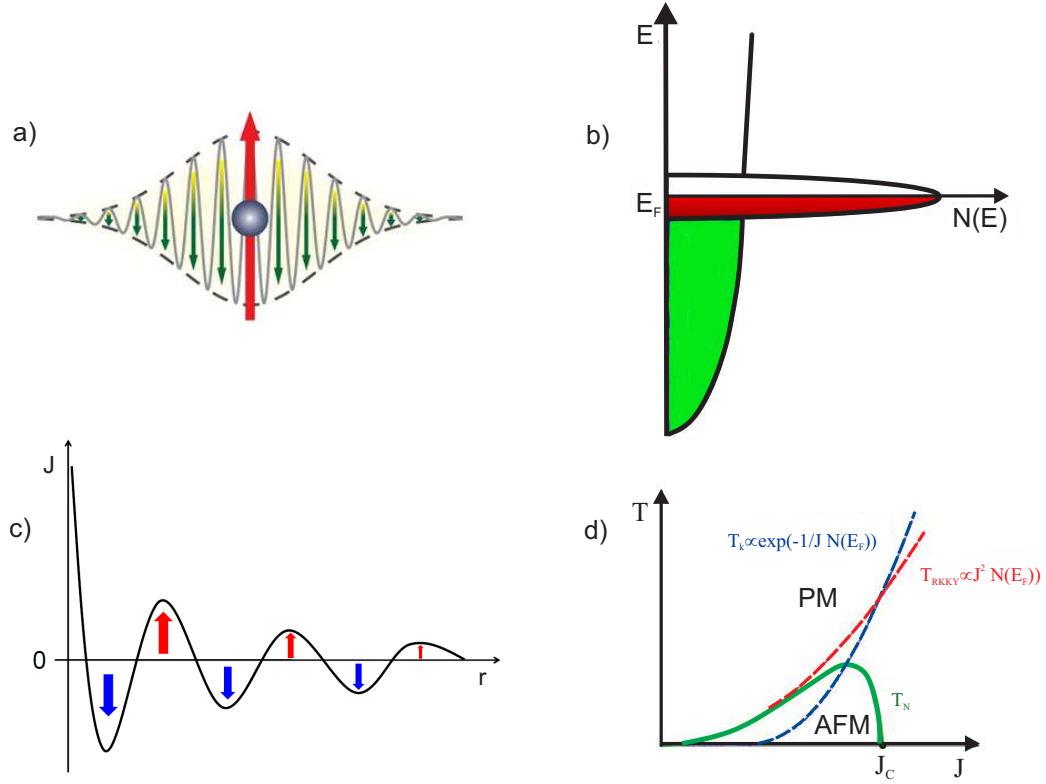


FIGURE 6.1: (a) A schematic representation of the screening an isolated localized magnetic impurity (red) by the delocalized conduction electrons of the metal host (green) caused by the Kondo effect, reproduced from [109]. (b) Scheme of the density of states $N(E)$ of a metal with magnetic impurities at low temperatures. The narrow peak comes from the hybridization of the localized electrons in the inner shells of the magnetic impurities with the conduction ones (red), which is superimposed to the density of states of the conduction electrons of the metal host (green). (c) Schematic of the magnetic coupling constant J with the distance r to a localized magnetic impurity (RKKY interactions). Its sign fluctuates, producing a ferromagnetic interaction when $J > 0$ (red) or an antiferromagnetic one when $J < 0$ (blue). (d) The 'Doniach phase diagram'[110] for Kondo-lattice systems: T_K , T_{RKKY} and T_N as a function for antiferromagnetic exchange-coupling J (> 0). reproduced from [111]. Note that the J is defined differently in Fig 6.1c and 6.1d.

localized electrons in the inner shells of the magnetic impurities hybridizing with the conduction electrons (red), which is superimposed to the wider band coming from the conduction band of the metal host (green) (Fig. 6.1b [108]).

Materials with periodically arranged local magnetic moments are referred as Kondo lattice. In these materials, the Kondo effect competes with the interaction between the magnetic impurities in the material, which are mediated by the conduction electrons of the host metal. This magnetic interaction is known as RKKY interaction [112, 113], and it depends on the distance between the impurities (decreases with the distance), which can interact either ferromagnetically or antiferromagnetically (see Fig. 6.1c). The competition between the Kondo effect and the RKKY interactions determine the different magnetic phases that arise at low temperatures, as shown in Doniach phase diagram

in Fig. 6.1d. When $T_K < T_{\text{RKKY}}$, magnetic order (in most cases antiferromagnetic) sets in below T_N . At large J , where $T_K > T_{\text{RKKY}}$, a paramagnetic phase is formed which shows the signatures of a heavy Fermi liquid. A quantum phase transition between the magnetically ordered phase and the paramagnetic phase exists at $J = J_c$ in the zero-temperature limit [111].

Heavy electron metals (heavy fermions) are intermetallic Kondo lattice compounds in which one of the constituents is a rare-earth or actinide atom, with partially filled $4f$ - or $5f$ - electron shells (such as Ce, U, Yb) [114]. As these materials are cooled down, some of the f -electrons order spontaneously, mostly antiferromagnetically (AF) and some become itinerant at low temperatures and thus the electrons showing both localized and delocalized, i.e. correlated behavior. The hybridization of conduction electrons with the localized orbitals results in low-energy excitations with a heavy effective mass (~ 3 orders of magnitude higher than normal electron mass). This hybridization between f orbitals and itinerant electrons is extremely sensitive to tuning parameters such as pressure, magnetic field and chemical dopants can change the phase towards an AF ordered ground state and in some cases unconventional superconductivity at very low temperatures [115] (Fig. 6.2a). The main signature of heavy fermions is the high electronic specific heat coefficient ($\gamma = C/T$), usually $\gamma > 400 \text{ mJ/mol.K}^2$. The first heavy Fermion compound was discovered in 1975 [116].

A novel method to study the electronic excitations of correlated electron systems locally with atomic resolution is spectroscopic-imaging scanning tunneling microscopy (SI-STM). This technique has been extensively used to study high temperature superconductors such as Cuprates family [117, 118] and more recently on iron-based superconductors [119–121] to learn about the mechanism of superconductivity. Furthermore, SI-STM has been used to study heavy Fermion compounds such as URu_2Si_2 [109, 122] for analyzing the hidden order phase, $CeCoIn_5$ for visualizing the heavy fermions [106, 123, 124] and $CeRu_2$ for visualizing the vortex lattice [125].

6.1.1 Introduction to $CeCu_2Si_2$

The first observation of superconductivity in heavy electron metals was made in $CeCu_2Si_2$ in 1979 [6], which was quite unexpected. Prior to this discovery it was believed that local magnetic moments (in this case Cerium), would eliminate conventional s -state (or singlet) superconductivity by splitting the Cooper pairs. This heavy-fermion superconductor is located at ambient pressure very close to an AF quantum critical point (QCP). $CeCu_2Si_2$ crystallizes in the body centered tetragonal structure (Fig. 6.2b), with a $T_C \simeq 600 \text{ mK}$ and an upper critical field of about 2T. This material has been

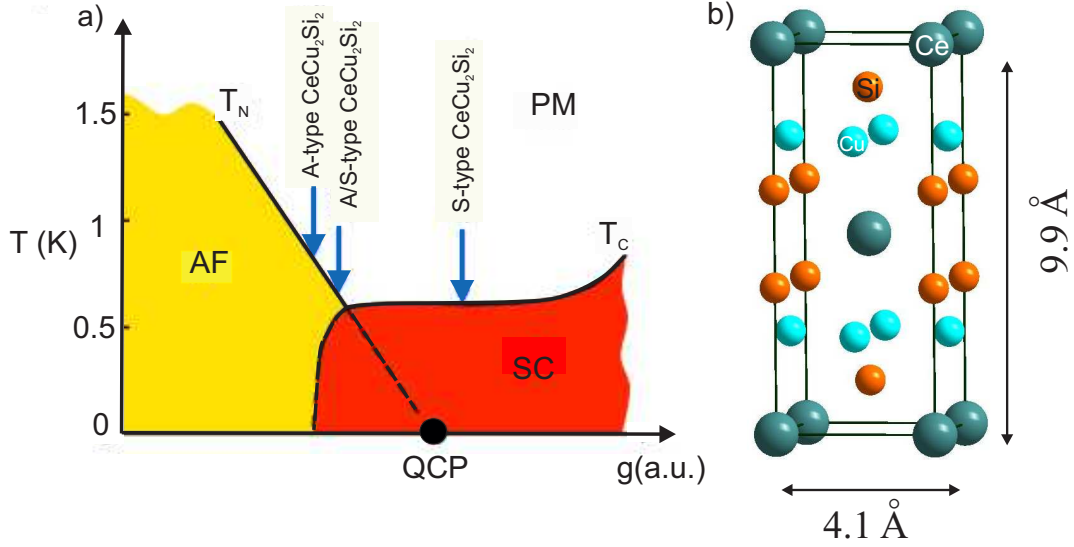


FIGURE 6.2: (a) Phase diagram of $CeCu_2Si_2$ reproduced from [126]. (b) Body centered tetragonal structure of $CeCu_2Si_2$.

extensively studied at low temperature thermodynamic and transport measurements [127]. Recently magnetic neutron scattering results have been obtained which relate the superconducting pairing symmetry to spin excitations instead of phonons [126]. Additionally, angle-resolved resistivity measurements of the upper critical field H_{C2} revealed a fourfold oscillation of H_{C2} , suggesting a d_{xy} symmetry of the order parameter [128].

6.1.1.1 Sample preparation and heat-capacity measurements

This project has been a collaboration between our group and MPI-Dresden (S. Seiro, S. Wirth, G. Geibel and F. Steglich) who prepared the single crystals. $CeCu_2Si_2$ single crystals were grown in Cu self-flux starting from polycrystals of nominal composition $Ce_{1.1}Cu_2Si_2$ and metallic Cu in a 3:2 molar ratio. These products were heated to $1570^\circ C$ in an Al_2O_3 crucible under Ar atmosphere and cooled down by a Bridgman technique [129]. The I4/mmm crystal structure was confirmed by x-ray powder diffraction on a crushed single crystal, yielding lattice parameters $a=4.1031 \text{ \AA}$ and $c=9.9266 \text{ \AA}$. The superconducting transition temperature determined from specific heat measurements was 0.59K as shown in Fig. 6.3. As these crystals do not present a preferential cleaving plane, a groove was cut around a perimeter perpendicular to the c axis in order to facilitate a breaking of the crystal in the ab plane. The sample was cleaved in-situ in cryogenic vacuum at 4K to avoid surface contamination.

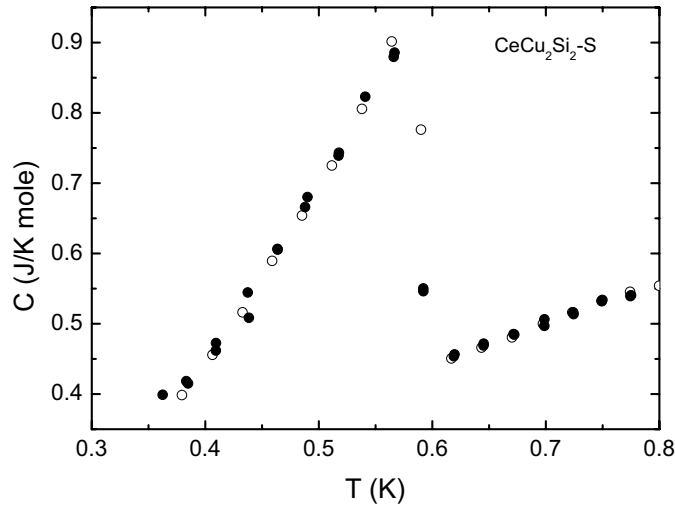


FIGURE 6.3: Heat capacity measurements on $CeCu_2Si_2$, showing the superconducting transition temperature at $\simeq 600$ mK. (From S. Seiro)

6.2 Results

After several unsuccessful cleaving attempts which resulted into rough surfaces, finally we were able to cleave the sample with a flat surface. After cleaving the sample at the 4K- Plate the sample was immediately placed in the STM- head. Measurements were taken at different temperatures ranging from 200mK to 700mK. Conductance spectra were measured with a lock-in amplifier frequency of 411 Hz and lock-in modulation of about $40\mu V$. All the spectra were normalized well above the superconducting gap at $300\mu V$ to get a good comparison. In the following sections I will present the topography and the spectroscopic results.

6.2.1 Topography and periodic rows

Initially, a flat region in an area of several hundred nanometers was found (Fig. 6.4a). If we scan in a smaller area with high resolution we see modulations of atoms with Picometer corrugation, indicating the atoms (Fig. 6.4b). The line cut as well as the FFT of the topography can also be seen in Inset of Fig. 6.4b, the distance between the Bragg peaks corresponds to $\frac{1}{a}=0.25\text{\AA}^{-1}$, indicating that the modulations represent the atoms, which have periodicity, with distance between two neighboring atoms being about 4\AA . However in the perpendicular direction the distance between the rows is not the same, which indicates that the cleave is not on the (001) plane, but with a plane which has an angle with respect to (001) plane. This angle can be calculated from the slope of the topography without performing plane subtraction, which is about $\alpha = \arctan(\frac{17}{150}) \simeq 6^\circ$.

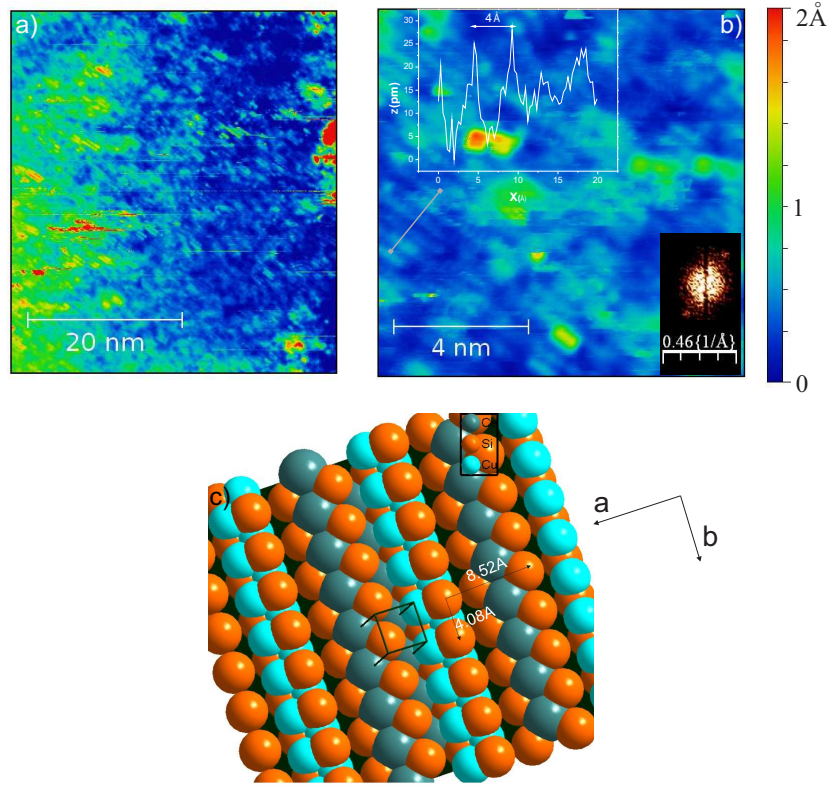


FIGURE 6.4: (a) Topography image of about $40 \times 50 \text{ nm}^2$, obtained using a setpoint of 100 mV for the bias voltage and 60 pA for the tunneling current. (b) Scanning over a small area of about $10 \times 10 \text{ nm}^2$, images are obtained using a setpoint of 100 mV for the bias voltage and 80 pA for the tunneling current. Inset: Fast Fourier Transform (FFT) of the image shows two Bragg peaks indicating periodicity in the topography. Additionally, the line profile in the inset shows the distance between the atomic rows in one direction to be on the order of 4 Å. (c) The possible surface termination (1 0 7), which has 6° angle with respect to (0 0 1) plane.

Therefore the cleaved plane should obey the equation :

$$\cos 6^\circ = (h \ k \ l) \cdot (0 \ 0 \ 1) / \sqrt{h^2 + k^2 + l^2} = 0.99 \quad (6.1)$$

The surface termination which fits well with the equation is (1 0 7), which can be seen in Fig. 6.4c. This indicates that what we scan on the surface is Si atoms.

6.2.2 Spectroscopy in large energy range and superconducting gap as a function of temperature

After observing the topography, we took conductance spectra, at large and small energy ranges. At large energy ranges we expect to see a Fano feature, which can be written as [130]:

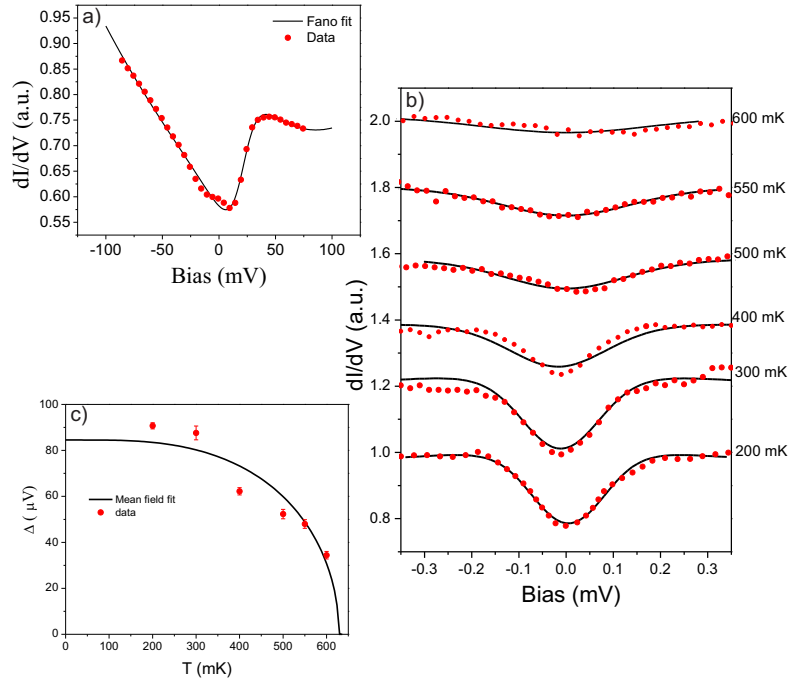


FIGURE 6.5: (a) Conductance spectra taken at ± 80 mV, fitted with Fano function (Eq. 6.2). (b) Superconducting gap as a function of the temperature. The superconducting gaps are fitted with Dynes equation (Eq. 2.17). (c) Gap size as function of temperature extracted from Dynes equation, fitted with a mean field function (Eq. 5.1). For all of the figures, red points are the data points whereas the black lines are from the fits.

$$\frac{dI}{dV} = G_0 + \frac{A}{(1+q^2)} \times \left(\frac{[q + \frac{(E-\varepsilon)}{\Gamma/2}]^2}{1 + [\frac{(E-\varepsilon)}{\Gamma/2}]^2} \right) \quad (6.2)$$

where q (known as the Fano parameter), is the ratio of the electrons tunneling into *real-space* many body state or into delocalized *momentum-space* electrons. Γ is the hybridization strength between the f electrons (from Ce) and the conduction electrons, also known as the resonance width, and it is inversely proportional to the effective mass m^* of the carriers in the heavy fermion system. ε is the energy of the many body state. G_0 is the conductance at zero bias voltage, A is the amplitude of the dip. The latter two parameters are dependent on local density of states of the sample. In Fig. 6.5a the spectra as well as the Fano fit can be seen. The fitted values yield $q = 0.89$, $\Gamma = 40$ mV, and $\varepsilon = 20$ mV. The Fano function describes how resonances are measured in tunneling spectroscopy. It results from interferences between two scattering intensities, one due to scattering within a continuum of states (the background delocalized *momentum-space* electrons) and the second due to an excitation of a discrete state (the resonant *real-space* many body state electrons). Since $CeCu_2Si_2$ is a Kondo lattice, the Fano

feature would be expected. In other heavy Fermion compounds (e.g. URu_2Si_2 [109] or $CeCoIn_5$ [131]) the Fano feature has already been reported.

The most interesting feature about this material is its superconducting behavior, which can be studied with a milli Kelvin STM. We took conductance spectra at 200mK to observe the superconducting gap. The gap did not open fully, but just about 25 percent down. In order to relate the gap with superconductivity, we did series of measurement to have enough proof. Initially, we took temperature dependent spectra to see how the gap varies as the temperature rises from 200 mK to its $T_c \simeq 630$ mK. In Fig. 6.5b the spectra as a function of temperature are shown with the red points. As it is shown the gap vanishes as it reaches the critical temperature, thus an indication that the gap is related to superconductivity. The fact that the gap does not go to zero at 200 mK, indicates that there is still some density of states, near the Fermi level. This could be because of the proximity effect, meaning that on the surface we have normal state, but because of the proximity to the superconducting bulk, a weak gap arises. The reason why the surface is not superconducting might be because of the surface termination, depending on the atoms on the surface (probably Si) superconductivity might vanish. Another reason could be due to the possible nodes of the gap values on the Fermi surface. Furthermore, there might be coupling of the magnetic excitations with superconductivity which might affect the superconducting gap. Furthermore, at each temperature, the density of states has been fitted with the Dynes equation (Eq. 2.17), as shown with the black lines in Fig. 6.5b, which match well with the experimental data.

In Fig. 6.5c, the temperature dependence of the superconducting gap can be seen in red points. Δ is obtained from the Dynes equation (2.17), using a constant $\Gamma = 120 \mu V$. The value of gap at 200 mK is $\Delta_0 = 90.7 \pm 1.35 \mu V$, which is equivalent to $1.67 k_B T$, which is a bit smaller than the the BCS limit ($1.76 k_B T$). The points are fitted with the mean field equation (Eq. 5.1), as shown with the black lines.

6.2.3 Field dependence spectra

Another proof of the relation to the superconductivity is the magnetic field dependent spectra. In Fig. 6.6, the value of zero bias tunneling conductance (ZBTC) as a function of magnetic field can be seen. As we increase the field the gap vanishes which is equivalent to increase in value of ZBTC.

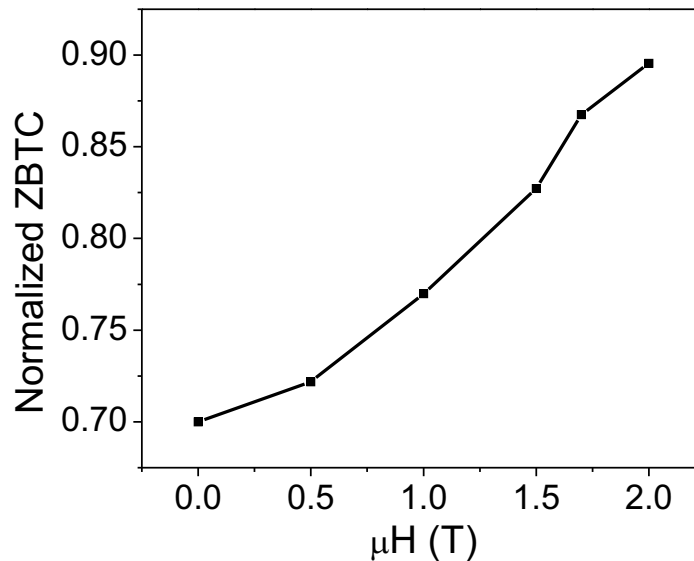


FIGURE 6.6: ZBTC of the averaged spectra as a function of the magnetic field. As the field increases the gap tends to disappear.

6.2.3.1 Observation of vortices as a function of field

One of the unique features of spectroscopic imaging-STM is the ability to visualize the vortex cores. This could be done by taking spatial maps at ZBTC. In type two superconductors, vortices appear when we are in the range of $H_{C1} < H < H_{C2}$. In this range there would be formation of vortex cores to minimize the internal energy. These vortices usually arrange themselves in triangular lattice (Abrikosov lattice)[132] due to repulsive interaction between them, and seldom change to square lattice [133] either by thermal agitation or quenched disorder. In the vortex there is no superconductivity and hence no gap, however, in some cases localized states near the Fermi level have been reported, where a peak emerges.

The ZBTC map were taken at different magnetic fields (0.5, 1, 1.5, 1.6, 1.7 Tesla) (Fig. 6.7), in the field of view of about $150 \times 150 \text{ nm}^2$. The triangular lattice symmetry is clearly resolved.

6.2.3.2 Average distance between vortices as function of field

As it can be seen from Fig. 6.7, by increasing the magnetic field (B), the number of vortices (N) in the same area (A) increases. The number of vortices (N) for a specific

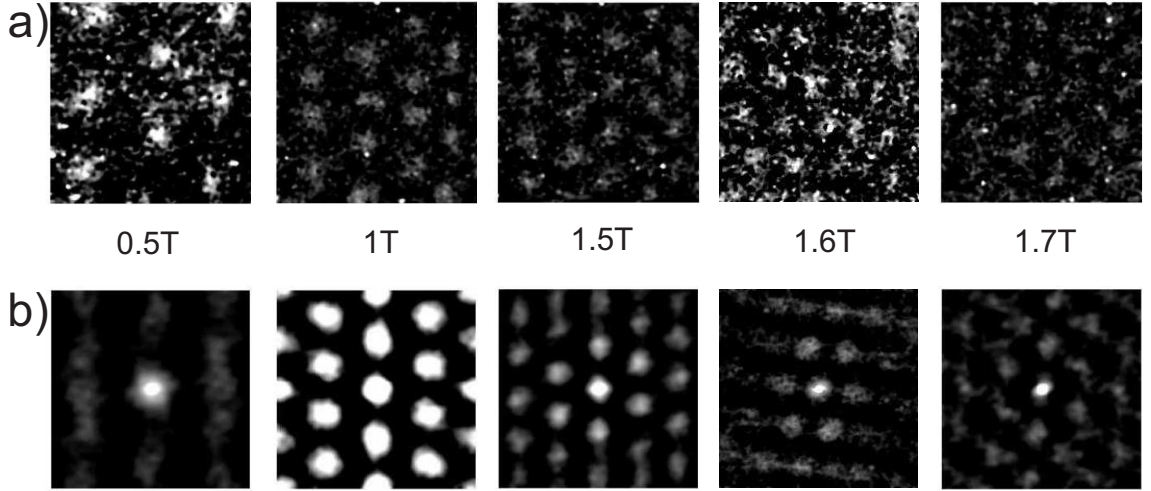


FIGURE 6.7: (a) ZBTC maps, taken at 0.2 K over a scanning area of $150 \times 150 \text{ nm}^2$ as a function of the magnetic field, $B = (0.5, 1, 1.5, 1.6, 1.7 \text{ T})$. The data have been filtered for better contrast. The triangular vortex structure is clearly seen. (b) The autocorrelation of the vortex lattice for better visualizing the triangular lattice symmetry.

magnetic field (B), and an area of (A) can be calculated from the equation:

$$N = \frac{B \cdot A}{\Phi_0} \quad (6.3)$$

where $\Phi_0 = h/2e$ is quantum of magnetic flux for each vortex.

In the case of triangular lattice symmetry, since $A = \frac{\sqrt{3}}{2} d^2$, the distance between two neighboring vortices (d) is:

$$d = \left(\frac{2}{\sqrt{3}} \frac{\Phi_0}{B} \right)^{\frac{1}{2}} \quad (6.4)$$

the distance d is inversely proportional to the square root of the magnetic field B .

In Fig. 6.8 the distance between the vortices as a function of magnetic field is shown.

6.2.3.3 Extraction of coherence length from data and from autocorrelation of data

Furthermore, by analyzing a single vortex core, we could find out about the coherence length by analyzing the ZBTC (σ) and how it changes from the center of the vortex core to the corner. This corresponds to the exponential decay which we expect in vortices [134].

$$\sigma(r, 0) = \sigma'_0 + (1 - \sigma'_0) \times \left(1 - \tanh \frac{|r|}{\xi} \right) \quad (6.5)$$

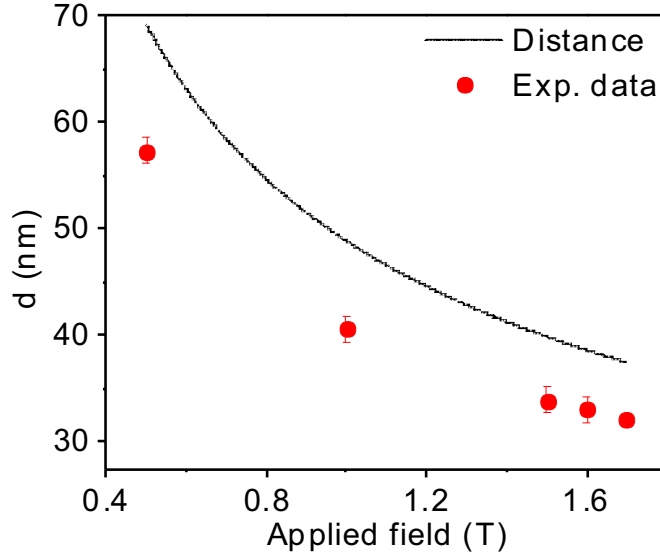


FIGURE 6.8: Distance between the vortices as a function of magnetic field. The line is following Eq. 6.4. The difference between the data and the theoretical values can be attributed to the calibration of the scan piezo, which is has about 10 percent.

Where σ'_0 is the value for σ at the center of the vortex and ξ is the coherence length.

After fitting ξ with Eq. 6.5, we get the value of 9.3nm which is consistent with the previous report [135]. Fig. 6.9a shows the fit to Eq. 6.5. However, as it can be seen near the center there is a big noise. In order to reduce the noise, it is possible to use the autocorrelation intensity to obtain the coherence length using:

$$\sigma(r, 0) = a + c \tanh\left[\frac{|r|}{\xi^*}\right]^2 \quad (6.6)$$

where a and c are constants. By simulating Eq. 6.5, with an arbitrary coherence length value it is possible to plot a vortex (which the radius is proportional to the coherence length). Furthermore, by taking the autocorrelation of Eq. 6.5, we can compare the ratio of the coherence length values obtained from the map and the autocorrelation of the map. For that, we have to compare the line profiles from the center to the edge of the vortex of the two maps and fit them with Eq. 6.5 and Eq. 6.6. From the fits the coherence lengths are determined. The ratio between the coherence length obtained from the autocorrelation and the real space image is 1.32. We should consider this ratio for obtaining the coherence length value from the autocorrelation of the map.

Fig. 6.9b shows the fit to Eq. 6.6, giving $\xi^* = 7.99$ nm. Therefore, $\xi = \xi^*/1.32 = 6.15$ nm.

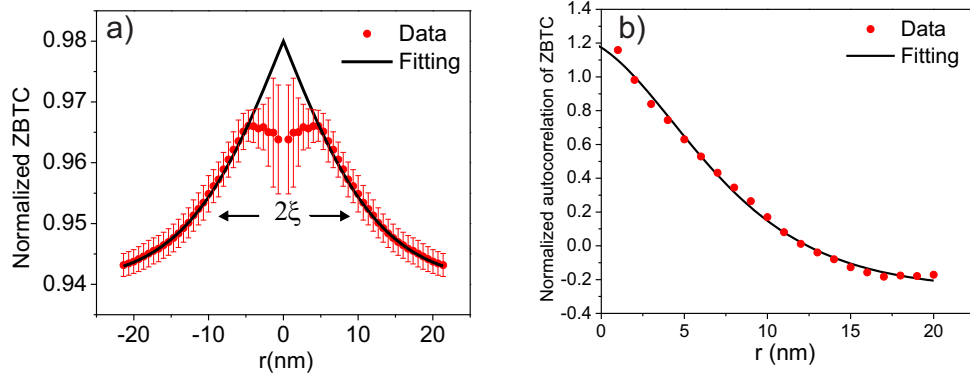


FIGURE 6.9: Evolution of the radial average of the normalized zero bias tunneling conductance $\sigma(r, 0)$ at 0.2 K and 1.6 T as a function of the radial distance from the vortex center r (red points). a) The black line is the fit to Eq. 6.5, which gives $\xi = 9.3$ nm. b) The black line is the fit to Eq. 6.6, which gives $\xi = 6.15$ nm.

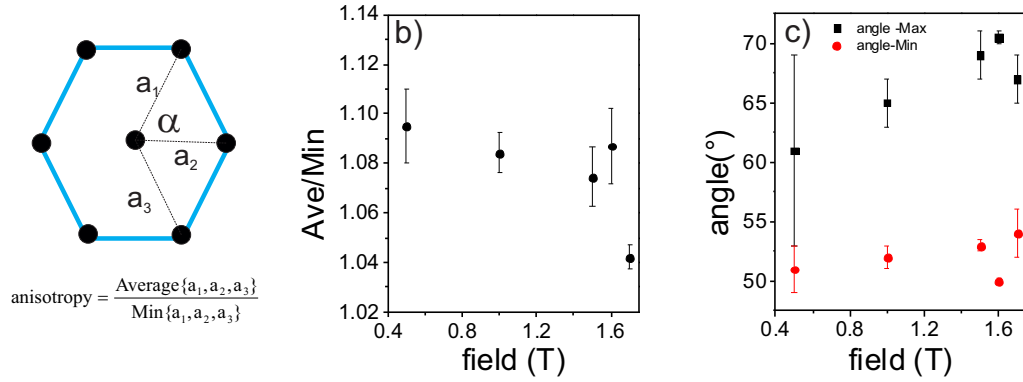


FIGURE 6.10: a) Determining the anisotropy of the vortex from the autocorrelation of the vortex lattice. b) Variation of the anisotropy of the vortex lattice as a function of the applied magnetic field. c) The maximum and minimum angle dependence of the vortex lattice as function of the applied magnetic field.

From $\xi = 9.3$ nm, taken from the real space map, we can derive the Fermi velocity from Eq. 6.7, which is equal to 4058 m/s, in agreement with previous studies [128].

$$v_F = \frac{\xi k_B T_C}{\hbar \times 0.18} \quad (6.7)$$

6.3 Conclusion and summary

In this chapter the superconductivity of $CeCu_2Si_2$ has been studied. The superconducting gap did not open fully and reduced about 25%. Recently, the superconducting gap of another heavy Fermion compound ($CeCoIn_5$) has been measured with STM, which also did not open fully [106, 124]. Furthermore, the evolution of the superconducting gap as a function of the temperature and magnetic field has been discussed. The vortex lattice has been illustrated as a function of magnetic field, where the triangular lattice is visible at different fields. This is the first imaging of the vortex cores of this material. From the anisotropy of the vortex lattice the symmetry of the order parameter can be studied (e.g. [136–138]). Furthermore, vortex lattice phase diagram of heavy fermion compounds have previously been measured by magnetic neutron scattering and STM (e.g. $CeCoIn_5$ in [106, 124, 139]) and have shown variations from triangular to square and rhombic. The measurements of the vortex lattice in $CeCu_2Si_2$ is experimentally more complicated due to the lower T_c and H_{c2} of $CeCu_2Si_2$ (600 mK and 2T) with respect to $CeCoIn_5$ (2.2 K and 5T). Our results indicate triangular vortex lattice with a bit anisotropy as the magnetic field increases shown in Fig. 6.10b. This can be sign of a d-wave order parameter [140]. The angle dependence of the vortex lattice for different fields is shown in Fig. 6.10c, where at 1.5T a large increase can be seen.

Chapter 7

Tunneling measurements on magnetic phases of CeB₆

7.1 Introduction

Hexaboride materials have attracted great amount of attention over the last four decades, due to their intriguing transport and magnetic properties [141]. CeB₆ is one of the hexaborides which is also a heavy fermion material. The electronic states near the Fermi level of CeB₆ are composed of localized cerium-4f levels hybridized with itinerant cerium-5d and boron-2p electrons [142]. Its resistivity possesses a Kondo-like minimum near 150 K, and shows semiconducting, paramagnetic (PM) behavior down to approximately 3 K [143]. At 2.3 and 3.2 K and at zero field, antiferromagnetic (AFM) and quadrupolar (AFQ) ordering occur, respectively, as shown in Fig. 7.1a and the resistivity is metallic at the lowest temperatures [144, 145].

As can be seen the magnetic phase diagram has an anisotropic behavior, meaning that the orientation of the crystal is determinant on its property. CeB₆ has a cubic structure, as it can be seen in Fig. 7.1b. The rich magnetic phase diagram of this material suggests that there might be change in the conductance spectra as the phase varies either by applying a magnetic field or changing the temperature. Recently, inelastic neutron scattering revealed a resonant magnetic excitation mode [147]. Point contact measurements have been carried out as a function of temperature and magnetic field [148, 149], which have shown good agreement with the temperature dependence and field dependence of the bulk resistivity.

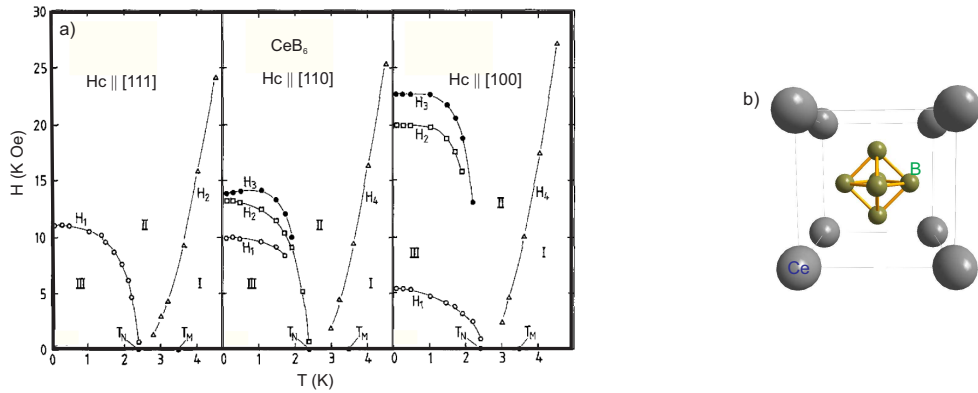


FIGURE 7.1: (a) The magnetic phase diagram of CeB_6 at low temperatures with three different orientations, indicating the anisotropic nature of the crystal. At zero field $T_N = 2.3$ K and $T_Q = 3.2$ K. The figure is reproduced from [146]. (b) The crystal structure of CeB_6 showing a cubic lattice structure.

Planar tunneling junction measurements have indicated a small, asymmetric gap appearing at approximately 45 mV; however, the measurements were carried out at temperatures between 13 K to 53 K [150].

In this work the first STM measurements on CeB_6 has been performed and the temperature as well as field dependence measurements have been carried out.

7.2 STM measurements

7.2.1 Topography

The crystals were obtained from D. Inosov from Max-Planck-Institute for solid state research in Stuttgart. The crystals were oriented in (100) orientation, where it is the easy cleave orientation. After successfully cleaving the sample I was able to see step edges in large area of 90×90 nm², as shown in Fig. 7.2a. If we take a high resolution topography on the dashed circle of Fig. 7.2a, we see the atoms in an area of 20×14 nm² and 3.5×3.5 nm² in Fig. 7.2b and c respectively. The FFT of the topography showing the atomic peaks in the reciprocal space can be seen in Fig. 7.2d. The quality of the topography is strongly tip dependent and with a blunt tip we were not able to observe the atoms.

7.2.2 Temperature dependence of spectra

In the range of ± 20 mV, the conductance spectra taken at the temperature of 100 mK shows an anisotropic kink, shown in Fig. 7.3a. In order to see how the spectra changes

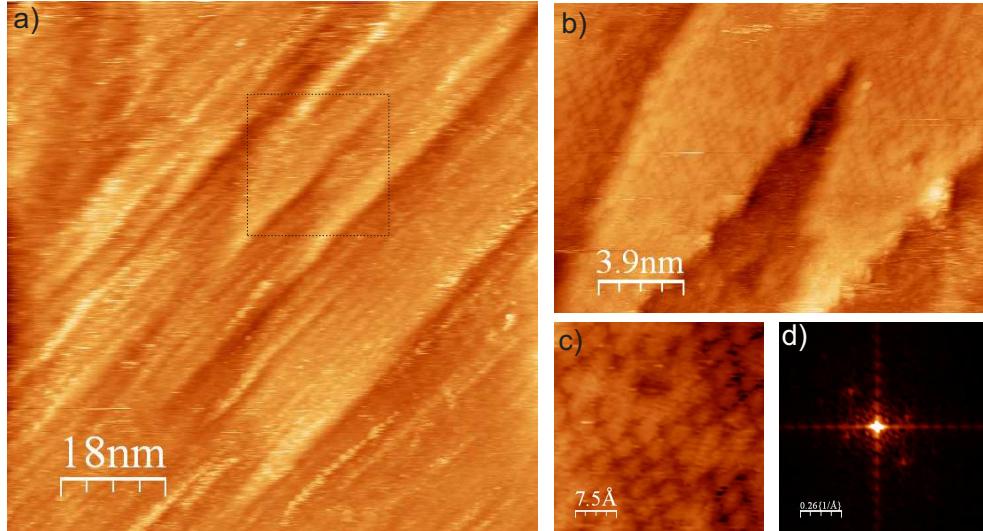


FIGURE 7.2: (a) Topographic image of CeB₆ step edges in an area of $90 \times 90 \text{ nm}^2$. Setpoints: $V_b=80 \text{ mV}$, $I_t=0.1 \text{ nA}$, taken at $T=8.5 \text{ K}$. (b) The topography of the dashed rectangle in (a) shown with higher resolution in an area of $20 \times 14 \text{ nm}^2$. Setpoints: $V_b=100 \text{ mV}$, $I_t=0.1 \text{ nA}$. (c) The atomic resolution topography in an area of $3.5 \times 3.5 \text{ nm}^2$. (d) FFT of the topography showing the atomic peaks.

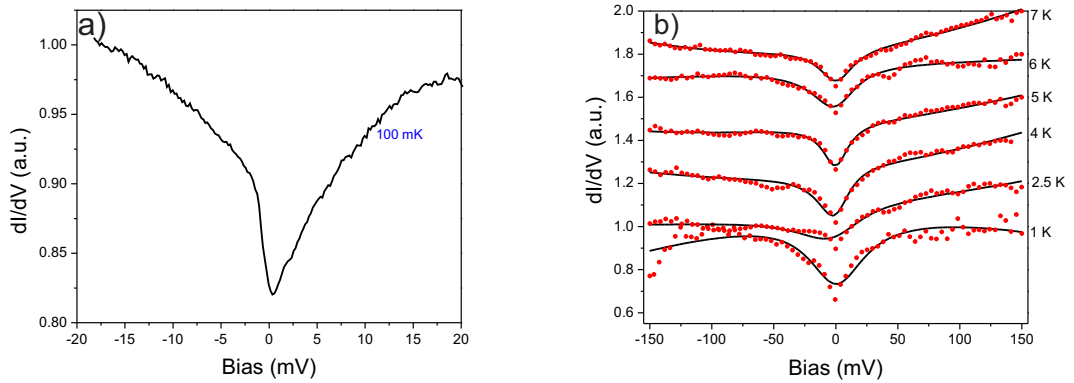


FIGURE 7.3: (a) Conductance spectra taken in the range of $\pm 20 \text{ mV}$, taken at 100 mK . (b) Conductance spectra taken in the range of $\pm 150 \text{ mV}$ as a function of temperature from 7 K to 1 K , with the Fano fits (Eq. 6.2). Offset in y axis is used for clarity.

with different phases I measured the conductance spectra as a function of temperature in the range of $\pm 150 \text{ mV}$, as shown in Fig. 7.3b.

These curves have been fitted with the Fano function (Eq. 6.2), with the resonance being centered at $\varepsilon = 0$.

The resonance width, Γ , has the average value of $41.6 \pm 14.9 \text{ (mV)}$ for the measured temperatures. This value is consistent with the planar junction measurements [150], which has been reported to be approximately 45 mV .

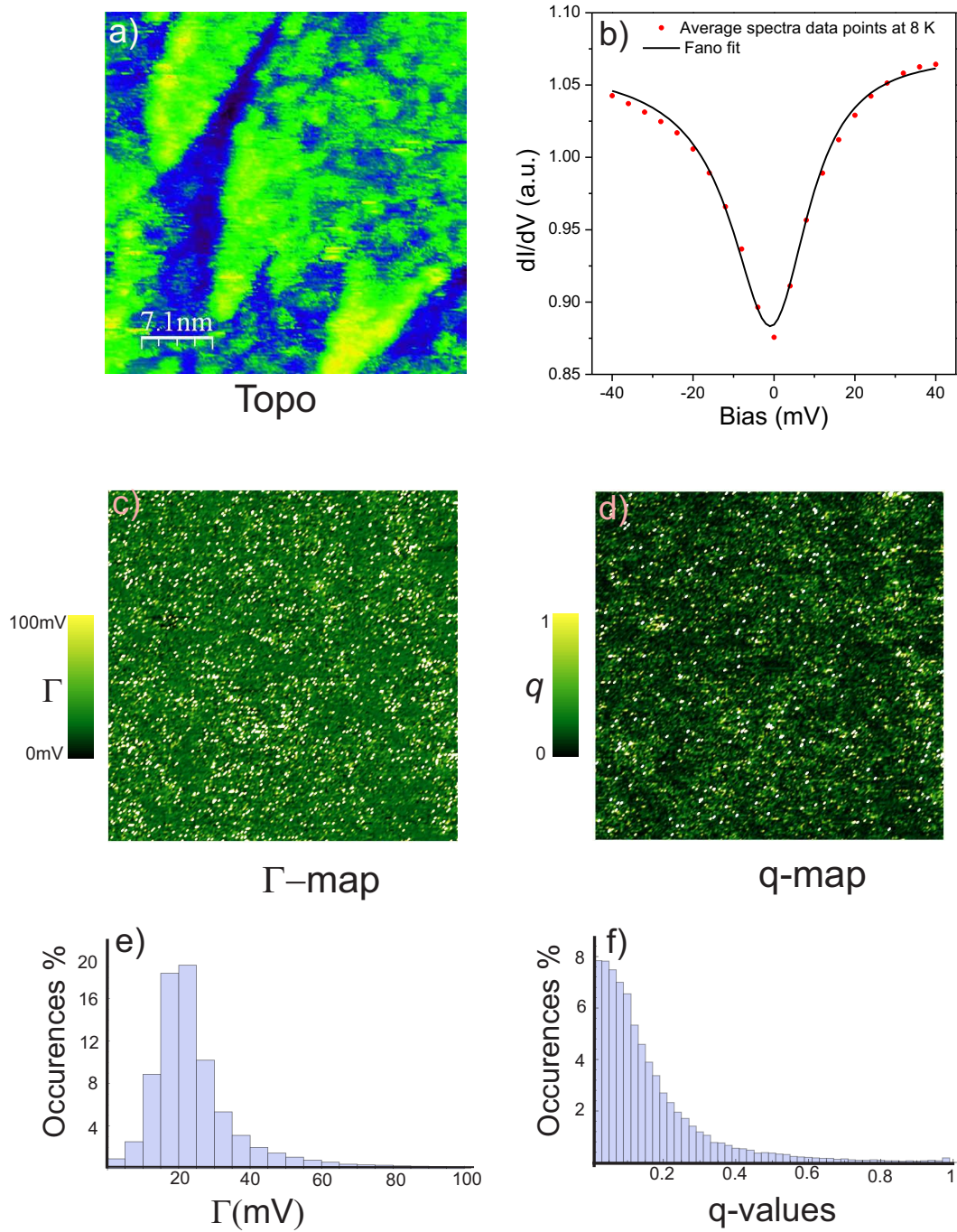


FIGURE 7.4: (a) Topography of the map showing the step edges, at an area of $35 \times 35 \text{ nm}^2$ with 200×200 pixels. (b) Average spectra of the map (from 40000 spectra) with the Fano fit. The map has been taken at 8 K (PM phase). (c) Spatial map of Γ , the color scale can be seen. (d) Spatial map of q . (e) Histogram of Γ , for each different Γ value, the percentage of occurrences is obtained, the majority of the values are below 30 mV . (f) Histogram of q , showing the percentage of occurrences.

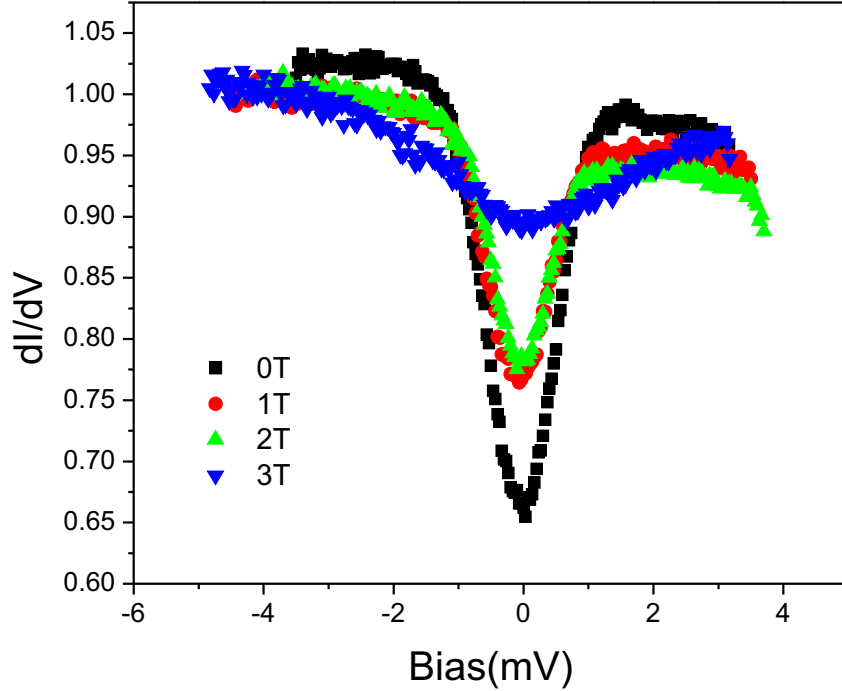


FIGURE 7.5: Conductance spectra taken in the range of ± 4 mV as a function of magnetic field from 0 Tesla to 3 Tesla at base temperature.

In order to see the spatial inhomogeneity in the DOS, a spectroscopic map near a step edge was taken as shown in Fig. 7.4. The map was taken at 8K, which implies that we are in the PM phase. The average spectra of the map has been fitted with Fano function (Eq. 6.2) as shown in Fig. 7.4b, and has $G_0= 0.8$, $\Gamma =20$ mV, and $q= 0.05$. Furthermore, by fitting the spectra for each pixel of the map with Fano function, it is possible to spatially derive the Fano parameters values (seen in Fig. 7.4c, and Fig. 7.4d for Γ and q respectively). The histograms of Γ and q can be seen in Fig. 7.4e and Fig. 7.4f respectively. The Γ and q maps do not show a drastic change near the step edge, suggesting that the step edge does not affect the Fano resonance.

7.2.3 Field dependence spectra

In order to see how the conductance spectra varies as function of the magnetic field, we applied fields from 0 Tesla to 3 Tesla with 1 Tesla steps in the range of ± 4 mV, as shown in Fig. 7.5, all measurements were done at base temperature. By ramping the field from 0 T to 3 T at 10 mK, there is phase transition first from AFM to SDW, and then from SDW to PM.

As can be seen, there is a formation of gap at the AFM phase (at 0 Tesla), and as the field increases the gap tends to reduce. Since the crystal orientation is (1 0 0), the magnetic phase at 1 T and 2 T are the same (as seen in Fig. 7.1) and thus the spectra look quite similar; however, at 3 T the phase changes to PM and thus the gap diminishes. The observation of the AFM gap is consistent with the point contact measurements which had been done already in 1985 [149], where at the AFM phase, a gap with the size of 2 mV appears and closes as the temperature is raised and the phase changes to AFQ and eventually to PM.

7.3 Summary and conclusion

The intriguing magnetic phase of the crystal makes this material an exciting candidate for STM measurements. We have performed measurements on atomically flat CeB_6 surface on the (100) orientation, where we have seen atomically flat surface. We have done spectroscopic measurements as a function of temperature and magnetic field to analyze how the conductance spectra changes for various magnetic phases.

The thermal evolutions were fitted with the Fano function, where we observed resonance width on the order of 41.6 ± 14.9 meV, and an unusual reduction of the dip when the phase changes from PM to AFQ as the temperature is reduced; where the usual behavior was a deepening of the dip by reduction of temperature.

Finally, the field dependent measurements at ± 4 mV show a gap closing as the field increases. The gap is dependent on the magnetic phase of the crystal.

Chapter 8

Superconducting gap and vortex core on BiPd

Non-centrosymmetric superconductors are one class of materials in which triplet-pairing of the Cooper pairs can be realized. In this chapter, I study the superconductivity of the α -BiPd, a material which has recently attracted a lot of attention as a possible candidate for superconductivity with a triplet component. Only one superconducting gap with $\Delta \simeq 0.6$ meV has been observed. The temperature and magnetic field dependence of the gap is studied and found consistent with BCS theory with a single *s*-wave gap. Furthermore, a single vortex core with the bound state at the zero bias conductance has been detected. Eventually, the Josephson supercurrent between the BiPd sample and tip coated with BiPd has been measured.

8.1 Introduction

Superconductivity requires formation of a quantum condensate state by pairing conduction electrons, known as Cooper pair. The pair can be in a state of either total spin $S=0$ (spin-singlet) or $S=1$ (spin-triplet). In Fig. 8.1 the conventional classification of symmetry of Cooper pair can be seen. The antisymmetric spin-singlet state is associated with a symmetric orbital wave function (even parity) with orbital angular momentum $L=0$ (*s*-wave, e.g. Conventional BCS superconductors in Fig. 8.1a) or $L=2$ (*d*-wave, e.g. cuprates in Fig. 8.1b). The symmetric spin-triplet state is accompanied by an antisymmetric orbital wave function (odd parity) with orbital angular momentum $L=1$ (*p*-wave, e.g. ^3He , Sr_2RuO_4 in Fig. 8.1c) [151].

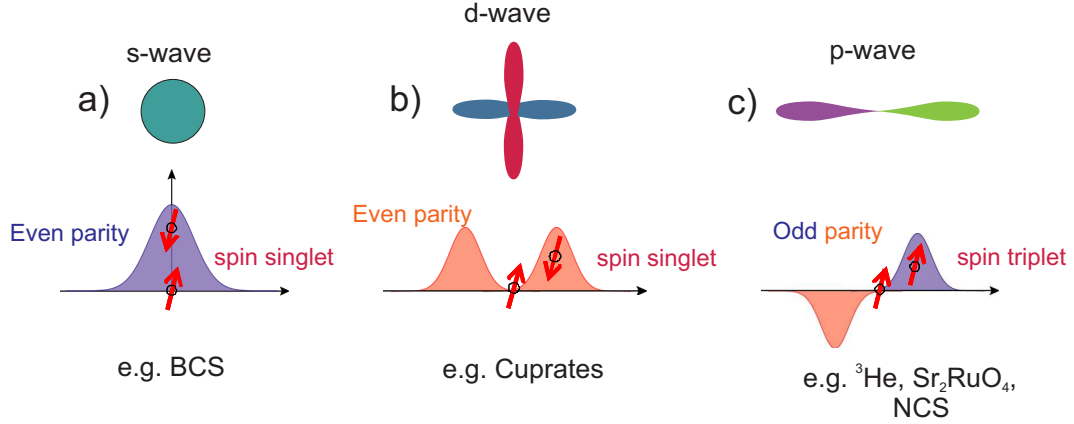


FIGURE 8.1: Conventional classification of symmetry of Cooper pair (a) an s-wave superconductor (e.g. BCS superconductor) showing an spin-singlet Cooper pair, with an even parity. (b) a d-wave superconductor (e.g. Cuprate) showing an spin-singlet Cooper pair, with an even parity. (c) a p-wave superconductor (e.g. ^3He , Sr_2RuO_4 , and NCS) showing an spin-triplet Cooper pair, with an odd parity.

An important group of materials, which show p-wave order parameter are Noncentrosymmetric (NCS) superconductors. NCS are materials which the crystal lattice has no inversion center. These materials gained a high focus for research after the discovery of the heavy fermion NCS CePt_3Si [152].

In a centrosymmetric superconductor, the wave functions of the Cooper pairs have to be even under inversion, unlike for a non-centrosymmetric superconductor. Therefore, the wave function of the Cooper pairs is allowed to also have a triplet component. In combination with Rashba spin-orbit coupling, the lack of inversion symmetry lifts the spin-degeneracy of the band structure. Since the spin-orbit coupling depends on the square of the atomic number (Z) of the elements involved, the presence of Bi ($Z=83$) is expected to result in a large spin-orbit coupling in this material [153]. Spin-triplet superconductivity has a number of interesting physical properties, specifically there are predictions for Majorana bound states to exist in the vortex cores of a spin-triplet superconductor [154, 155]. There are many non-centrosymmetric compounds in which superconductivity has been detected, such as BaPtSi_3 [156], $\text{Li}_2\text{Pt}_3\text{B}$ [157], etc. However, it has been difficult to clearly identify signatures of triplet pairing.

Here I demonstrate the results obtained from the superconductivity of α -BiPd, mainly by low temperature STM/STS. Non-centrosymmetric superconductivity in α -BiPd has been established already 60 years ago [158] and has recently been rediscovered [159, 160]. Thus the identification of this material as a noncentrosymmetric superconductor predates BCS theory, and it was not realized that NCSC was special until the discovery of an anomalously high H_{c2} in CePt_3Si [152], 50 years later. While in α -BiPd, local point contact experiments appear to yield multi-gap behavior and a zero bias peak at the

conductance spectra [153], nuclear quadrupolar resonance (NQR) rather points to a single gap behavior [160].

With the aid of STM, it is possible to image the atoms and defects and determine the plane termination. Additionally, with STS we can study the superconducting properties of BiPd, including the type of gap, field and temperature dependence of the gap, and even imaging the vortex core.

8.2 Results

8.2.1 Physical characterization of the crystal

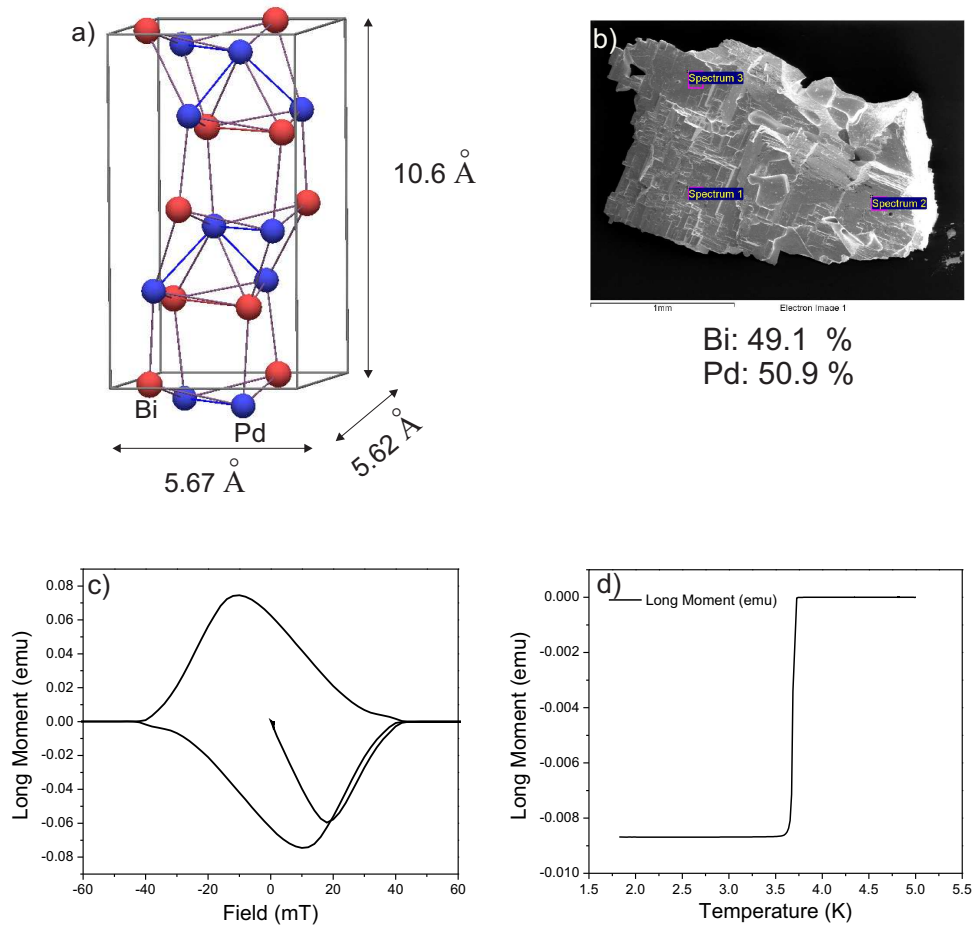


FIGURE 8.2: (a) The illustration of the crystal lattice structure of α -BiPd. (b) The SEM image of BiPd crystal together with EDX analysis. (c) Squid measurement determining the H_{c2} of the crystal to be $\sim 40\text{mT}$ (d) Squid measurements determining the $T_C \simeq 3.7\text{K}$.

Samples have been grown by D. Peets in the Max-Planck-Institute for Solid State Research in Stuttgart. The crystals were characterized by X-ray diffraction to confirm the

crystal structure to be monoclinic. An illustration of the crystal lattice of α -BiPd is shown in Fig. 8.2a. By EDX the element composition has been confirmed, as shown in Fig. 8.2b. The superconducting transition temperature has been detected both in SQUID magnetometry as well as transport experiments. We find a T_C of 3.7K and an H_{c2} of 40mT, as depicted in Fig. 8.2c,d.

The upper critical field, H_{c2} , is an order of magnitude lower than the previously reported crystal [159], this can be due to different possible phases in the crystal or different elemental composition. Further supplementary measurements can elucidate the reason.

8.2.2 STM measurements

8.2.2.1 Topography

The α -BiPd sample is cleaved perpendicular to the b axis. In the topography steps with different heights are observed on the sample surface.

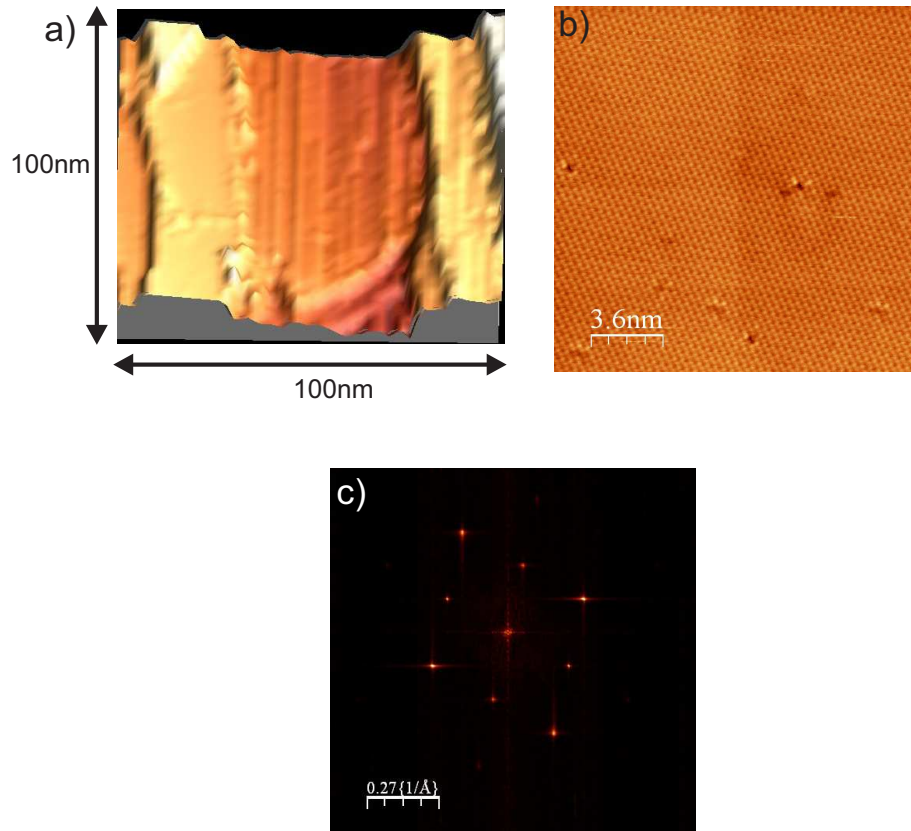


FIGURE 8.3: (a) Large STM topography of the α -BiPd surface. 100x100 nm². Setpoint: $V_b=60$ mV, $I=100$ pA. (b) Atomic resolutions image of the surface type A, 10x10 nm². Setpoint: $V_b=10$ mV, $I=100$ pA. (c) The FFT of the topography image.

A topographic image is shown in Fig. 8.3a, where different step edges are visible. The smallest step height is about 2.5Å, which is quarter of the lattice constant in the b

axis direction [159]. We have observed two different types of terminations which have a height difference of about 1\AA . An atomic resolution topography of the surface is shown in Fig. 8.3b. We can see that the lattice is distorted from the square lattice, which can be easily seen in the Fourier transformed image of the topography (Fig. 8.3c). Beside the lattice distortion there are also some extra modulations, which can be explained due to the lattice distortion in b axis direction.

8.2.2.2 Tunneling spectra

A typical conductance spectrum around the Fermi energy in the area with atomic resolution (Fig. 8.3b) is shown in Fig. 8.4. The spectrum is taken at the base temperature. The spectrum reveals only one superconducting gap. A fit of the spectrum with a simple isotropic s -wave order parameter gives a good description of the data (Eq. 2.10 [27]). From the fitting we get that the gap value Δ is about 0.6 meV , the electronic temperature around 140 mK and broadening of about $6\text{ }\mu\text{V}$.

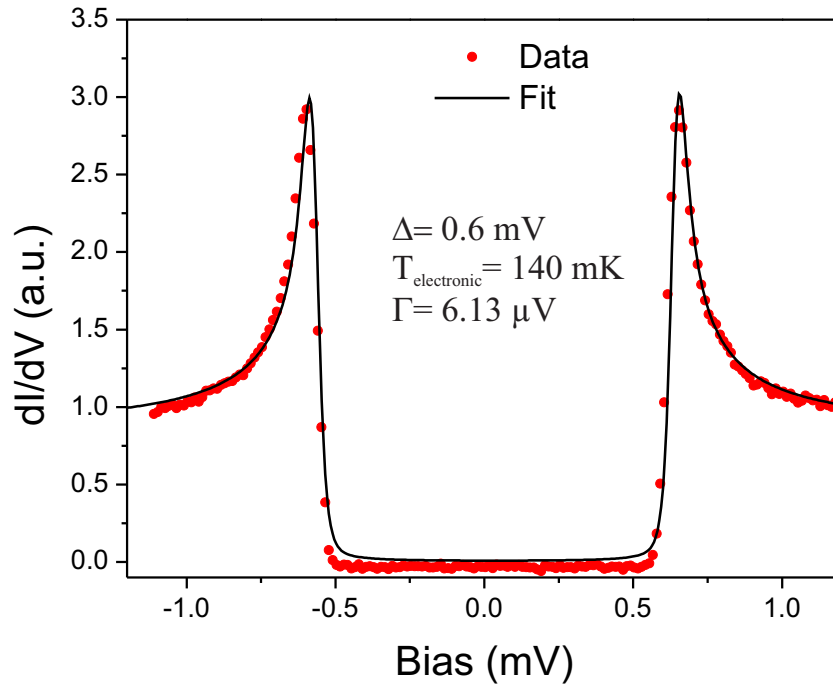


FIGURE 8.4: Conductance spectrum taken at base temperature. The spectrum is fitted with a simple Dynes formula with thermal broadening as discussed in the text.

8.2.2.3 Temperature dependence

In order to study the gap variation as function of temperature, we carried out series of measurements by recording the spectra as function of temperature. In Fig. 8.5a the spectra are shown, and the gap tends to vanish as the temperature approaches $T_C = 3.55$ K. The spectra were fitted with Dynes equation to derive the gap size, and fitted with BCS like (mean field) function plotted in Fig. 8.5b. Broadening increases by raising the temperature shown in Fig. 8.5c.

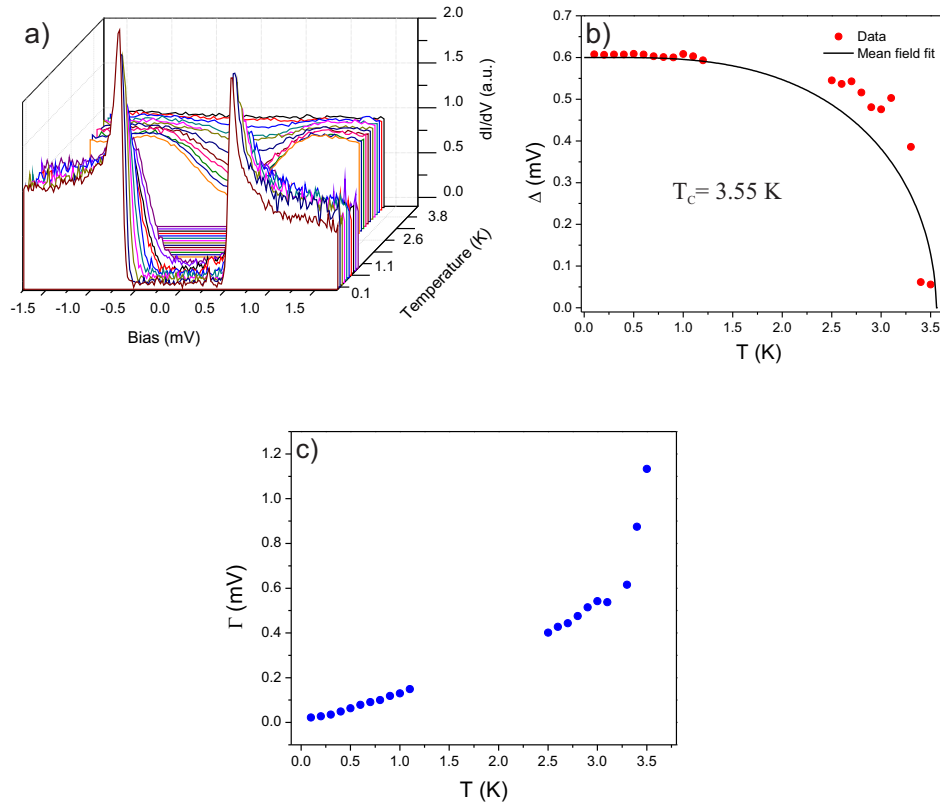


FIGURE 8.5: (a) Temperature dependence of the conductance spectra. By increasing the temperature the gap becomes weaker. (b) The gap size as a function of temperature. The solid line is the BCS like (mean field) fit, which gives a $T_C=3.55$ K. (c) The lifetime broadening as function of temperature extracted from the fit. By increasing the temperature, Γ increases.

The temperature dependence of the superconducting gap shows its disappearance at about 3.55K. This value is consistent with the critical temperature extracted from SQUID and transport measurements. If we take this value as the critical temperature T_C , it gives $2\Delta \simeq 3.93 k_B T_c$, which is slightly larger than the BCS prediction of $3.5 k_B T_C$.

8.2.2.4 Magnetic field dependence

By applying a magnetic field along the b axis, we studied the evolution of the conductance spectra. The spectra are taken at the same location on the sample. The spectra have been fitted using Dynes equation as discussed before in Eq. 2.18 (for $n=1$). The dependence of the superconducting gap as a function of the magnetic field is shown in Fig. 8.6a. The contour plot shown in Fig. 8.6b depicts the intensity of the conductance spectra, showing the gap vanishing around 60 mT.

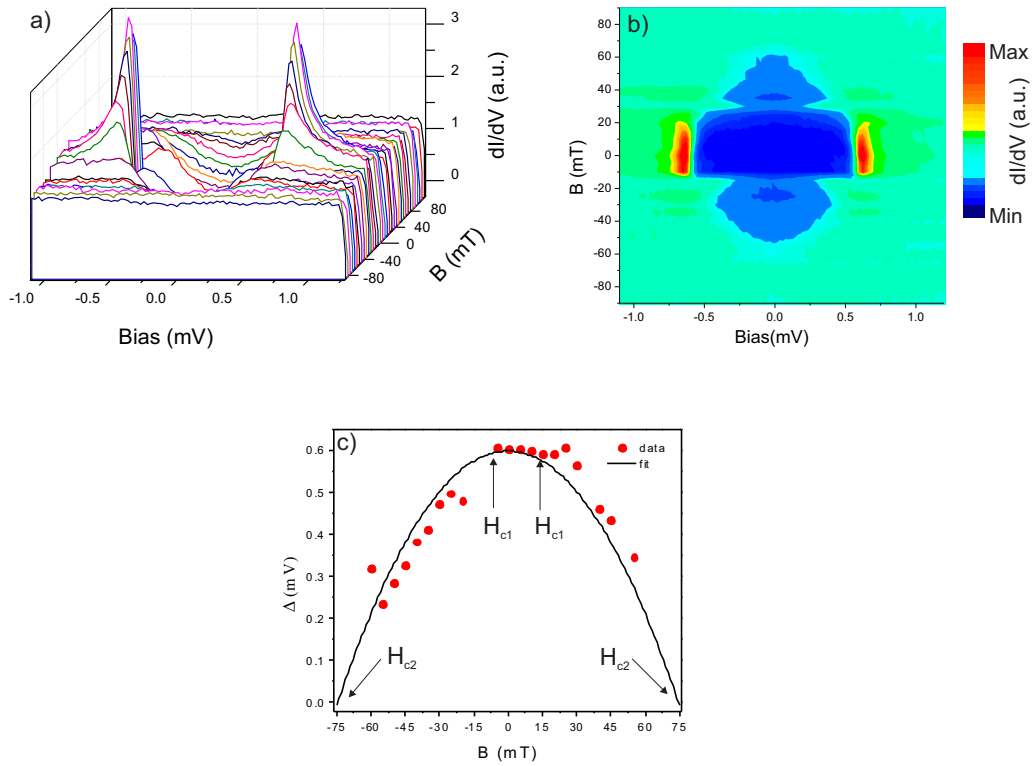


FIGURE 8.6: (a) Conductance spectra taken as a function of magnetic field applied parallel to the b axis. All spectra are taken at same position at base temperature. (b) The contour plot of the conductance spectra of as a function of magnetic field. (c) Gap size as a function of magnetic field, fitted with $\Delta(H) = \Delta(0)(1 - (H/H_{c2})^2)$ as described in the text.

The superconducting gap as a function of magnetic field is fitted with equation $\Delta(H) = \Delta(0)(1 - (H/H_c)^2)$ [161]. From the fitting we get the upper critical field value 74 mT, as shown in Fig. 8.6c. The value is on the same order of magnitude as the value measured from transport and SQUID (40 mT) shown in Fig. 8.2c. From the graph we can see that some data points deviate from the fitting. This is because when we increase magnetic field, occasionally magnetic vortex core move into the regions where the spectra are taken indicating that H_{c1} is about 15 mT. If we assume the vortex lattice is close packed, from the upper critical field $H_{c2} = \Phi_0/2\pi\xi_0^2$, we can get the coherence length ξ_0 about 65 nm.

Furthermore, a conductance map has been taken in the vicinity of step edges at base temperature with a finite magnetic field (about 10 mT). The topography can be seen in Fig. 8.7a, in which four different planes can be seen (A-D). The topography covers an area of $150 \times 150 \text{ nm}^2$. The line profile across the step edges is shown in Fig. 8.7b. The height difference between each of the terraces is about 5 \AA . The average conductance spectra for different step edges are shown in Fig. 8.7c. These spectra were averaged from the full region in each of the planes (from A to D). As it can be seen the gaps are suppressed with respect to BCS limit, and there is a clear difference of the average spectra for different regions (especially regions A and C). In region 'C' the gap clearly resembles a V-shape unconventional SC gap, with a weaker coherence peaks. This difference in SC gap can be as a result of the residual magnetic field which forms a vortex core and thus suppresses the superconducting gap depending on the distance to the vortex core.

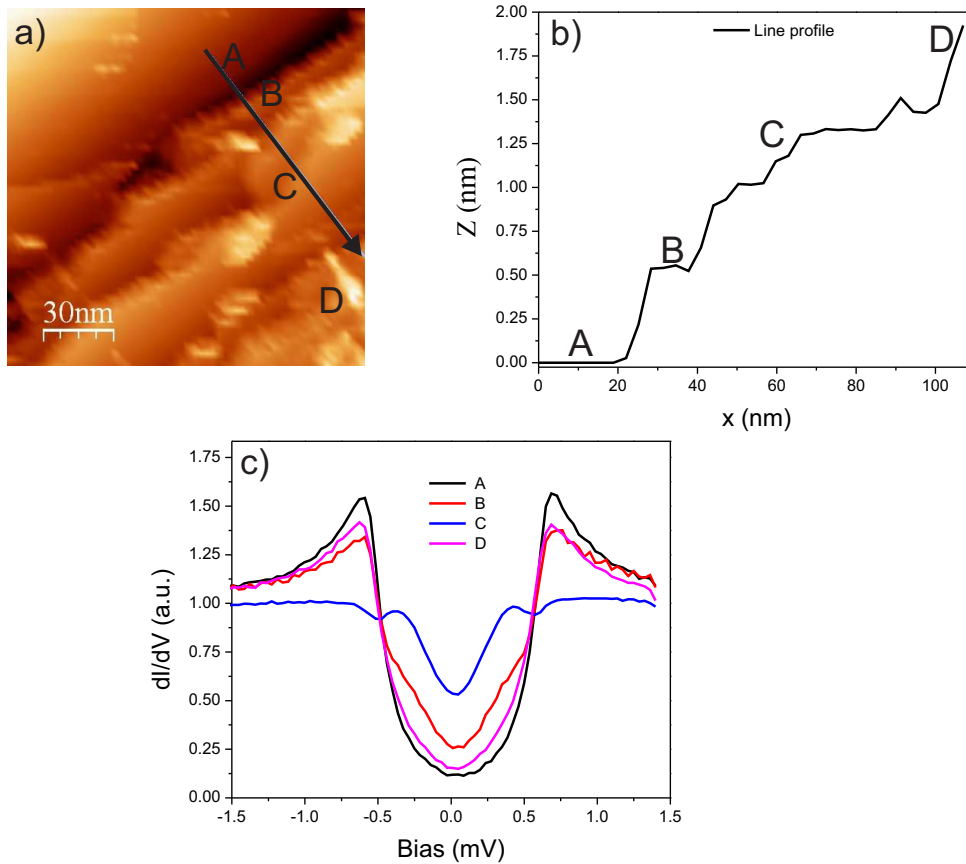


FIGURE 8.7: (a) Topography of plane with different step edges, the planes are indicated in the image from A to D. The area is $150 \times 150 \text{ nm}^2$. (b) The line profile of the line shown in (a); the different planes can be seen. (c) The average spectra on each of the planes.

8.2.2.5 Vortex core

Since α -BiPd is a type II superconductor, it can host magnetic vortices when we ramp the field $15 \text{ mT} < H < 60 \text{ mT}$. By taking a spectroscopic map in an area of $100 \times 100 \text{ nm}^2$ which was between step edges (topography shown in Fig. 8.8a), we have observed a vortex core from the ZBTC spatial map shown in Fig. 8.8b, which reveals a clear, rather broad bound state at the Fermi level. As can be seen from the map and spectra taken as a function of distance from the vortex core (Fig. 8.8 (c) and (d) for parallel and perpendicular to the axis of the vortex), the bound state is localized within $\approx 60 \text{ nm}$. This characteristic length scale gives a measure for the coherence length ξ_0 , which is consistent with what we estimate from the upper critical field H_{c2} . The fact that the vortex was found near the step edge can indicate that it had been pinned to it.

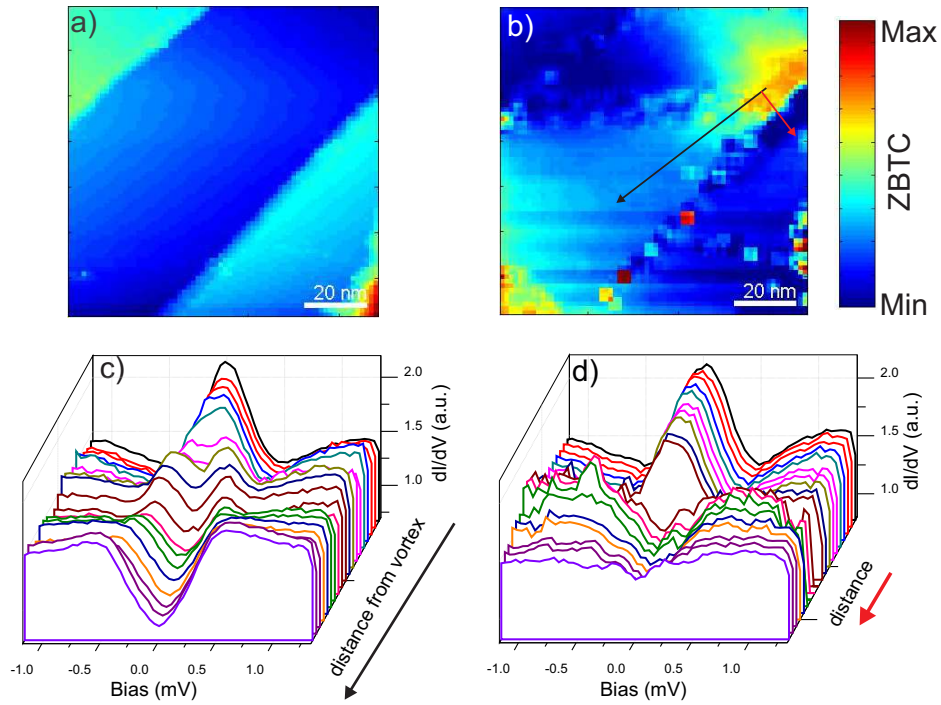


FIGURE 8.8: Single magnetic vortex core. (a) The topography of the surface where the vortex has been observed, the step edges can be seen. (b) The zero energy conductance of the vortex core in an area of $100 \times 100 \text{ nm}^2$. The vortex locates at the up right corner of the map. (c) The conductance spectrum line profile across the vortex core. Spectra are taken following the black line in (b). The bound state in the vortex core can be seen. (d) The conductance spectrum line profile perpendicular to the axis of the vortex. Spectra are taken following the red line in (b).

The bound state in the vortex core can be attributed Caroli-de Gennes-Matricon (CdGM) bound states [162] which can be explained due to Andreev reflection, where there is an interface between the normal (N) (vortex) state and the superconducting (S) state. In that case when the electron (hole) tunnels from the vortex (N) to the (S), it forms a Cooper pair in the (S) with the retroreflection of a hole (electron) of opposite spin and

momentum to the incident electron (hole). The quasiparticles with same spins interfere constructively, and a peak in the DOS will be observed. To distinguish potential zero-energy Majorana modes from ordinary CdGM states with finite energy, a resolution on the order of $\Delta^2/E_F \sim 0.1\mu\text{eV} \approx 1\text{ mK}$ is required, which is beyond the resolution of any STM up to now.

8.2.2.6 Measurements with superconducting tips

As it has already been discussed in chapter 4, Josephson junction can be studied when Cooper pairs tunnel between two superconductors. During our measurements on BiPd, the tip was coated with BiPd and transformed to a superconductor. However, we observed two different superconducting tips, presumably depending on the size of the cluster of BiPd which coated the tip. In Fig. 8.9a the comparison between the two different superconducting tips and the normal tip can be seen. All the three spectra were taken with the same set points ($V_b=10\text{ mV}$, $I=2\text{ nA}$) which results in junction resistance of $R_N = 5M\Omega$. In the case of superconducting tip1 (black line), the gap size doubles with respect to the normal tip (red points), i.e. $\Delta_{tip1} = \Delta_{sample}$, therefore $\Delta_{tip1} + \Delta_{sample} = 2\Delta_{sample}$. On the other hand, for the case of superconducting tip2 (blue line), we observe formation of two distinct gaps.

This can be explained when $\Delta_{tip2} \neq \Delta_{sample}$ and as a result we see subharmonic gap structures (SGS), originating from multiple Andreev reflections (MAR). The SGS have been observed in junctions between superconductors as conductance peaks appearing at bias voltages $V = (\Delta_{tip2} + \Delta_{sample})/n$ with $n = 1, 2, 3, \dots$ [163]. $\Delta_{tip2} + \Delta_{sample} = 1\text{ mV}$, Δ_{tip2} , Δ_{sample} . Since the gap values (Δ_{tip2} and Δ_{sample}) are close to each other, what we observe is $0.5(\Delta_{tip2} + \Delta_{sample})$. Hence, the value of $\Delta_{tip2} \approx 0.4\text{ mV}$, where $\Delta_{sample} = 0.6\text{ mV}$. The coherence peak with tip1 is very sharp and clear and much higher than what is expected in an N-S junction with a normal tip, which is what we expect from a superconducting tip. However, the coherence peaks in tip2 does not rise higher than the normal tip, which might be because of the structure of the tip and how it couples to the sample, which reduces quasiparticle tunneling.

This observation with two gaps is consistent with the already observed double gap in the point contact measurement [153], however they have seen different values of gap for different crystal axes.

With superconducting tip1 (black line), magnetic field dependence measurements were conducted to observe the changes of the superconducting gap of the tip1. The spectra are shown in Fig. 8.9b, and as it can be seen the upper critical field is larger than 1.5T. This has already been observed with Al tip in chapter 3, that if the tip apex is

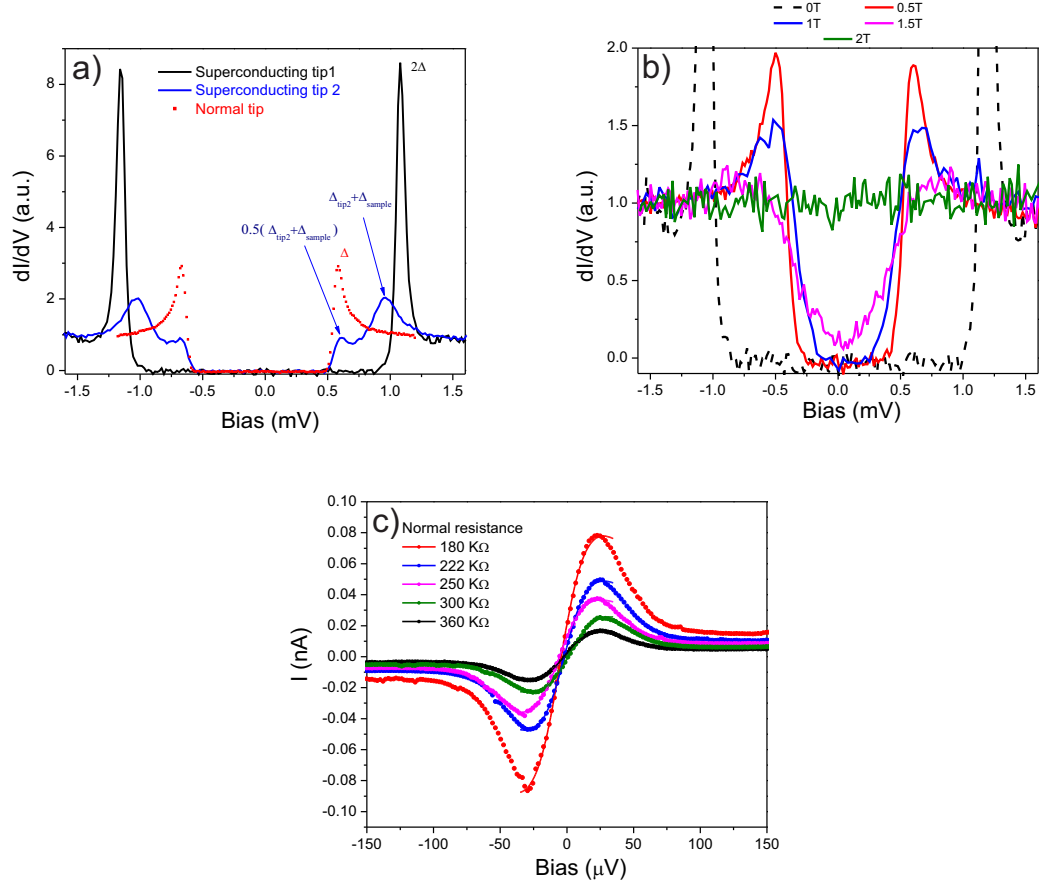


FIGURE 8.9: (a) The superconducting gap with two different superconducting tips. All three spectra were taken with same setpoints. $V_b=10$ mV, $I=2$ nA ; $R_N = 5M\Omega$. All data have been taken at 20 mK. (b) The superconducting gap with tip1 as function of magnetic field. (c) Data (obtained with tip2) and fits of the supercurrent with phase diffusion model for different resistances. The fitting range is from dip to peak.

smaller than the coherence length, the superconductivity can survive magnetic fields higher than the critical field of the bulk material. This can explain one reason why previous measurements have shown higher upper critical field (0.8 T) which might be due to the size of the crystal which had been used for their measurements (if they have measured a really tiny piece).

In order to measure the supercurrent, we have carried measurements with tip2 by applying low tunneling resistance (in the range of few $\text{K}\Omega$). In Fig. 8.9c the data and the fit with phase diffusion model already discussed in chapter 3 can be seen. From the fits we have derived $T_J = 2.29 \pm 0.217$ K, and $R_{\text{mean}} = 322 \pm 42\Omega$. Furthermore, unlike Al- Josephson (in chapter 3) we observe no resonances (shoulders) in the spectra. The Josephson tunneling is more complicated than the quasi-particle tunneling since it is dependent on the electromagnetic environment of the circuit, on the surface roughness and the tip and therefore for different measurements (meaning different tips and different samples), distinct T_J will be expected.

8.3 Summary and Discussion

Our results give a picture of the superconductivity in α -BiPd well consistent with the expectations for a standard type-II BCS superconductor with a single s -wave order parameter with negligible admixture of spin-triplet pairing. This is consistent with the nuclear quadrupolar resonance (NQR) measurements [160], which also show single gap behavior though with a slightly smaller gap size than what we find. Our results are in disagreement with the conclusions acquired by point-contact spectroscopy measurements [153], where zero-bias anomalies were observed and interpreted as a signature of unconventional superconductivity. In order to reconcile these two opposing findings, the impurity effects and the structure and form of the point-contact need to be taken into consideration. It is also probable that the point-contact measurements probe in-gap states at crystal faces different from the (010) surface, which are not accessible in our STM measurements. Furthermore, the differences concerning the upper critical field H_{C2} from the point-contact spectroscopy measurements (between ~ 0.8 T [153, 159] and 60 mT) can be explained due to the difference in the size of the cluster of crystal being measured, as we have observed upper critical fields of up to 1.5 T with cluster of BiPd coating the apex (Fig. 8.9b). Squid measurements confirmed the 60 mT upper critical field. Moreover, a vortex has been imaged by the spectroscopic map at zero bias by applying a magnetic field of ~ 20 mT. The spectra showed a peak (bound state), due to the Andreev reflection. Finally, with a superconducting tip (BiPd coated on the tip), Josephson supercurrent between BiPd-BiPd junction has been measured. The measurements indicated a difference to the Al-Al junction, due to the difference of tips, electromagnetic environment, sample roughness. As an outlook, studying the spin-orbit coupling effect can be performed. Due to the large atomic spin-orbit interaction of the heavy element Bi results in a Rashba-like spin splitting of the bulk bands. Scanning tunneling spectroscopy measurements can reveal density of states at the (010) surface of BiPd single crystal, which can be compared with band structure calculations as well as ARPES measurements.

Chapter 9

Conclusion and summary

Studying superconductors which belong to the family of strongly correlated electron materials is a promising approach for expanding the understanding in the field of superconductivity; however, the electrons in these materials have dual local and itinerant behavior, which makes its experimental investigation challenging. SI-STM is an ideal tool to detect the electronic excitations in real and reciprocal space.

In this work, I have used SI-STM to investigate strongly correlated electron materials. Initially, prior to performing the presented experiments, I assisted to construct and setup a new STM operating at milli Kelvin temperatures, which has been optimized for spectroscopic imaging functionality [17]. The STM scan head made of sapphire, is anchored to the lowest part of a dilution refrigerator, with continuous circulation of ^3He - ^4He mixture. The measurements can be performed at a base temperature of ~ 10 mK, and in magnetic fields of up to 14T.

Once the new instrument was successfully tested, first measurements were taken on NbSe₂ and Aluminum; the former to image the atomic resolution topography in order to calibrate the piezo scanner and the latter to determine the energy resolution by fitting the superconducting gap of Al with the BCS function accounting thermal broadening. Consequently, with an Al coated tip on an Al sample I measured the Josephson supercurrent, from which it is possible to determine the Josephson temperature, circuit resistance, capacitance and inductance. The supercurrent has been fitted with various models, and all of them were consistent. Josephson supercurrent is strongly affected by the size of the tip, electromagnetic environment of the tip and sample, roughness of the surface, etc. As an outlook, it would be intriguing to measure the Josephson supercurrent to determine the superconducting order parameter (SOP) of the sample, if that of the tip is known, since it enables phase sensitive measurements.

Furthermore, SI-STM studies were conducted on several correlated electron materials, the results of which are described in the body of this thesis.

Magnetic order in strongly correlated electron materials is usually acquired by neutron scattering, where magnetic scattering peaks shows up. Real space imaging of magnetic order is possible with spin-polarized scanning tunneling microscopy (SP-STM), which has been used extensively to study magnetic properties of thin films, nanostructures and magnetic clusters [105]. Despite its potential, especially for imaging the transition from the magnetically ordered parent compound to the superconducting state, characterization of atomic scale magnetic structure in strongly correlated electron materials and, in particular, materials relevant for high temperature superconductivity has not been achieved so far by SP-STM. Due to the layered structure of Fe_{1+y}Te , electronic properties and magnetism are quasi two-dimensional [164], making it ideally suited for a study by SP-STM. The results by imaging the topography with SP-tip, indicate a transition from unidirectional stripes in the monoclinic phase to bidirectional stripes in the orthorhombic phase by increasing the excess iron concentration. Magnetic and temperature dependent measurements verified the nature of the stripes to be originated from the spin structure.

The observation of magnetic structures on the atomic scale in parent compounds of high temperature superconductors brings the possibility to obtain real space images of stripe order in cuprates [165, 166] and search for magnetic order accompanying the spatially modulated electronic states found in the pseudogap phase [167, 168].

Moreover, the spectroscopic measurements on the first discovered heavy fermion superconductor, CeCu_2Si_2 , showed that the superconducting gap does not open fully; however the temperature and magnetic field dependent measurements showed that the gap vanishes as it reaches T_c and H_{c2} respectively. The vortex lattice of this compound has been mapped for the first time, where other techniques like magnetic neutron scattering have not yet reported any data for this compound, making the observation unique for STM. The vortex lattice of CeCoIn_5 , another heavy fermion superconductor, has been extensively studied by neutron scattering and has proven to have a rich and complex vortex lattice phase diagram as the temperature and magnetic field are tuned [139]. However, our observations show that the vortices form a triangular lattice structure at different fields at the base temperature. Technically, measurements of the vortex lattice on CeCu_2Si_2 is more challenging than CeCoIn_5 due to its lower superconducting transition temperature and critical field. From imaging a single vortex, it is possible to determine the coherence length of the superconductor. From the anisotropy of the vortex lattice the symmetry of the order parameter can be studied.

Afterwards, another heavy fermion compound with an intriguing magnetic phase diagram at low temperatures, CeB_6 , has been measured. Measurements on an atomically flat surface on the (1 0 0) orientation have been performed, and spectroscopic measurements as a function of temperature and magnetic field have been carried out. The thermal evolutions are fitted with the Fano function, where a resonance width on the order of 41.6 ± 14.9 mV has been derived. Finally, the field dependence data showed that a gap with the size of ± 4 mV vanishing as the field increases, since there is a transition of the magnetic phase. As an outlook, measuring the field dependence with a vector magnet (applying field in different directions) would be interesting due to the complex phase diagram of this compound.

Finally, the first atomic resolution STM measurement on the non-centrosymmetric superconductor BiPd has been performed. The motivation which led us to study this compound was the possibility to detect p-wave superconducting pair. Furthermore, since the zero energy Majorana states appear inside the vortex core of chiral p-wave superconductors, we were interested in measuring the bound state inside a vortex core. Additionally, due to the large spin-orbit interaction of the heavy element Bi, topologically protected surface states can be predicted, which could have technological applications in the future. All these potential possibilities make BiPd an exciting compound to study.

Our results showed that the superconducting gap on most of the surfaces shows a clear s-wave order parameter and the p-wave component is negligible. This suggests that the superconductivity is driven by phonons and the magnetically mediated coupling is not sufficiently strong to affect the pairing. The bound state in the vortex core showed a broad peak, which can be attributed to Andreev reflections (CdGM states [162]). With resolutions of about 1mK it should be possible to detect the splitting of the peaks near the Fermi energy. For a Majorana state in the vortex core a narrow peak at zero energy is expected, which is in contrast with the result. Eventually, with a superconducting tip (BiPd coated on the tip), Josephson supercurrent between BiPd-BiPd junction has been measured. The measurements indicated a difference to the Al-Al junction, due to the difference of tips, electromagnetic environment and sample roughness.

These findings may assist to broaden the understanding of the connection between magnetism and superconductivity in correlated electron materials, and also elucidate the mechanism of superconductivity in these materials.

Bibliography

- [1] J. George Bednorz and K. Alex Müller. Possible high T_c superconductivity in the Ba- La- Cu- O system. *Zeitschrift für Physik B Condensed Matter*, 64(2):189–193, 1986.
- [2] Y. Kamihara, H. Hiramatsu, M. Hirano, R. Kawamura, H. Yanagi, T. Kamiya, and H. Hosono. Iron-based layered superconductor: LaOFeP. *Journal of the American Chemical Society*, 128(31):10012–10013, 2006.
- [3] G. Wu, Y.L. Xie, H. Chen, M. Zhong, R.H. Liu, B.C. Shi, Q.J. Li, X.F. Wang, T. Wu, Y.J. Yan, et al. Superconductivity at 56K in samarium-doped SrFeAsF. *Journal of Physics: Condensed Matter*, 21(14):142203, 2009.
- [4] Michael R. Norman. The challenge of unconventional superconductivity. *Science*, 332(6026):196–200, 2011.
- [5] K. Andres, J.E. Graebner, and H.R. Ott. $4f$ -virtual-bound-state formation in CeAl₃ at low temperatures. *Phys. Rev. Lett.*, 35:1779–1782, 1975.
- [6] Ff. Steglich, J. Aarts, C.D. Bredl, W. Lieke, D. Meschede, W. Franz, and H. Schäfer. Superconductivity in the presence of strong pauli paramagnetism: CeCu₂Si₂. *Physical Review Letters*, 43(25):1892–1896, 1979.
- [7] Elbio Dagotto. Complexity in strongly correlated electronic systems. *Science*, 309(5732):257–262, 2005.
- [8] Fa Wang and Dung-Hai Lee. The electron-pairing mechanism of iron-based superconductors. *Science*, 332(6026):200–204, 2011.
- [9] G.R. Stewart. Heavy-fermion systems. *Reviews of Modern Physics*, 56(4):755, 1984.
- [10] Andrew J. Schofield. Condensed-matter physics: The emergent and hidden unveiled. *Nature*, 465(7298):553–554, 2010.
- [11] Piers Coleman. Condensed-matter physics: Microscopy of the macroscopic. *Nature*, 474(7351):290–291, 2011.

- [12] Øystein Fischer, Martin Kugler, Ivan Maggio-Aprile, Christophe Berthod, and Christoph Renner. Scanning tunneling spectroscopy of high-temperature superconductors. *Reviews of Modern Physics*, 79(1):353, 2007.
- [13] Jinho Lee, M.P. Allan, M.A. Wang, J. Farrell, S.A. Grigera, F. Baumberger, J.C. Davis, and A.P. Mackenzie. Heavy d-electron quasiparticle interference and real-space electronic structure of $\text{Sr}_3\text{Ru}_2\text{O}_7$. *Nature Physics*, 5(11):800–804, 2009.
- [14] T. Hanaguri, S. Niitaka, K. Kuroki, and H. Takagi. Unconventional s-wave superconductivity in Fe (Se, Te). *Science*, 328(5977):474–476, 2010.
- [15] John Singleton and Charles Mielke. Quasi-two-dimensional organic superconductors: a review. *Contemporary Physics*, 43(2):63–96, 2002.
- [16] Xiao-Liang Qi and Shou-Cheng Zhang. Topological insulators and superconductors. *Reviews of Modern Physics*, 83(4):1057, 2011.
- [17] U.R. Singh, M. Enayat, S.C. White, and P. Wahl. Construction and performance of a dilution-refrigerator based spectroscopic-imaging scanning tunneling microscope. *Rev. Sci. Instr.*, 84:013708, 2013.
- [18] C Julian Chen. *Introduction to scanning tunneling microscopy*, volume 227. Oxford University Press New York, 1993.
- [19] Eric Hudson. *Investigating High-TC Superconductivity on the Atomic Scale by Scanning Tunneling Microscopy*. PhD dissertation, University of California, Berkeley, 1999.
- [20] Jennifer Eve Hoffman. *A Search for Alternative Electronic Order in the High Temperature Superconductor $\text{Bi}_2\text{Sr}_2\text{CaCu}_2\text{O}_{8+\delta}$ by Scanning Tunneling Microscopy*. PhD dissertation, University of California, Berkeley, 2003.
- [21] Maximilian Assig. *Development of a Millikelvin Scanning Tunneling Microscope for Applications in Ultra High Vacuum and High Magnetic Fields*. PhD dissertation, EPFL, 2011.
- [22] Antonio Barone, Gianfranco Paterno, and John Wiley. *Physics and applications of the Josephson effect*, volume 1. Wiley New York, 1982.
- [23] J. Bardeen. Tunneling from a many-particle point of view. *Phys. Rev. Lett.*, 6(57), 1961.
- [24] J. Tersoff and DR. Hamann. Theory and application for the scanning tunneling microscope. *Physical review letters*, 50(25):1998–2001, 1983.

- [25] J. Klein, A. Léger, M. Belin, D. Défourneau, and M.J.L. Sangster. Inelastic-electron-tunneling spectroscopy of metal-insulator-metal junctions. *Phys. Rev. B*, 7:2336–2348, Mar 1973.
- [26] L.J. Lauhon and W. Ho. Effects of temperature and other experimental variables on single molecule vibrational spectroscopy with the scanning tunneling microscope. *Review of Scientific Instruments*, 72(1):216–223, 2001.
- [27] R.C. Dynes, V. Narayanamurti, and J. Pm Garno. Direct measurement of quasiparticle-lifetime broadening in a strong-coupled superconductor. *Physical Review Letters*, 41(21):1509–1512, 1978.
- [28] H. London. *Proc. Int. Conf. Low Temperature Physics*, 157, 1951.
- [29] O. V. Lounasmaa. *Experimental principles and methods below 1K*. 1974.
- [30] F. Pobell. *F. Matter and Methods at Low Temperatures*. Springer 3rd ed., 2007.
- [31] S.H. Pan, E.W. Hudson, and J.C. Davis. ^3He refrigerator based very low temperature scanning tunneling microscope. *Review of scientific instruments*, 70(2):1459–1463, 1999.
- [32] M. Kugler, Ch. Renner, O. Fischer, V. Mikheev, and G. Batey. A ^3He refrigerated scanning tunneling microscope in high magnetic fields and ultrahigh vacuum. *Review of Scientific Instruments*, 71(3):1475–1478, 2000.
- [33] Christian Debuschewitz, Frank Münstermann, Vojko Kunej, and Elke Scheer. A compact and versatile scanning tunnelling microscope with high energy resolution for use in a ^3He cryostat. *Journal of Low Temperature Physics*, 147(3-4):525–535, 2007.
- [34] J.G. Rodrigo, H. Suderow, and S. Vieira. On the use of STM superconducting tips at very low temperatures. *The European Physical Journal B-Condensed Matter and Complex Systems*, 40(4):483–488, 2004.
- [35] N. Moussy, H. Courtois, and B. Pannetier. A very low temperature scanning tunneling microscope for the local spectroscopy of mesoscopic structures. *Review of Scientific Instruments*, 72(1):128–131, 2001.
- [36] M. Marz, G. Goll, and Hv Lohneysen. A scanning tunneling microscope for a dilution refrigerator. *Review of Scientific Instruments*, 81(4):045102, 2010.
- [37] Hélène Le Sueur and Philippe Joyez. Room-temperature tunnel current amplifier and experimental setup for high resolution electronic spectroscopy in millikelvin scanning tunneling microscope experiments. *Review of scientific instruments*, 77(12):123701, 2006.

- [38] H. Kambara, T. Matsui, Y. Niimi, and Hiroshi Fukuyama. Construction of a versatile ultralow temperature scanning tunneling microscope. *Review of Scientific Instruments*, 78(7):073703, 2007.
- [39] Young Jae Song, Alexander F Otte, Vladimir Shvarts, Zuyu Zhao, Young Kuk, Steven R Blankenship, Alan Band, Frank M Hess, and Joseph A Stroscio. Invited review article: A 10 mK scanning probe microscopy facility. *Review of Scientific Instruments*, 81(12):121101, 2010.
- [40] Maximilian Assig, Markus Etzkorn, Axel Enders, Wolfgang Stiepany, Christian R Ast, and Klaus Kern. A 10 mK scanning tunneling microscope operating in ultra high vacuum and high magnetic fields. *Review of Scientific Instruments*, 84(3):033903, 2013.
- [41] Modified kelvinox 400MX by oxford instruments. Technical report.
- [42] Chr. Wittneven, R. Dombrowski, S.H. Pan, and R. Wiesendanger. A low-temperature ultrahigh-vacuum scanning tunneling microscope with rotatable magnetic field. *Review of scientific instruments*, 68(10):3806–3810, 1997.
- [43] S. h. pan, piezoelectric motor, international patent publication no. wo 93/19494. Technical report.
- [44] S.C. White, U.R. Singh, and P. Wahl. A stiff scanning tunneling microscopy head for measurement at low temperatures and in high magnetic fields. *Review of Scientific Instruments*, 82(11):113708–113708, 2011.
- [45] Piezo actuators (model p-121.03). Technical report.
- [46] According to calculations by Oxford Instruments for the magnet.
- [47] Passive dampers (model i-2000). Technical report.
- [48] Rf filters (model 1221-001). Technical report.
- [49] RuO₂ temperature sensors. Technical report.
- [50] Soft db inc. Technical report.
- [51] Percy Zahl, Markus Bierkandt, Stefan Schroder, and Andreas Klust. The flexible and modern open source scanning probe microscopy software package GXSM. *Review of scientific instruments*, 74(3):1222–1227, 2003.
- [52] Percy Zahl, Thorsten Wagner, Rolf Möller, and Andreas Klust. Open source scanning probe microscopy control software package GXSM. *Journal of Vacuum Science & Technology B: Microelectronics and Nanometer Structures*, 28:C4E39, 2010.

- [53] Femto GmbH (model dlpca-200). Technical report.
- [54] The calibration of the z -piezo has been obtained from the height of occasionally seen step edges on different types of single crystals.
- [55] B. Giambattista, A. Johnson, R.V. Coleman, B. Drake, and P.K. Hansma. Charge-density waves observed at 4.2 K by scanning-tunneling microscopy. In *Scanning Tunneling Microscopy*, pages 234–237. Springer, 1993.
- [56] I. Guillamon, H. Suderow, S. Vieira, L. Cario, P. Diener, and P. Rodiere. Superconducting density of states and vortex cores of 2H-NbS₂. *Physical review letters*, 101(16):166407, 2008.
- [57] Au(111) crystal. Technical report.
- [58] J. Klein, A. Leger, M. Belin, D. Défourneau, and M.J.L. Sangster. Inelastic-electron-tunneling spectroscopy of metal-insulator-metal junctions. *Physical Review B*, 7(6):2336, 1973.
- [59] A.K. Gupta, L. Créton, N. Moussy, B. Pannetier, and H. Courtois. Anomalous density of states in a metallic film in proximity with a superconductor. *Physical Review B*, 69(10):104514, 2004.
- [60] M. Poza, E. Bascones, J. G. Rodrigo, N. Agra, S. Vieira, and F. Guinea. Nano-sized superconducting constrictions. *Phys. Rev. B*, 58:11173–11176, Nov 1998. doi: 10.1103/PhysRevB.58.11173.
- [61] Brian David Josephson. Possible new effects in superconductive tunnelling. *Physics Letters*, 1(7):251–253, 1962.
- [62] Jurij Šmakov, Ivar Martin, and Alexander V Balatsky. Josephson scanning tunneling microscopy. *Physical Review B*, 64(21):212506, 2001.
- [63] Silvia Corlevi. *Quantum effects in nanoscale Josephson junction circuits*. PhD dissertation, Kungliga Tekniska Hgskolan, Roslagstullsbacken 21 SE-106 91 Stockholm, 2006.
- [64] Vinay Ambegaokar and Alexis Baratoff. Tunneling between superconductors. *Phys. Rev. Letters*, 10, 1963.
- [65] O. Naaman, W. Teizer, and R.C. Dynes. Fluctuation dominated josephson tunneling with a scanning tunneling microscope. *Physical review letters*, 87(9):097004, 2001.

- [66] Hikari Kimura, R.P. Barber Jr., Shimpei Ono, Yoichi Ando, and Robert C. Dynes. Scanning josephson tunneling microscopy of single-crystal $\text{Bi}_2\text{Sr}_2\text{CaCu}_2\text{O}_{8+\delta}$ with a conventional superconducting tip. *Physical review letters*, 101(3):037002, 2008.
- [67] Hikari Kimura, R.P. Barber Jr., S. Ono, Yoichi Ando, and R.C. Dynes. Josephson scanning tunneling microscopy: A local and direct probe of the superconducting order parameter. *Physical Review B*, 80(14):144506, 2009.
- [68] Markus Ternes, Wolf-Dieter Schneider, Juan-Carlos Cuevas, Christopher P. Lutz, Cyrus F. Hirjibehedin, and Andreas J. Heinrich. Subgap structure in asymmetric superconducting tunnel junctions. *Physical Review B*, 74(13):132501, 2006.
- [69] J.G. Rodrigo, V. Crespo, and S. Vieira. Josephson current at atomic scale: Tunneling and nanocontacts using a STM. *Physica C: Superconductivity*, 437:270–273, 2006.
- [70] Yu.M.Ivanchenko and L.A.Zil'berman. The josephson effect in small tunnel contacts. *Soviet Physics JETP*, 28(6):1272, 1969.
- [71] Gert-Ludwig Ingold, Hermann Grabert, and Udo Eberhardt. Cooper-pair current through ultrasmall josephson junctions. *Physical Review B*, 50(1):395, 1994.
- [72] Gert-Ludwig Ingold and Yu V. Nazarov. Charge tunneling rates in ultrasmall junctions. *Single Charge Tunneling*, 294, 2005.
- [73] G-L Ingold and Hermann Grabert. Finite-temperature current-voltage characteristics of ultrasmall tunnel junctions. *EPL (Europhysics Letters)*, 14(4):371, 1991.
- [74] Y. Mizuguchi and Y. Takano. Review of Fe chalcogenides as the simplest Fe-based superconductor. *J. Phys. Soc. Jap.*, 79(10):2001, 2010.
- [75] Cevriye Koz, Sahana Rößler, Alexander A Tsirlin, Steffen Wirth, and Ulrich Schwarz. Low-temperature phase diagram of Fe_{1+y}Te studied using x-ray diffraction. *Physical Review B*, 88(9):094509, 2013.
- [76] D. Fruchart, P. Convert, P. Wolfers, R. Madar, J.P. Senateur, and R. Fruchart. Structure antiferromagnetique de $\text{Fe}_{1.125}\text{Te}$ accompagnée d'une deformation monoclinique. *Mat. Res. Bull.*, 10:169–174, 1975.
- [77] A. Martinelli, A. Palenzona, M. Tropeano, C. Ferdeghini, M. Putti, M.R. Cimberle, T.D. Nguyen, M. Affronte, and C. Ritter. From antiferromagnetism to superconductivity in $\text{Fe}_{1+y}\text{Te}_{1-x}\text{Se}_x$: Neutron powder diffraction analysis. *Phys. Rev. B*, 81(9):094115, 2010.

- [78] S. Rößler, D. Cherian, W. Lorenz, M. Doerr, C. Koz, C. Curfs, Y. Prots, UK Rößler, U. Schwarz, S. Elizabeth, et al. First-order structural transition in the magnetically ordered phase of $\text{Fe}_{1.13}\text{Te}$. *Phys. Rev. B*, 84(17):174506, 2011.
- [79] Shiliang Li, Clarina de la Cruz, Q. Huang, Y. Chen, J. W. Lynn, Jiangping Hu, Yi-Lin Huang, Fong-Chi Hsu, Kuo-Wei Yeh, Maw-Kuen Wu, and Pengcheng Dai. First-order magnetic and structural phase transitions in $\text{Fe}_{1+y}\text{Se}_x\text{Te}_{1-x}$. *Phys. Rev. B*, 79:054503, Feb 2009.
- [80] Wei Bao, Y. Qiu, Q. Huang, M.A. Green, P. Zajdel, M.R. Fitzsimmons, M. Zherrenkov, S. Chang, Minghu Fang, B. Qian, et al. Tunable $(\delta\pi, \delta\pi)$ -type antiferromagnetic order in α -Fe(Te,Se) superconductors. *Phys. Rev. Lett.*, 102(24):247001, 2009.
- [81] F. Ma, W. Ji, J. Hu, Z.Y. Lu, and T. Xiang. First-principles calculations of the electronic structure of tetragonal α -FeTe and α -FeSe crystals: evidence for a bicollinear antiferromagnetic order. *Phys. Rev. Lett.*, 102(17):177003, 2009.
- [82] A.M. Turner, F. Wang, and A. Vishwanath. Kinetic magnetism and orbital order in iron telluride. *Phys. Rev. B*, 80(22):224504, 2009.
- [83] I.A. Zaliznyak, Z. Xu, J.M. Tranquada, G. Gu, A.M. Tsvelik, and M.B. Stone. Unconventional temperature enhanced magnetism in $\text{Fe}_{1.1}\text{Te}$. *Phys. Rev. Lett.*, 107(21):216403, 2011.
- [84] S. Ducatman, N.B. Perkins, and A. Chubukov. Magnetism in parent Fe-chalcogenides: quantum fluctuations select a plaquette order. *Phys. Rev. Lett.*, 109:157206, 2012.
- [85] A. Subedi, L. Zhang, D.J. Singh, and M.H. Du. Density functional study of FeS, FeSe, and FeTe: Electronic structure, magnetism, phonons, and superconductivity. *Phys. Rev. B*, 78(13):134514, 2008.
- [86] G.F. Chen, Z.G. Chen, J. Dong, W.Z. Hu, G. Li, X.D. Zhang, P. Zheng, J.L. Luo, and N.L. Wang. Electronic properties of single-crystalline $\text{Fe}_{1.05}\text{Te}$ and $\text{Fe}_{1.03}\text{Se}_{0.30}\text{Te}_{0.70}$. *Phys. Rev. B*, 79(14):140509, 2009.
- [87] C. Fang, B. Andrei Bernevig, and J. Hu. Theory of magnetic order in $\text{Fe}_{1+y}\text{Se}_x\text{Te}_{1-x}$. *Europhys. Lett.*, 86:67005, 2009.
- [88] I.A. Zaliznyak, Z.J. Xu, J.S. Wen, J.M. Tranquada, G.D. Gu, V. Solovyov, V.N. Glazkov, A.I. Zheludev, V.O. Garlea, and M.B. Stone. Continuous magnetic and structural phase transitions in Fe_{1+y}Te . *arXiv:1108.5968*.
- [89] M.-C. Ding, H.-Q. Lin, and Y.-Z. Zhang. *arxiv:1303.4072*.

- [90] Y. Liu and C.T. Lin. *J. Supercond. Nov. Magn.*, 24:183, 2011.
- [91] X.B. He, G.R. Li, J.D. Zhang, A.B. Karki, R.Y. Jin, B.C. Sales, A.S. Sefat, M.A. McGuire, D. Mandrus, and E.W. Plummer. Nanoscale chemical phase separation in $\text{FeTe}_{0.55}\text{Se}_{0.45}$ as seen via scanning tunneling spectroscopy. *Phys. Rev. B*, 83: 220502, 2011.
- [92] T. Machida, K. Kogure, T. Kato, H. Nakamura, H. Takeya, T. Mochiku, S. Ooi, Y. Mizuguchi, Y. Takano, K. Hirata, et al. Unidirectional electronic structure in the parent state of iron-chalcogenide superconductor $\text{Fe}_{1+\delta}\text{Te}$. *J. Phys. Soc. Jpn.*, 81(7):4714, 2012.
- [93] T. Machida, K. Kogure, T. Kato, H. Nakamura, H. Takeya, T. Mochiku, S. Ooi, Y. Mizuguchi, Y. Takano, K. Hirata, et al. Observation of an isosceles triangular electronic structure around the excess iron atoms in $\text{Fe}_{1+\delta}\text{Te}$. *Physical Review B*, 87(21):214508, 2013.
- [94] Andrei E. Ruckenstein, Peter J. Hirschfeld, and J. Appel. Mean-field theory of high- T_c superconductivity: The superexchange mechanism. *Physical Review B*, 36 (1):857, 1987.
- [95] Y. Xia, D. Qian, L. Wray, D. Hsieh, G.F. Chen, J.L. Luo, N.L. Wang, and M.Z. Hasan. Fermi surface topology and low-lying quasiparticle dynamics of parent $\text{Fe}_{1+x}\text{Te}/\text{Se}$ superconductor. *Phys. Rev. Lett.*, 103(3):37002, 2009.
- [96] C.Y. Moon and H.J. Choi. Chalcogen-height dependent magnetic interactions and magnetic order switching in $\text{FeSe}_x\text{Te}_{1-x}$. *Phys. Rev. Lett.*, 104(5):57003, 2010.
- [97] Efrain E Rodriguez, Chris Stock, Pawel Zajdel, Kathryn L Krycka, Charles F Majkrzak, Peter Zavalij, and Mark A Green. Magnetic-crystallographic phase diagram of the superconducting parent compound Fe_{1+x}Te . *Physical Review B*, 84(6):064403, 2011.
- [98] X. Liu, C.C. Lee, ZJ Xu, JS Wen, G. Gu, W. Ku, JM Tranquada, and JP Hill. X-ray diffuse scattering study of local distortions in Fe_{1+x}Te induced by excess Fe. *Phys. Rev. B*, 83(18):184523, 2011.
- [99] M.C. Boyer, K. Chatterjee, W.D. Wise, G.F. Chen, J.L. Luo, N.L. Wang, and E.W. Hudson. *arXiv:0806.4400*.
- [100] K. Koepf, S. Johnston, E. van Heumen, Y. Huang, J. Kaas, J.B. Goedkoop, M.S. Golden, and J. van den Brink. *Phys. Rev. Lett.*, 109:127001, 2012.
- [101] F. Masee, S. de Jong, Y. Huang, J. Kaas, E. van Heumen, J.B. Goedkoop, and M.S. Golden. *Phys. Rev. B*, 80:140507, 2009.

- [102] D. Hsieh, Y. Xia, L. Wray, D. Qian, K. Gomes, A. Yazdani, G.F. Chen, J.L. Luo, N.L. Wang, and M.Z. Hasan. *arXiv: 0812.2289*, 2008.
- [103] T.-M. Chuang, M.P. Allan, J. Lee, Y. Xie, N. Ni, S.L. Bud'ko, G.S. Boebinger, P.C. Canfield, and J.C. Davis. *Science*, 327:181–184, 2010.
- [104] A.V. Balatsky, D.N. Basov, and J.X. Zhu. Induction of charge density waves by spin density waves in iron-based superconductors. *Phys. Rev. B*, 82(14):144522, 2010.
- [105] R. Wiesendanger. Spin mapping at the nanoscale and atomic scale. *Rev. Mod. Phys.*, 81:1495–1550, (2009).
- [106] Brian B Zhou, Shashank Misra, Eduardo H da Silva Neto, Pegor Aynajian, Ryan E Baumbach, JD Thompson, Eric D Bauer, and Ali Yazdani. Visualizing nodal heavy fermion superconductivity in CeCoIn₅. *Nature Physics*, 2013.
- [107] Jun Kondo. Resistance minimum in dilute magnetic alloys. *Progress of theoretical physics*, 32(1):37–49, 1964.
- [108] Ana Isabel Maldonado Cid. *Superconducting vortex dynamics and new heavy fermion phases studied by very low temperature scanning tunneling spectroscopy*. PhD dissertation, Universidad Autónoma de Madrid, Spain, 2013.
- [109] Andrew R Schmidt, Mohammad H Hamidian, Peter Wahl, Focko Meier, Alexander V Balatsky, JD Garrett, Travis J Williams, Graeme M Luke, and JC Davis. Imaging the fano lattice to hidden order transition in URu₂Si₂. *Nature*, 465(7298): 570–576, 2010.
- [110] S Doniach. The kondo lattice and weak antiferromagnetism. *Physica B+ C*, 91: 231–234, 1977.
- [111] F. Steglich, J. Arndt, O. Stockert, S. Friedemann, M. Brando, C. Klingner, C. Krellner, C. Geibel, S. Wirth, S. Kirchner, et al. Magnetism, f-electron localization and superconductivity in 122-type heavy-fermion metals. *Journal of Physics: Condensed Matter*, 24(29):294201, 2012.
- [112] Melvin A Ruderman and Charles Kittel. Indirect exchange coupling of nuclear magnetic moments by conduction electrons. *Physical Review*, 96(1):99, 1954.
- [113] Kei Yosida. Magnetic properties of Cu-Mn alloys. *Physical Review*, 106(5):893, 1957.
- [114] Z. Fisk, H.R. Ott, T.M. Rice, and J.L. Smith. Heavy-electron metals. *Nature*, 320:124–129, 1986.

- [115] A. Schröder, G. Aeppli, R. Coldea, M. Adams, O. Stockert, Hv. Löhneysen, E. Bucher, R. Ramazashvili, and P. Coleman. Onset of antiferromagnetism in heavy-fermion metals. *Nature*, 407(6802):351–355, 2000.
- [116] K. Andres, J.E. Graebner, and H.R. Ott. 4f-virtual-bound-state formation in CeAl_3 at low temperatures. *Physical Review Letters*, 35:1779–1782, 1975.
- [117] J.E. Hoffman, K. McElroy, D-H Lee, K.M. Lang, H. Eisaki, S. Uchida, and J.C. Davis. Imaging quasiparticle interference in $\text{Bi}_2\text{Sr}_2\text{CaCu}_2\text{O}_{8+\delta}$. *Science*, 297(5584):1148–1151, 2002.
- [118] Jinho Lee, K. Fujita, K. McElroy, J.A. Slezak, M. Wang, Y. Aiura, H. Bando, M. Ishikado, T. Masui, J-X Zhu, et al. Interplay of electron–lattice interactions and superconductivity in $\text{Bi}_2\text{Sr}_2\text{CaCu}_2\text{O}_{8+\delta}$. *Nature*, 442(7102):546–550, 2006.
- [119] T. Hanaguri, S. Niitaka, K. Kuroki, and H. Takagi. Unconventional s-wave superconductivity in Fe (Se, Te). *Science*, 328(5977):474–476, 2010.
- [120] M.P. Allan, A.W. Rost, A.P. Mackenzie, Yang Xie, J.C. Davis, K. Kihou, C.H. Lee, A. Iyo, H. Eisaki, and T-M Chuang. Anisotropic energy gaps of iron-based superconductivity from intraband quasiparticle interference in LiFeAs . *Science*, 336(6081):563–567, 2012.
- [121] T. Hanaguri, K. Kitagawa, K. Matsubayashi, Y. Mazaki, Y. Uwatoko, and H. Takagi. Scanning tunneling microscopy/spectroscopy of vortices in LiFeAs . *Physical Review B*, 85(21):214505, 2012.
- [122] Pegor Aynajian, Eduardo H da Silva Neto, Colin V Parker, Yingkai Huang, Abhay Pasupathy, John Mydosh, and Ali Yazdani. Visualizing the formation of the kondo lattice and the hidden order in URu_2Si_2 . *Proceedings of the National Academy of Sciences*, 107(23):10383–10388, 2010.
- [123] Pegor Aynajian, Eduardo H. da Silva Neto, András Gyenis, Ryan E. Baumbach, J.D. Thompson, Zachary Fisk, Eric D. Bauer, and Ali Yazdani. Visualizing heavy fermions emerging in a quantum critical kondo lattice. *Nature*, 486(7402):201–206, 2012.
- [124] MP Allan, F Masee, DK Morr, J van Dyke, AW Rost, AP Mackenzie, C Petrovic, and JC Davis. Imaging cooper pairing of heavy fermions in CeCoIn_5 . *Nature Physics*, 2013.
- [125] Hideaki Sakata, Nobuhiko Nishida, Masato Hedo, Kenji Sakurai, Yoshihiko Inada, Yoshichika Onuki, Etsuji Yamamoto, and Yoshinori Haga. Vortex lattice

- and quasiparticle density of states in CeRu₂ studied by scanning tunneling spectroscopy. *Journal of the Physical Society of Japan*, 69(7):1970–1973, 2000.
- [126] Oliver Stockert, J. Arndt, E. Faulhaber, C. Geibel, H.S. Jeevan, S. Kirchner, M. Loewenhaupt, K. Schmalzl, W. Schmidt, Q. Si, et al. Magnetically driven superconductivity in CeCu₂Si₂. *Nature Physics*, 7(2):119–124, 2010.
- [127] F. Steglich, P. Gegenwart, C. Geibel, P. Hinze, M. Lang, C. Langhammer, G. Sparn, T. Tayama, O. Trovarelli, N.K. Sato, et al. Superconductivity and magnetism in heavy-fermions, 2001.
- [128] H.A. Vieyra, N. Oeschler, S. Seiro, H.S. Jeevan, C. Geibel, D. Parker, and F. Steglich. Determination of gap symmetry from angle-dependent h_{c2} measurements on CeCu₂Si₂. *Physical review letters*, 106(20):207001, 2011.
- [129] S. Seiro, M. Deppe, H. Jeevan, U. Burkhardt, and C. Geibel. Flux crystal growth of CeCu₂Si₂: Revealing the effect of composition. *physica status solidi (b)*, 247(3):614–616, 2010.
- [130] U. Fano. Effects of configuration interaction on intensities and phase shifts. *Phys. Rev.*, 124:1866–1878, Dec 1961.
- [131] Pegor Aynajian, Eduardo H da Silva Neto, András Gyenis, Ryan E Baumbach, JD Thompson, Zachary Fisk, Eric D Bauer, and Ali Yazdani. Visualizing heavy fermions emerging in a quantum critical kondo lattice. *Nature*, 486(7402):201–206, 2012.
- [132] G. Blatter, M.V. Feigel’Man, V.B. Geshkenbein, A.I. Larkin, and V.M. Vinokur. Vortices in high-temperature superconductors. *Reviews of Modern Physics*, 66(4):1125, 1994.
- [133] Ji-Hai Xu, Yong Ren, and Chin-Sen Ting. Structures of single vortex and vortex lattice in a d-wave superconductor. *Physical Review B*, 53(6):R2991–R2994, 1996.
- [134] M.R. Eskildsen, M. Kugler, S. Tanaka, J. Jun, S.M. Kazakov, J. Karpinski, and Ø Fischer. Vortex imaging in the π band of magnesium diboride. *Physical review letters*, 89(18):187003, 2002.
- [135] U. Rauchschwalbe, W. Lieke, C.D. Bredl, F. Steglich, J. Aarts, K.M. Martini, and A.C. Mota. Critical fields of the” heavy-fermion” superconductor CeCu₂Si₂. *Physical Review Letters*, 49(19):1448–1451, 1982.
- [136] T.A. Tokuyasu, D.W. Hess, and J.A. Sauls. Vortex states in an unconventional superconductor and the mixed phases of UPt₃. *Physical Review B*, 41(13):8891, 1990.

- [137] Ji-Hai Xu, Yong Ren, and Chin-Sen Ting. Structures of single vortex and vortex lattice in a d-wave superconductor. *Physical Review B*, 53(6):R2991, 1996.
- [138] M. Ichioka, N. Hayashi, N. Enomoto, and K. Machida. Vortex structure in d-wave superconductors. *Physical Review B*, 53(22):15316, 1996.
- [139] Andrea D Bianchi, Michel Kenzelmann, Lisa DeBeer-Schmitt, Jon S White, Edward M Forgan, Joel Mesot, Markus Zolliker, Joachim Kohlbrecher, Roman Movshovich, Eric D Bauer, et al. Superconducting vortices in CeCoIn₅: Toward the pauli-limiting field. *Science*, 319(5860):177–180, 2008.
- [140] M. Franz, I. Affleck, and M. H. S. Amin. Theory of equilibrium flux lattices in unconventional superconductors. *Phys. Rev. Lett.*, 79:1555–1558, 1997.
- [141] G. Aeppli and Z. Fisk. Kondo insulators. *Comments on Condensed Matter Physics*, 16:155–165, 1992.
- [142] V.P. Plakhty, L.P. Regnault, A.V. Goltsev, S.V. Gavrilov, F. Yakhou, J. Flouquet, C. Vettier, and S. Kunii. Itinerant magnetism in the Kondo crystal CeB₆ as indicated by polarized neutron scattering. *Physical Review B*, 71(10):100407, 2005.
- [143] A Takase, K Kojima, T Komatsubara, and T Kasuya. Electrical resistivity and magnetoresistance of CeB₆. *Solid State Communications*, 36(5):461–464, 1980.
- [144] P. Burllet, J. Rossat-Mignod, J.M. Effantin, T. Kasuya, S. Kunii, and T. Komatsubara. Magnetic ordering in cerium hexaboride CeB₆. *Journal of Applied Physics*, 53(3):2149–2151, 1982.
- [145] Masashi Takigawa, Hiroshi Yasuoka, Takaho Tanaka, and Yoshio Ishizawa. Nmr study on the spin structure of CeB₆. *Journal of the Physical Society of Japan*, 52(3):728–731, 1983.
- [146] S. Horn, F. Steglich, M. Loewenhaupt, H. Scheuer, W. Felsch, and K. Winzer. The magnetic behavior of CeB₆: Comparison between elastic and inelastic neutron scattering, initial susceptibility and high-field magnetization. *Zeitschrift für Physik B Condensed Matter*, 42(2):125–134, 1981.
- [147] G. Friemel, Yuan Li, A.V. Dukhnenko, N. Yu Shitsevalova, N.E. Sluchanko, A. Ivanov, V.B. Filipov, B. Keimer, and D.S. Inosov. Resonant magnetic excitation mode in the heavy-fermion antiferromagnet CeB₆. *Nature Communications*, 3:830, 2012.
- [148] Yu G. Naidyuk, M. Reiffers, A.G.M. Jansen, P. Wyder, and I.K. Yanson. Point-contact measurements of CeB₆ and CeCu₆ in high magnetic fields. *Zeitschrift für Physik B Condensed Matter*, 82(2):221–226, 1991.

- [149] E Paulus and G Voss. Point contact spectra of cerium compounds. *Journal of magnetism and magnetic materials*, 47:539–541, 1985.
- [150] B. Amsler, Z. Fisk, J.L. Sarrao, S. Von Molnar, M.W. Meisel, and F. Sharifi. Electron-tunneling studies of the hexaboride materials SmB_6 , EuB_6 , CeB_6 , and SrB_6 . *Physical Review B*, 57(15):8747, 1998.
- [151] Andrew Peter Mackenzie and Yoshiteru Maeno. The superconductivity of Sr_2RuO_4 and the physics of spin-triplet pairing. *Rev. Mod. Phys.*, 75:657–712, May 2003. doi: 10.1103/RevModPhys.75.657.
- [152] Ernst Bauer, Gerfried Hilscher, Herwig Michor, Ch Paul, E.W. Scheidt, A. Gribovanov, Yu Seropegin, H. Noël, M. Sigrist, and Peter Rogl. Heavy fermion superconductivity and magnetic order in noncentrosymmetric CePt_3Si . *Phys. Rev. Lett.*, 92(2):027003, 2004.
- [153] Mintu Mondal, Bhanu Joshi, Sanjeev Kumar, Anand Kamalpure, Somesh Chandra Ganguli, Arumugam Thamizhavel, Sudhansu S Mandal, Srinivasan Ramakrishnan, and Pratap Raychaudhuri. Andreev bound state and multiple energy gaps in the noncentrosymmetric superconductor BiPd . *Phys. Rev. B*, 86(9):094520, 2012.
- [154] Andreas P. Schnyder, Carsten Timm, and P.M.R. Brydon. Spin polarization and edge currents in topological superconductors. *arXiv:1302.3461*.
- [155] Mathias Duckheim and Piet W Brouwer. Andreev reflection from noncentrosymmetric superconductors and Majorana bound-state generation in half-metallic ferromagnets. *Phys. Rev. B*, 83(5):054513, 2011.
- [156] E. Bauer, R.T. Khan, H. Michor, E. Royanian, A. Grytsiv, N. Melnychenko-Koblyuk, P. Rogl, D. Reith, R. Podloucky, E-W Scheidt, et al. BaPtSi_3 : A noncentrosymmetric BCS-like superconductor. *Phys. Rev. B*, 80(6):064504, 2009.
- [157] H.Q. Yuan, D.F. Agterberg, N. Hayashi, P. Badica, D. Vandervelde, K. Togano, M. Sigrist, and M.B. Salamon. S-wave spin-triplet order in superconductors without inversion symmetry: $\text{Li}_2\text{Pd}_3\text{B}$ and $\text{Li}_2\text{Pt}_3\text{B}$. *Phys. Rev. Lett.*, 97(1):017006, 2006.
- [158] D.M. Kheiker, G.S. Zhdanov, and N.N. Zhuravlev. X-ray investigation of the structure of BiPd . *Zh. Eksp. Teor. Fiz*, pages 25–621, 1953.
- [159] Bhanu Joshi, A. Thamizhavel, and S. Ramakrishnan. Superconductivity in noncentrosymmetric BiPd . *Phys. Rev. B*, 84(6):064518, 2011.

-
- [160] Kazuaki Matano, Satoki Maeda, Hiroki Sawaoka, Yuji Muro, Toshiro Takabatake, Bhanu Joshi, Srinivasan Ramakrishnan, Kenji Kawashima, Jun Akimitsu, and Guo-qing Zheng. NMR and NQR studies on non-centrosymmetric superconductors Re_7B_3 , LaBiPt , and BiPd . *arXiv:1307.5382*.
- [161] V.S. Mathur, N. Panchapakesan, and R.P. Saxena. Magnetic-field dependence of the energy gap in superconductors. *Phys. Rev. Letters*, 9, 1962.
- [162] C. Caroli, P. G. de Gennes, and J. Matricon. Bound Fermion states on a vortex line in a type II superconductor. *Physics Letters*, 9:307–309, May 1964.
- [163] L. J. Barnes. Tunneling at point contacts between superconductors. *Phys. Rev.*, 184:434–446, 1969.
- [164] M.D. Lumsden and A.D. Christianson. Magnetism in Fe-based superconductors. *Journal of Physics: Condensed Matter*, 22(20):203203, (2010).
- [165] J. Zaanen and O. Gunnarsson. Charged magnetic domain lines and the magnetism of high T_c oxides. *Phys. Rev. B*, 40(10):7391, (1989).
- [166] S.A. Kivelson, E. Fradkin, and V.J. Emery. Electronic liquid-crystal phases of a doped Mott insulator. *Nature*, 393(6685):550–553, (1998).
- [167] M. Vershinin, S. Misra, S. Ono, Y. Abe, Y. Ando, and A. Yazdani. Local ordering in the pseudogap state of the high- T_c superconductor $\text{Bi}_2\text{Sr}_2\text{CaCu}_2\text{O}_{8+\delta}$. *Science*, 303:1995–1998, (2004).
- [168] Y. Kohsaka, C. Taylor, K. Fujita, A. Schmidt, C. Lupien, T. Hanaguri, M. Azuma, H. Eisaki, H. Takagi, S. Uchida, and J.C. Davis. An intrinsic bond-centered electronic glass with unidirectional domains in underdoped cuprates. *Science*, 315:1380–1385, (2007).

Acknowledgments

During the work of my thesis I was supported by a lot of people to whom I want to acknowledge:

- I am very grateful to Prof. Kern for giving me the opportunity and the honor to do my Phd under his supervision. I regard him as a great scientist whom I have learned a lot from.
- My greatest gratitude to Prof. Wahl for his excellent supervision, motivation and guidance during the period of my Phd. I consider him as my mentor and I hope to stay in contact with him in future.
- Prof. Cécile Hébert, Prof. Giorgio Margaritondo, Prof. Wulf Wulfhekel, and Dr. Steffen Wirth for graciously agreeing to examine my work.
- I would like to thank all the members of tunneling spectroscopy group: Ivan Pentegov, Zhixiang Sun, Ana Maldonado, Udai Singh, Rama Aluru, Seth White, Stefan Schmaus and all the other people from the department who supported me and made a friendly environment.
- I am thankful of the crystal preparation group in MPI-Stuttgart and MPI-Dresden for providing us nice crystals to perform measurements on. Especially I would like to thank Dr. Lin, Dr. Seiro, and Dr. Peets for their cooperation.
- I am thankful to international Max-Planck research school (IMPRS) for the financial support.
- Last but not least I want to thank my family for their encouragement and emotional support.

Publications

U. R. Singh, M. Enayat, S. C. White and P. Wahl, *Construction and Performance of a Dilution-Refrigerator based Spectroscopic-Imaging Scanning Tunneling Microscope*, Rev. Sci. Instrum., **84**, 013708, (2013)

M. Enayat, Z. Sun, U. R. Singh, R. Aluru, S. Schmaus, A. Yaresko, Y. Liu, C. T. Lin, V. Tsurkan, A. Loidl, J. Deisenhofer and P. Wahl, *Real Space Imaging of the Atomic-Scale Magnetic Structure of $Fe_{1+y}Te$* , submitted

M. Enayat, Z. Sun, A. Maldonado, H. Suderow, S. Seiro, C. Geibel, S. Wirth, F. Steglich, and P. Wahl, *Superconductivity of heavy Fermion compound $CeCu_2Si_2$ studied by milli-Kelvin Scanning Tunneling Microscope*, in preparation

Z. Sun, M. Enayat, A. Maldonado, D. Peets, A. Yaresko, A. P. Schnyder, and P. Wahl, *Surface states and superconductivity in noncentrosymmetric $BiPd$* , in preparation

Curriculum Vitæ

Name	Mostafa Enayat
Date of Birth	25.06.1985
Nationality	Iranian
2010-2014	IMPRS fellow at Max-Planck-Institute for Solid State Research, Stuttgart, Germany
2007-2009	Christian-Albrechts-Universität zu Kiel, Kiel, Germany, MSc. in Materials Science and Engineering, <i>Very Good</i>
2003-2007	Amir Kabir University of Technology, Tehran, Iran, BSc. in Materials Engineering.